Study of near-infrared pumped solid-state lasers and applications

by

Boris Golubovic

S.M. E.E.C.S., Massachusetts Institute of Technology (1994)

S.B. E.E., Massachusetts Institute of Technology (1991)

S.B. Physics, Massachusetts Institute of Technology (1990)

Submitted to the Department of
Electrical Engineering and Computer Science
in Partial Fulfillment of the Requirement for the
Degree of

Doctor of Philosophy in Electrical Engineering

at the

Massachusetts Institute of Technology

December 1997

Signature of Author _____

Department of Electrical Engineering and Computer Science
December 10, 1997

Certified by _____

James G. Fujimoto
Professor of Electrical Engineering
Thesis Supervisor

Accepted by _____

Arthur C. Smith
Professor of Electrical Engineering
Chairman, Department Committee on Graduate Studies

Study of near-infrared pumped solid-state lasers and applications

by

Boris Golubovic

Submitted to the Department of Electrical Engineering and Computer Science
on December 10, 1997 in partial fulfillment of the requirements for the degree of
Doctor of Philosophy in Electrical Engineering

ABSTRACT

Solid-state lasers with broad emission spectra are of interest because they enable the implementation of broadly tunable continuous-wave sources or the generation of short temporal optical pulses. Chromium-doped forsterite is a solid-state gain medium with a broad emission band centered near 1.3 μm. The goal of this thesis was to investigate new aspects in the design of these lasers which would allow for the implementation of more robust and compact laser systems. Studies of fluorescence spectra, tuning ranges, lasing efficiencies, and limiting slope efficiencies were performed on chromium-doped forsterite lasers pumped at 1064 nm with gain crystals oriented along different crystallographic axes. In addition to the absorption at the commonly used 1064 nm wavelength region, chromium-doped forsterite has larger absorption coefficients around 740 nm. In contrast to pumping at 1064 nm, pumping near 740 nm permits the use of shorter crystal lengths which enable the development of compact and diode pumped laser geometries. This thesis describes the room-temperature operation of a chromium-doped forsterite laser using a Ti:Al_2O_3 pump laser. Continuous-wave laser characteristics were investigated over a range of pump wavelengths compatible with diode pumping. Room temperature continuous-wave operation with the broadest tuning range yet (1175 to 1375 nm) was achieved and modelocked operation with 50 fs pulses was demonstrated. This thesis also presents a continuous-wave chromium-doped forsterite laser that permits rapid wavelength tuning over a broad bandwidth and demonstrates the application of this source to high-resolution optical frequency domain ranging. The tuning range of 1200 to 1275 nm was swept in less than 500 μs which enabled for optical ranging with scan rates of up to 2000 scans per second at an axial resolution of 15 μm. This ranging method can be extended to other solid-state lasers.

Thesis Supervisor: James G. Fujimoto
Title: Professor of Electrical Engineering

Acknowledgments

I thank my advisor Professor James Fujimoto for giving me the opportunity to perform the work presented in this thesis. This research would have not been possible without the resources of the Optics Group. I would also like to thank Professors Erich Ippen and Hermann Haus for their help and inspiration over the years. In particular I am grateful to Professor Ippen for serving on more than one of my examination committees. My thanks are also due to Professor Shaoul Ezekiel for being a member of my thesis committee as well as teaching my first optics class. His enthusiasm and sense of humor were always an inspiration.

Over the past few years I worked closely with Dr. Brett Bouma from whom I learned a great many things which contributed to the completion of this thesis. Brett's insights and willingness to teach others were always uplifting, and particularly in times when results seemed so far away. But above all, I value the friendship we have developed through so many hours spent in lab.

Many thanks also go out to other members of the Optics Group with whom I shared the past years, Igor Bilinsky, Stephen Boppart, David Jones, Costas Pitris, and Gary Tearney. Their friendship and camaraderie were a source of support over the years. Special thanks go to Cindy Kopf for all the advice, administrative help, and organizing Optics Group events.

I would also like to thank John and Ellen Essigmann, their work as housemasters of New House and their concern for the well being of MIT students are always an inspiration. Their friendship and support helped my success and for this I am grateful. Jonathan Wilker, and his upbeat outlook on life were always a refreshing and welcome distraction. My years at MIT would have not been as positive of an experience without the many friends I have made over the years. Thank you all!

Finally, and most importantly, I would like to thank my mother Hildegard, whose unwavering love and support were a source of strength and stability throughout the years. Even though my late father Tomislav was only able to share my excitement of getting accepted to MIT as an undergraduate, his belief in my abilities and his joy of life will always be with me. The success of this work was in no small part possible due to my parents belief in the value of education and the pursuit of ones interests.

Contents

Chapter 4

Near-IR pumping of Cr^{4+}:forsterite

Chapter 5

Optical frequency domain reflectometry using rapid wavelength tuning of a cw Cr^{4+}:forsterite laser

Chapter 1

Introduction

1.1 Background

In recent years lasers have been increasingly finding applications outside the research laboratory environment and are becoming an indispensable tool in communications, manufacturing, medicine, and an integral part of consumer goods. This onset of commercial applications of lasers also spurred the interest in the development of systems which would meet the need of specific applications. Depending on the actual application, laser systems have to meet requirements including operation in a specific wavelength region, narrow spectral output, broad wavelength tuning range, or the output of short temporal optical pulses. The wide range of laser applications, and the non-traditional settings where they are used, demand that lasers approach the reliability and ease of use associated with turn-key instruments. Thus, research and development efforts more recently include work on compact, robust, and power efficient systems capable of operation in a multitude of environments.

Systems with broad wavelength emission ranges are of interest since the access to a larger number of emission wavelengths generally extends the number of possible applications. Broad emission-band materials can be used for either the implementation of tunable continuous-wave (cw) lasers, or for lasers generating short optical pulses. This is of particular interest if a system is used as diagnostic or measuring tool in laboratories, but is also of importance and beneficial in other commercial laser applications. Traditionally dye lasers have been employed where broad tuning ranges were required. However, due to the often difficult-to-use nature of this technology (handling of liquid gain media), and the hazardous waste generated from toxic dye and solvent use, a more robust replacement was desired. Gas lasers and more recently semiconductor lasers

generally can not provide the large emission bandwidths available from dye lasers. Even though solid state materials were used in the first demonstration of laser action [1], their wide spread use in tunable systems started with the demonstration of the Ti:Al_2O_3 laser by Peter Moulton [2]. This gain medium was compatible with the design of dye-laser cavities as well as the frequently used Argon-ion pump laser. Since the introduction of the Ti:Al_2O_3 laser, other solid-state tunable materials at various wavelength were introduced.

1.2 Solid-state laser materials

In general, laser materials must have well defined fluorescent emission bands and strong absorption bands allowing for reasonably high efficiency in exciting the fluorescent transition of interest. These characteristics are often shown by solids (crystals or glasses) which incorporate small amounts of elements in which optical transitions can occur. In addition to well defined emission bands, laser materials should also have absorption bands which can be accessed by readily available pump sources and can generate a population inversion. Typical pump sources for solid state lasers are flashlamps, gas or solid-state lasers, or semiconductor laser devices. Figure 1-1 shows a number of well established tunable solid-state materials and their corresponding wavelength coverage.

Since it was introduced [2], the Ti:Al_2O_3 laser has been the subject of numerous studies and today represents the most widely used tunable solid-state laser gain medium. It has an emission band ranging from 660-1100 nm and it be can operated in either a continuous-wave or short-pulse mode. One of the most important methods for short-pulse generation from laser oscillators, Kerr-lens modelocking, was demonstrated with a Ti:Al_2O_3 laser [3]. In addition, the shortest optical pulse to-date generated directly from a lasers oscillator, 6.5 fs [4], was generated using this gain medium. New studies using Ti:Al_2O_3 lasers still continue, and this laser systems remains an important platform for laser system development and various laser applications. However, one of the drawbacks of Ti:Al_2O_3 laser systems is that the absorption band peaks around 490 nm and is not accessible with current semiconductor laser diodes. Traditionally excitation is achieved with argon-ion lasers, but recently diode-pumped frequency doubled Nd:YAG and Nd:YVO_4 lasers

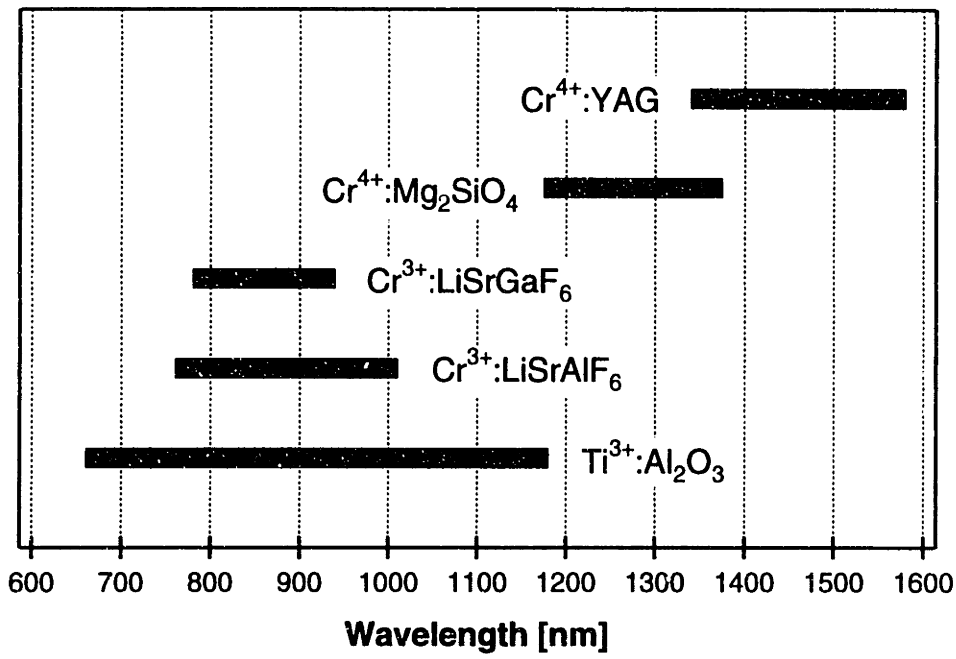

FIGURE 1-1: Commonly used, room-temperature, operated tunable solid-state lasers provide coverage over much of the near-infrared wavelength region.

were introduced which can replace argon-ion lasers in applications where less that 10 W of pump power are required. This in turn allows for the design of more compact and robust Ti:Al_2O_3 laser systems.

To address the need for laser sources which can be directly pumped by existing semiconductor diodes a number of "designer" crystals were developed with emission bands similar to Ti:Al_2O_3 lasers. The most well known laser crystals in this category are Cr^{3+}:$LiCaAlF_6$ (Cr:LiCAF) [5], Cr^{3+}:$LiSrAlF_6$ (Cr:LiSAF) [6] and Cr^{3+}:$LiSrGaF_6$ (Cr:LiSGaF) [7] all developed at the Lawrence Livermore National Laboratory (Livermore, CA). All three of these materials have absorption bands that permit laser action using visible semiconductor laser diodes for pumping [8][9][10]. Even though the laser efficiencies of Cr:LiSAF and Cr:LiSGaF were found to be slightly less than that of Cr:LiCAF, they have resulted in more interest due to their larger emission cross sections and broader tuning ranges. Spectroscopic properties and the thermal quenching of the upper state lifetime are very similar in of both Cr:LiSAF and Cr:LiSGaF, [11]. With respect to some mechanical properties however, Cr:LiSGaF is an improvement on Cr:LiSAF and has thermal expansion coefficients which are lower as well as more isotropic along the different crystal

axes. Both materials are being fabricated with increasing crystal quality and are available from commercial sources. Broad cw tuning ranges and mode-locked operation were studied with both gain media using diffraction limited krypton-ion pump lasers as well as broad-area semiconductor diode lasers [12][13]. Pulses as short as 15 fs were generated from Cr:LiSAF and 14 fs from Cr:LiSGaF oscillators [14]. These material systems were also extensively used in mode-locked oscillators using various semiconductor saturable absorber structures for self-starting mode-locked performance [15][16]. For the case of Cr:LiSAF and Cr:LiSGaF high output powers are typically limited by highly non-diffraction-limited laser-diode pump beams and by upper-state lifetime quenching. Novel laser geometries allow for diode-pumped systems with output powers of as much as 1.1 W cw [17], and 500 mW under mode-locked operation [18]. In summary, the Cr:LiSAF and Cr:LiSGaF material systems are a direct diode-pumped substitute for Ti:Al_2O_3 lasers operating in the 900-1000 nm range in applications where only moderate output power is needed.

For telecommunications applications laser sources with emission around the 1300 and 1550 nm wavelength regions are needed. The 1300 nm wavelength region overlaps with the zero-dispersion operating region of conventional optical fibers, whereas the 1550 nm region is commensurate with the low-loss wavelengths of optical fibers. The Cr^{4+}:YAG laser, first reported by Angert *et al.* [19] in 1988, is a source which can be tuned over the 1550 nm wavelength region where the present-day low-loss fiber-optic transmission systems are operated. The absorption spectrum has a region of strong absorption in the visible, and a broad absorption band in the 900-1100 nm region which makes the Cr^{4+}:YAG laser suitable for pumping using 1064 nm Nd:YAG or Nd:YVO_4 lasers. Operation of the Cr^{4+}:YAG gain crystal was achieved in Q-switched [19][20], cw [20][21], and mode-locked laser implementations [22][23]. Continuous-wave operation was demonstrated throughout the region from 1340-1580 nm. In mode-locked configurations optical pulses as short as 43 fs were obtained from a Cr^{4+}:YAG oscillator [24]. The gain bandwidths, as well as the cw-tuning range, indicate that shorter optical pulses could be attained but it is believed that the presence of several water absorption lines may preclude this in all but *dry* systems. When combined with compact, diode-pumped 1064 nm pump lasers, Cr^{4+}:YAG lasers can be implemented into

TABLE 1-1: Vibronically broadened tunable solid-state laser gain media and select parameters: laser tuning range, $\Delta\lambda$; absorption peak associated with the pump wavelength used, λ_P; excited state lifetime, τ; saturation fluence, E_{sat}; stimulated emission cross section, σ; refractive index at center of the tuning range; shortest optical pulse to-date, Δt.

	$Ti^{3+}:Al_2O_3$ (Ti:sapphire)	$Cr^{3+}:LiSrAlF_6$ (Cr:LiSAF)	$Cr^{3+}:LiSrGaF_6$ (Cr:LiSGaF)	$Cr^{4+}:Mg_2O_3$ (Cr:forsterite)	Cr^{4+}:YAG (Cr:YAG)
$\Delta\lambda$ [nm]	660-1180	780-1010	780-940	1175-1375	1340-1580
λ_P [nm]	490	670	670	740, 1064	1064
τ [μs]	3.3	67	88	2.7	3.6
E_{sat} [$J \cdot cm^{-2}$]	0.8	5	5	0.8	0.4
σ [$\times 10^{-20}$ cm^{-2}]	30	4.8	3.3	20	30
T_C [$W \cdot (m \cdot K)^{-1}$]	34	3.2	3.5	5	13
Refractive index	1.76	1.41	1.41	1.64	1.81
Diode pumping	no	yes	yes	yes	yes
Δt [fs]	6.5	15	14	25	43

robust turn-key systems. Operating around 1500 nm, Cr^{4+}:YAG complements other tunable solid-state lasers in providing a tunable, mode-locked source for spectroscopy, remote sensing, and study of communication systems operating in this wavelength range.

1.3 Statement of work

Chromium-doped forsterite is a solid-state laser material with a broad emission band extending from 1175 nm to1375 nm. Tunability around 1.3 μm, the zero-dispersion wavelength of conventional optical fibers, is important for telecommunication applications and is of increasing interest in the medical field for non-invasive imaging. The importance of this wavelength region motivated a number of studies on Cr^{4+}:forsterite lasers, and this thesis complements past efforts. A systematic study of Cr^{4+}:forsterite laser performance depending on the crystallographic orientation of the gain crystal was performed. Most previous studies on Cr^{4+}:forsterite lasers used pump lasers accessing the 1064 nm absorption band whereas this work also examined the room-temperature operation of a Cr^{4+}:forsterite laser pumped around 740 nm. This pump wavelength region is accessible by current semiconductor laser devices and is of interest because it enables direct diode pumping. Experience gained from diode pumping of Cr^{3+}:LiSGaF was used as model for the investigation of direct-diode pumping in Cr^{4+}:forsterite lasers.

Optical ranging systems are of importance in engineering as well as medical applications. One of the technologies used for optical ranging is optical frequency domain reflectometry. In optical frequency domain reflectometry a narrow-linewidth optical source is needed for which the wavelength can be continuously scanned. The resolution of this type of system increases as the cw tuning range of the optical source is increased. Since the solid-state lasers presented in Figure 1-1 all have considerable tuning ranges, high-resolution spatial imaging should be possible using cw wavelength tuning. The use of a rapidly tunable cw Cr^{4+}:forsterite laser for optical frequency domain ranging was examined and the limitations of such system were assessed.

Chapter 2

Material properties of Cr^{4+}:forsterite

2.1 Introduction

Solid-state materials suitable for supporting optical gain are of interest for the design of lasers and optical amplifiers. In these materials it is possible to maintain a population inversion by optical pumping using either pump lasers or flash-lamp sources. A small number of such materials actually get to be implemented into laser systems for long-term, wide-spread, commercial use. In general, for a material to become widely accepted for laser design, it has to have emission characteristics which are of interest to some specific applications, a pump source has to be readily available, and the whole system should preferably be implemented at an affordable cost. Chromium-doped forsterite is a gain material with a wide vibronically broadened emission-band centered in the 1.3 μm wavelength range. This broad emission-band is well suited for the implementation of broadly tunable cw sources or the generation of ultra-short optical pules. Moreover, this wavelength region was originally of particular interest in communications applications, but has more recently also gained interest for applications in medical imaging. Finally, chromium-doped forsterite has several absorption bands which can be accessed by a number of currently available pump laser systems.

2.2 Crystallographic properties of Cr^{4+}:forsterite

Forsterite (Mg_2SiO_4) is a member of the olivine family of crystals and is a naturally occurring gem. In the laboratory single crystals of forsterite can be grown by the Czochralski method. A unit cell of forsterite belongs to the orthorhombic system with the space group *Pbnm* in which

the Si ion occupies a tetrahedral site and the Mg ions occupy two unequivalent octahedral sites. In an orthorhombic crystal system the lattice constants are unequal; $a \neq b \neq c$, and the corresponding crystal planes are mutually orthogonal such that $\alpha=\beta=\gamma=90°$. The actual forsterite unit cell has dimensions: a=0.476 nm, b=1.022 nm, and c=0.599 nm and a forsterite crystals can be grown along any of these axes. Crystals grown along different directions in general exhibit different crystallographic properties [25] and the actual crystal axis orientation can be determined using Laue x-ray crystallography.

Laser action in chromium-doped forsterite is attributed to Cr^{4+} ions substituting for Si^{4+} in tetrahedrally coordinated lattice sites [26][27][28]. However, chromium in the forsterite lattice can also be found as Cr^{2+} or Cr^{3+}, and can occupy either of two distinct, sixfold coordinated Mg^{2+} sites, one with inversion symmetry (site M1) and one with mirror symmetry (site M2) [27][28][29][30][31][32]. Absorption and emission spectra can contain features due to any of these different chromium charge state, which originally contributed to some uncertainty in identifying the actual center responsible for laser action in chromium-doped forsterite. The absorption of Cr^{4+}:forsterite is similar to other chromium doped crystals which contain tetrahedral sites [33][34][35][36][37]. In each case, the 1064 nm absorption can be attributed to the $^3A_2 \rightarrow {}^3T_2$ transition in Cr^{4+}. There is also a near-infrared transition, $^3A_2 \rightarrow {}^3T_1$, which results in ground-state absorption and its use for laser design will be discussed in Chapter 4. In addition, a number of theoretical works discussed and supported the understanding that Cr^{4+} is the active ion and not Cr^{3+} as early studies suggested [27][38][39]. Finally, growth of forsterite in a pure oxygen environment resulted in crystals which have negligible amounts of the Cr^{3+} ion and studies using these crystals experimentally support the understanding that Cr^{4+} is the lasing ion in chromium-doped forsterite [40][25].

2.3 Absorption characteristics of Cr^{4+}:forsterite

The characterization of Cr^{4+}:forsterite absorption along different crystallographic axes is important for choosing the crystal orientation for use in lasers. To measure the absorption along different crystallographic axes, a right-angle parallelepiped was polished for propagation along the a- and c-axis of the crystal. The crystal dimensions were along the: a-axis, 1.15 cm; and c-axis, 0.70 cm. The labeling convention used in this study and the relation to standard crystallo-

graphic planes is shown in Table 2-1. It is to be noted that there is some inconsistency throughout

TABLE 2-1: Crystal axis label and relation to standard crystallographic planes.

a-axis	perpendicular to the [100] plane
b-axis	perpendicular to the [010] plane
c-axis	perpendicular to the [001] plane

the literature with respect to the notation of the *a*- and *c*-axis in forsterite crystals and the two labels are at times interchanged. The incident and transmitted pump power were measured for propagation along the *a*- and *c*-axis, for polarizations along each of the orthogonal crystal axes. These measurements were repeated for a number of pump wavelengths ranging form 670-1064 nm. A tunable cw *Coherent Mira 900* Ti:Al_2O_3 laser was operated using the short wavelength mirror set for absorption measurements from 670-850 nm and using the long wavelength mirror set for measurements in the range from 860-1000 nm. The data for absorption at 1064 nm were obtained using a flashlamp pumped Nd:YAG laser. To account for surface reflections, the measured incident, P_{IN}, and transmitted, P_{OUT}, pump powers were corrected using the reflection coefficient at normal incidence

$$R = \left(\frac{n_1 - n_2}{n_1 + n_2}\right)^2 = \left(\frac{1 - 1.64}{1 + 1.64}\right)^2 = 5.9\% \tag{2-1}$$

where the index of refraction for forsterite is 1.64. The actual absorption coefficients for a crystal of length, L, were then calculated using power conservation such that

$$(1 - R)P_{IN}e^{-2\alpha(\lambda)L} = \frac{P_{OUT}}{(1 - R)} \tag{2-2}$$

and the measured absorption coefficients shown in Figure 2-1 were evaluated using

$$\alpha(\lambda) = -\frac{1}{2L}\ln\left(\frac{P_{OUT}}{P_{IN}}\frac{1}{(1 - R)^2}\right). \tag{2-3}$$

There are typically two criteria for selection of laser crystal orientation and these are set by the choice/availability of pump laser wavelengths and the need for sufficient power absorption in the crystal. Initial work on Cr^{4+}:forsterite was based on widely available 1064 nm pump lasers. These pump systems are readily available with cw pump powers as high as 10 W and are typically used with a Cr^{4+}:forsterite crystal oriented such that the pump propagates along the *a*-axis and with the polarization is parallel to the *b*-axis. From the data in Figure 2-1 it can be seen that the absorption coefficient for this pump wavelength is favorable for a pump polarization parallel to the *b*-axis. However, from the absorption properties only, it is not clear if there is any actual advantage in propagating along either the a-axis or c-axis. This ambiguity was the focus of work presented in section 3.2 where the cw performance of Cr^{4+}:forsterite lasers for which the pump propagates along these two axes (and the pump polarization parallel to the *b*-axis) were studied.

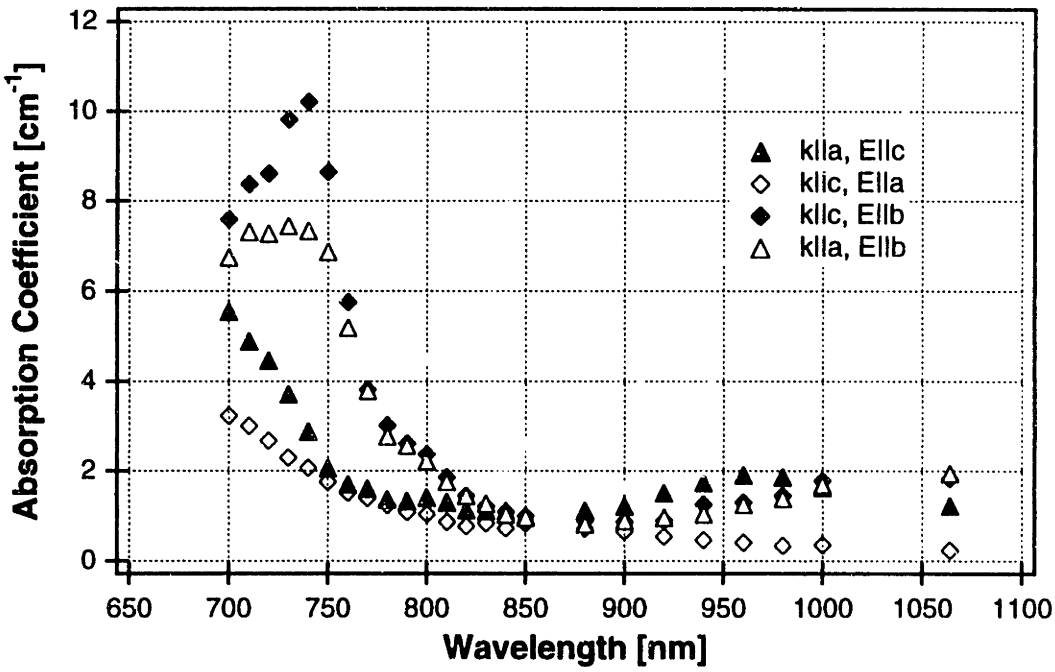

FIGURE 2-1: Absorption spectra in Cr^{4+}:forsterite for pump propagation and polarization along different crystallographic axis.

There are cases for which pumping with the polarization parallel to the b-axis is not the most optimal crystal orientation. In the work by Evans *et al.* [41] a Cr^{4+}:forsterite laser was implemented using a crystal oriented for propagation along the *a*-axis and with the incident polarization parallel to the *c*-axis. In the cited work a 980 nm diffraction-limited semiconductor master-

oscillator-power-amplifier pump laser was used. Since such devices typically have <1 W of available pump power it was important to maximize the absorbed power in the 16 mm long laser crystal. For such choice of pump wavelength it was necessary to select a crystal for which k||a and E||c because this resulted in the largest possible absorption coefficient and consequently the highest absorbed pump power (see Figure 2-1).

The data in Figure 2-1 indicate that absorption coefficients for pumping in the near-infrared are the largest for propagation along the *c*-axis with the polarization parallel to the *b*-axis. However, the systematic error for measurements in the 710-760 nm region was relatively high for E||b, and in particular for the case where k||a. The crystal length in the *a*-direction was 1.15 cm and resulted in virtually all the incident power being absorbed and a high measurement uncertainty of the transmitted power. Subsequent measurements using shorter crystals oriented with k||a and E||b, resulted in near-IR absorption coefficients as well as spectral dependency, very similar to the ones obtained for the case where k||c and E||b (see Figure 4-1).

In summary, Cr^{4+}:forsterite has two broad absorption bands, one centered around 1000 nm, and the other in the near-IR extending into the visible region. These bands primarily correspond to the $^3A_2 \rightarrow {}^3T_2$ and $^3A_2 \rightarrow {}^3T_1$ transitions of the Cr^{4+} ion, respectively. Depending on the pump wavelength, propagation axis, and polarization axis different absorption coefficients for Cr^{4+}:forsterite crystals can be obtained. The choice for laser implementation is typically set by the pump wavelength and availability of actual crystals. Moreover, from measuring the absorption only, it is not clear if the lasing efficiency is equivalent for all pumping geometries, thus, further measurements may have to be made for a specific choice of propagation/polarization orientations.

Chapter 3

Cr^{4+}:forsterite pumped at 1064 nm

3.1 Introduction

Chromium-doped forsterite lasers were first reported almost ten years ago [42]. Early work reported pumping at 1064 nm, as well as the second harmonic, 532 nm, of Nd:YAG or Nd:glass lasers. The wide availability of these pump lasers resulted in a large number of publications on Cr^{4+}:forsterite laser implementations. However, almost all studies involving Cr^{4+}:forsterite were conducted using the same crystal orientation where the pump propagation was along the *a*-axis and pump polarization parallel to the *b*-axis. This section presents a comparative study of the cw performance in Cr^{4+}:forsterite laser systems using different gain crystal orientations. Also, the implementation of a Kerr-lens mode-locked Cr^{4+}:forsterite optical source for optical coherence tomography applications will be presented.

3.2 Lasers using *a*-axis and *c*-axis crystal orientations

Gain crystals have, in general, different optical properties depending on the pump propagation and polarization axis. Since in forsterite the crystallographic axes are mutually orthogonal the propagation axis and the two incident polarizations can always be aligned along a principal crystal axis for characterization. From Figure 2-1 it can be seen how the absorption in Cr^{4+}:forsterite depends on the propagation axis and how it changes for the cases where different pump polarizations are used. In addition, the crystal growth-rate also depends on the crystallographic growth axis. Among the three crystal axes, crystals grown along the *a*-axis have the fastest growth rate, whereas crystals grown along the *b*-axis have the slowest growth rate [25]. Most experimental studies of Cr^{4+}:forsterite based laser and amplifier systems have been conducted using a 1064 nm

pumped crystal with the pump beam propagating along the *a*-axis and polarized along the *b*-axis. From the absorption coefficient measurements shown in Figure 2-1 it can clearly be seen that pumping with the polarization oriented along the *b*-axis is most beneficial. However, from the absorption spectrum in Figure 2-1 it is not evident if there is any advantage for pump propagation along the crystallographic *a*-axis or *c*-axis. Lasers based on *a*-axis crystals were extensively characterized for their fluorescence spectrum, cw laser output characteristics, limiting slope efficiencies and laser tuning range [26][43][44][40]. The characterization of lasers based on *c*-axis grown crystals is primarily of interest because growth along this axis may permit the fabrication of higher doping density crystals than the commonly used *a*-axis grown crystals [45]. Therefore, the comparative study presented in this section examines the performance of Cr^{4+}:forsterite lasers with the pump polarization oriented along the b-axis and pump propagation along the *a*-axis and *c*-axis. In principle it is not necessary to grow a Cr^{4+}:forsterite along the *a*-axis for it to be used for pump propagation along this axis. There is no fundamental reason for why the Cr^{4+}:forsterite crystal could not be grown along the *c*-axis and used for pump propagation along the *a*-axis. However, crystal boule dimensions (80 mm long the growth axis, 25 mm in diameter [25]) are typically such that it is not possible to cut a long enough, laser quality crystal along the boule width and as such the growth direction does restrict the usable pump propagation direction. Thus, if high Cr^{4+} doping densities in forsterite are indeed restricted to *c*-axis grown crystals, it is important to examine the performance of Cr^{4+}:forsterite lasers systems for which k||c and E||b.

3.2.1 Crystal specifications

The "*a*-axis" chromium-doped forsterite crystal was grown by the Czochralski method along the crystallographic *a*-axis with 0.130% weight in the melt, and an actual concentration of Cr^{4+} ions was measured by X-ray fluorescence to be 0.08%. The crystal was cut into a 3×3×18 mm^3 Brewster angle cut slab oriented such that the pump propagation axis was along the *a*-axis and the polarization parallel to the crystal *b*-axis. The crystal orientation after cutting was verified by Laue x-ray crystallography such the direction of the incident x-rays was selected to be parallel to the what was believed to be the *c*-axis. The Fraunhofer x-ray diffraction pattern recorded on the film, shown in Figure 3-1, was matched against the expected spot pattern from an orthorhombic crystal with this orientation. The close agreement between the calculated and measured spot loca-

tions verified the predicted crystal axis orientation as shown in Figure 3-1. An absorption coefficient at the pump wavelength of 1064 nm was measured as α=0.87 cm^{-1} with a total absorption in the crystal of 79% of the incident pump power.

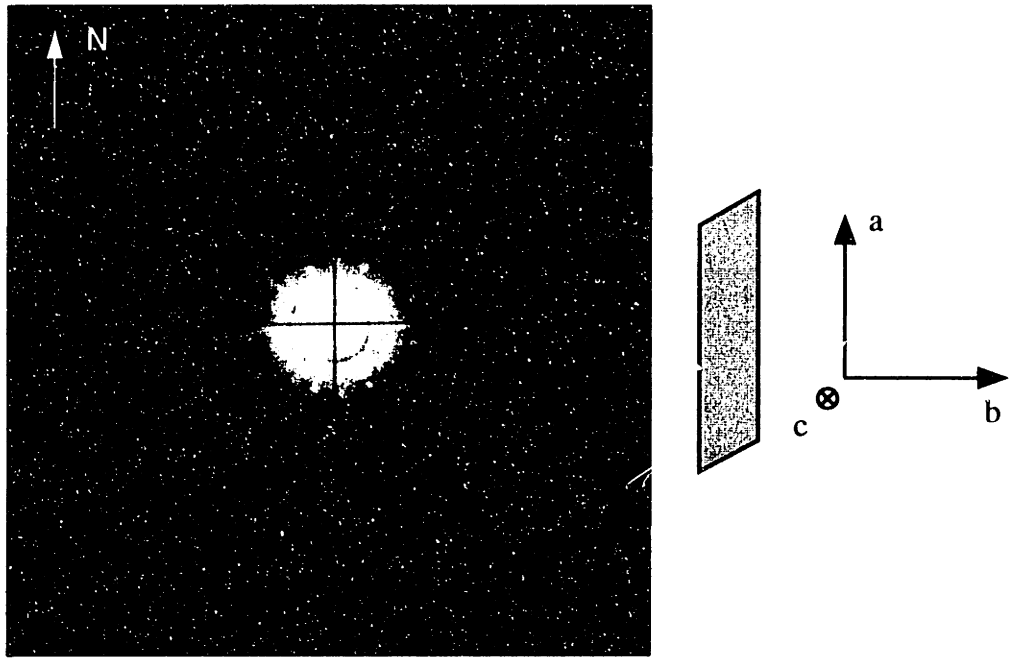

FIGURE 3-1: Laue x-ray crystallography pattern (left) for the *a*-axis Cr^{4+}:forsterite laser crystal and corresponding crystal orientation (right). The beam energy was set to 25 kV with a beam current of 20 mA, and a 15 min exposure time.

The "*c*-axis" chromium-doped forsterite crystal was grown by the Czochralski method along the crystallographic *c*-axis with 0.147% weight in the melt, and an actual concentration of Cr^{4+} ions was measure by X-ray fluorescence to be 0.09%. The crystal was cut into a 3×3×20 mm^3 Brewster angle cut slab oriented such that the pump propagation axis was along the *a*-axis and the polarization parallel to the crystal *b*-axis. The crystal orientation after cutting was verified by Laue x-ray crystallography such the direction of the incident x-rays was selected to be parallel to the what was believed to be the *a*-axis. The Fraunhofer x-ray diffraction pattern recorded on the film, shown in Figure 3-2, was matched against the expected spot pattern from an orthorhombic crystal with this orientation. The close agreement between the calculated and measured spot locations verified the predicted crystal axis orientation as shown in Figure 3-2. An absorption coefficient at the pump wavelength of 1064 nm was measured as α=0.98 cm^{-1} with a total absorption in the crystal of 86% of the incident pump power.

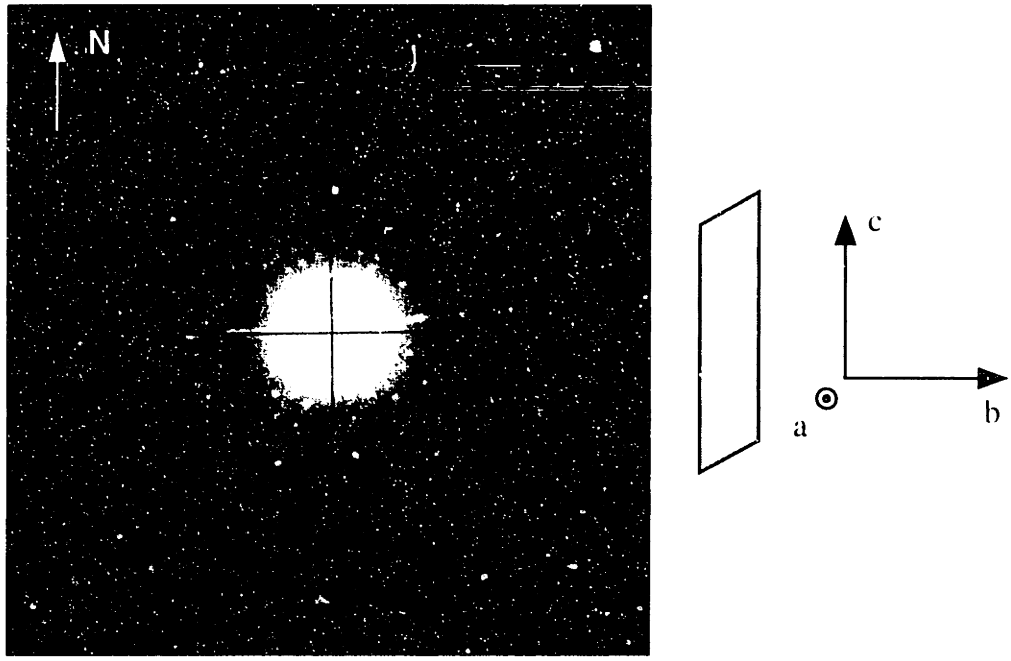

FIGURE 3-2: Laue x-ray crystallography pattern (left) for the *c*-axis Cr^{4+}:forsterite laser crystal and corresponding crystal orientation (right). The beam energy was set to 25 kV with a beam current of 20 mA, and a 15 min exposure time.

The fluorescence spectrum of a material sets the upper limit on the tuning range of any lasing emission from a material. Thus, initial work in comparing the *a*-axis and *c*-axis grown crystals comprised in the comparison of the fluorescence spectra when excited with 1064 nm Nd:YAG laser radiation polarized along the crystallographic *b*-axis (Figure 3-3). The fluorescence was measured by off-axis imaging of the crystal in order to minimize the contribution of scattered pump radiation to the measured fluorescence signal. When comparing the *a*-axis and *c*-axis crystal fluorescence a close correspondence was observed. The two spectra were virtually identical in the long wavelength region but there was a relatively stronger fluorescence for the *a*-axis crystal in the region below 1150 nm. Since it can be assumed that the spectral width of the fluorescence determines the upper limit to the tuning bandwidth of this solid-state laser medium it can be expected that the tuning range for both crystals would be virtually identical.

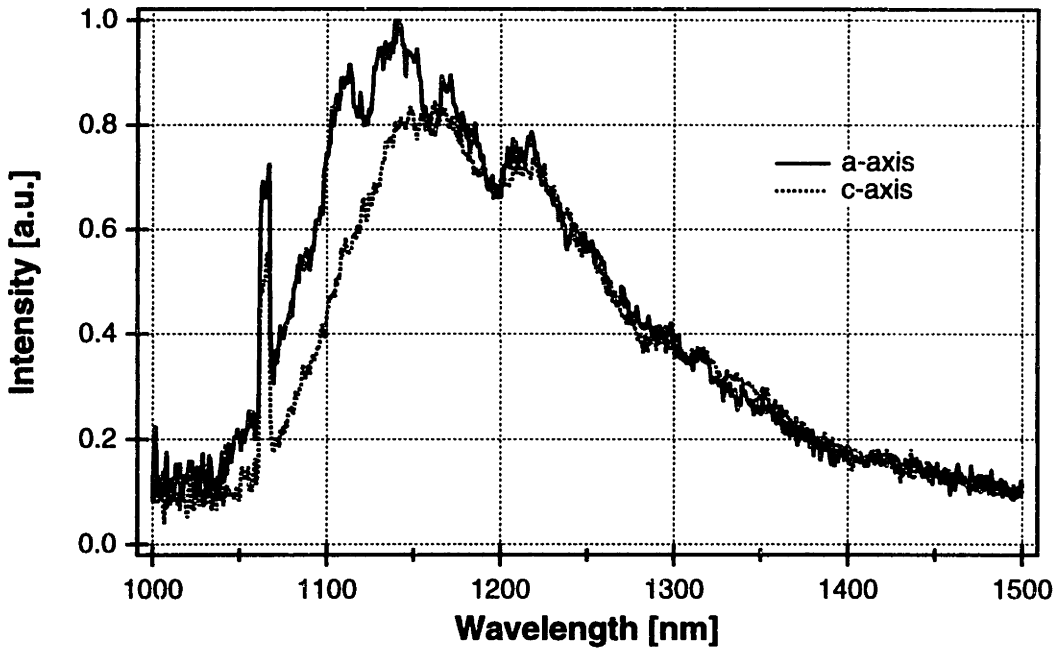

FIGURE 3-3: Fluorescence spectra for Cr^{4+}:forsterite grown along the crystallographic *a*-axis and *c*-axis using a 1064 nm Nd:YAG pump laser polarized parallel to the *b*-axis.

3.2.2 Continuous wave laser operation performance

For the purpose of the experiments presented in this section, the forsterite crystal was excited by linearly polarized, continuous wave, 1064 nm radiation from a Nd:YAG pump laser. The experiments were performed such that the pump beam propagated along either the *a*- or *c*-axis and the polarization was parallel with the *b*-axis for either choice of crystals. In order to compare the performance of the *a*-axis and *c*-axis laser crystals, identical cavities were used to perform the measurements. Both laser crystals were placed in symmetric *z*-cavities with arm lengths of 19 cm. Each cavity was formed by a pair of 100 mm radius-of-curvature folding mirrors, a planar high-reflector, and an output coupler. The laser crystals were mounted in water-cooled copper heat-sinking mounts such that the temperature could be maintained at 11°C. Lower temperatures would typically result in a larger gain but were limited by water vapor condensation on the crystal faces. The Cr^{4+}:forsterite crystal was pumped by a 1064 nm Nd:YAG flashlamp pumped laser with an output power up to 8W. The curved folding mirrors were optimized for operation with a

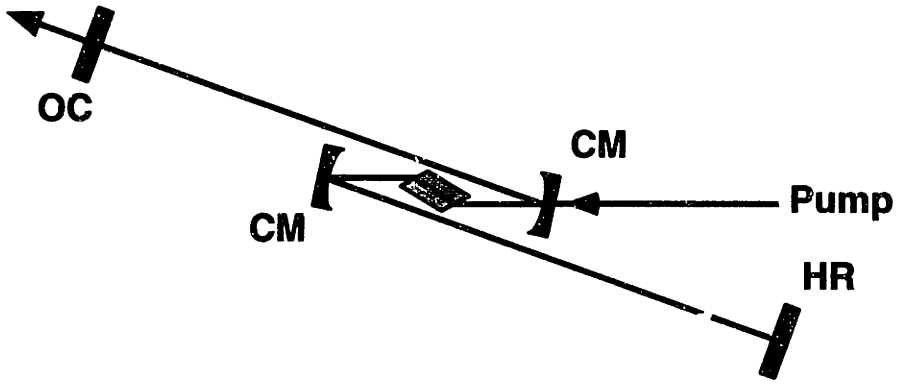

FIGURE 3-4: Symmetric z-cavity: OC, output coupler; CM's, 100 mm radius-of-curvature folding mirrors; HR, high reflector. The cavity arm lengths for both crystals were 19 cm.

1064 nm pump laser such that $T(1064)=91\%$. The laser cavity was re-optimized at each pump power to exclude any performance degradation due to thermal lensing effects in the forsterite crystal.

Lasing was obtained for different output couplers and the output power as a function of the absorbed 1064 nm cw pump was measured for both crystals. The lasers were each operated with two output couplers, 2.4% and 4.9%, and a linear relationship between the absorbed pump power in the crystal and the laser output was obtained. By performing a linear fit to the data in Figure 3-5 the slope efficiencies, η_S, and absorbed pump powers at threshold can be extracted and are presented in Table 3-1. The slope efficiencies using either output coupler are lower for the *c*-axis laser than the ones obtained with the *a*-axis laser. This can be either due to some intrinsic inferior property of the *c*-axis crystal, or can be the result of imperfect crystal growth. To determine if there is a fundamental reason for this diminished performance of the *c*-axis laser the limiting slope efficiencies have to be obtained and compared.

3.2.3 Laser crystal parameters

In order to fully characterize and compare the *a*-axis and *c*-axis laser crystals it is necessary measure the unsaturated gain and parasitic loss in the crystals, as well as to determine the limiting slope efficiency of both Cr^{4+}:forsterite gain crystals. The unsaturated gain, γ, is the gain indepen-

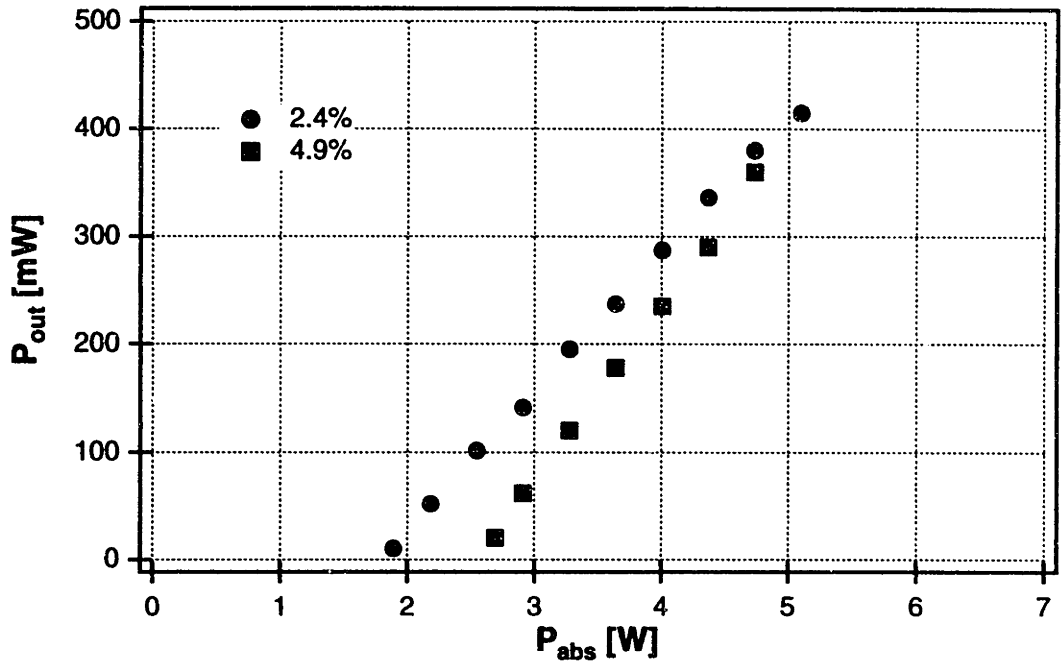

(a)

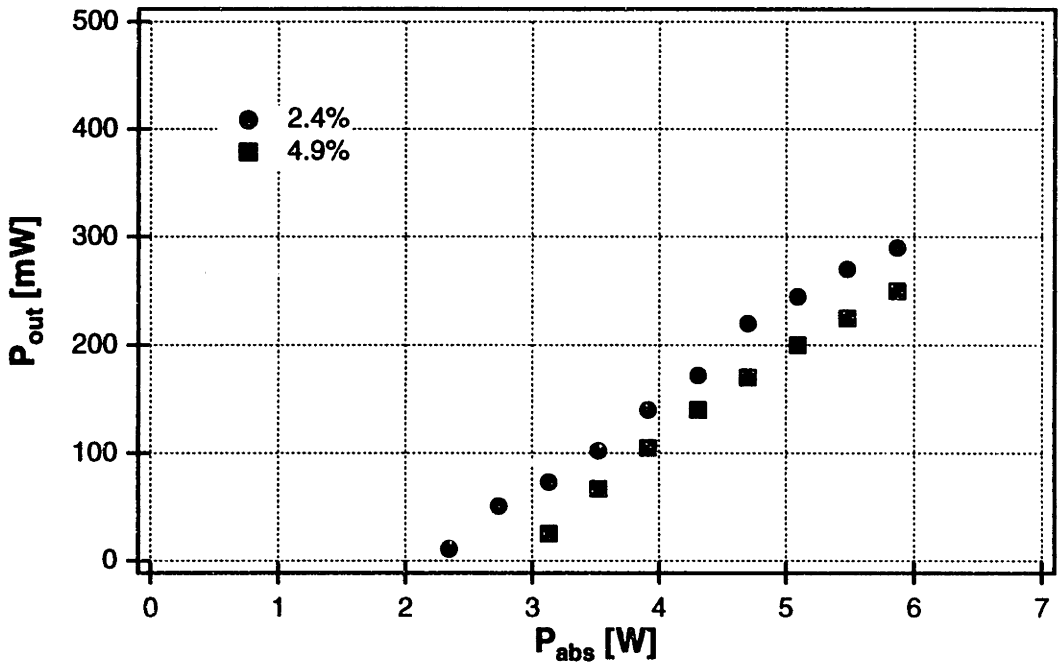

(b)

FIGURE 3-5: Cr^{4+}:forsterite laser output as a function of absorbed 1064 nm pump power for different output couplers: (a) *a*-axis crystal, (b) *c*-axis crystal.

TABLE 3-1: Slope efficiencies and absorbed threshold pump powers for a-axis and c-axis lasers and for two output couplers. The values were obtained by applying linear fits to the data in Figure 3-5.

	a-axis		c-axis	
OC	η_s	P_{th} [W]	η_s	P_{th} [W]
2.4%	12.7%	1.78	8.2%	2.19
4.9%	16.3%	2.55	8.2%	2.69

dent of intracavity intensity and is typically observed close to threshold The parasitic loss is the undesired loss in the gain crystal at the laser emission wavelength. The limiting slope efficiency is the best slope efficiency a laser system can have if the gain crystal would be void of all losses due to material imperfections. In order to characterize the crystals and extract the desired crystal parameters it was necessary for the laser to operate for a large number of calibrated output couplers. Since only two calibrated output coupler substrates were available, a continuously variable output coupler was inserted into the laser resonator.

Variable output coupler calibration

To implement a continuously variable output coupler a thin glass window was placed into the laser resonator and rotated near Brewster's angle. The reflectivity of the glass window changes with angle and results in a continuously variable output coupler. The first step to the use of this continuously variable output coupler is to properly calibrate how the glass window angular deflection relates to laser output coupling. The window can be operated at Brewster's angle in either laser arm and is typically set by ease of use. Also, the window is oriented at brewster angle only because low output coupling values were desired, however if there is sufficient gain or larger output coupling values are desired the angle can be adjusted appropriately. It is not advised to operate the plate close to normal with respect to the intracavity mode to avoid possible etalon effects. The variable output coupler can be calibrated by simultaneously measuring the laser output from the either side of the glass window, P_{G1} & P_{G2}, as well as the transmitted power, P_{OC}, through a fixed output coupler of known reflectivity, T_{OC}. The output from a given laser output port is the intrac-

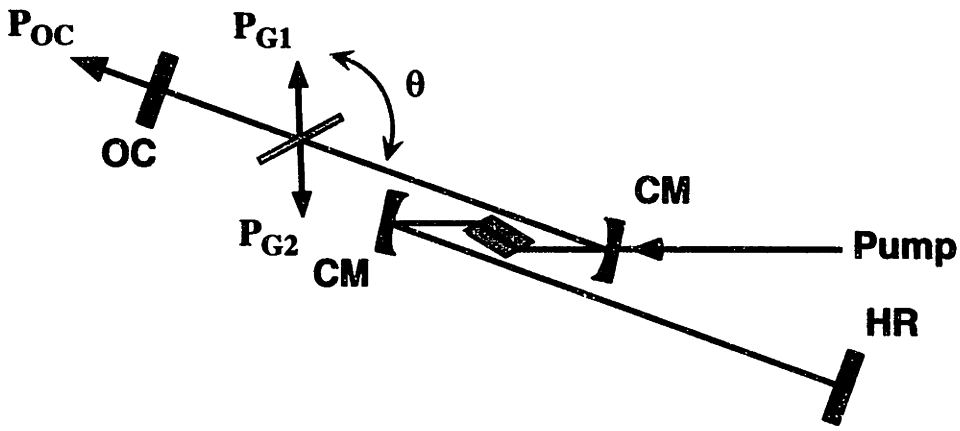

FIGURE 3-6: Symmetric z-cavity: OC, output coupler; CM's, 100 mm radius-of-curvature folding mirrors; HR, high reflector. A thin glass window is inserted in the cavity to implement a continuously variable output coupler by changing the angle of incidence θ; in general $P_{G1}=P_{G2}$.

avity power multiplied by the output coupling coefficient attributed to a given optical element. The exact total output coupling of the window, T_{G0}, can thus be determined using the following relations

$$\left.\begin{aligned} P_{OC} &= P_{in}\cdot T_{OC} \\ P_{G1} &= P_{in}\cdot R_{G1} \\ P_{G2} &= P_{in}\cdot R_{G2} \end{aligned}\right\} \Rightarrow R_{G1}+R_{G2} = \frac{T_{OC}}{P_{OC}}(P_{G1}+P_{G2}) = T_{G0}. \qquad (3\text{-}1)$$

In general when a simple thin glass window is used $P_{G1}\cong P_{G2}$ and the power on only one side of the slide needs to be measured. Figure 3-7 shows the data obtained for calibrating the effective output coupling of the window used in this study. The window angle, θ, is defined as the declination from the intracavity beam path, with zero defined as the point where the window is normal to intracavity mode. To verify the angular dependence of the output coupling data in Figure 3-7 a fit

to the theoretical reflectivity of a glass window close to Brewster's angle can be performed. The functional dependence can be mathematically expressed as:

$$T_{G0}(\theta) = 4 \cdot \frac{\tan\left(\theta - \operatorname{asin}\left(\frac{1}{n}\sin(\theta)\right)\right)^2}{\tan\left(\theta + \operatorname{asin}\left(\frac{1}{n}\sin(\theta)\right)\right)^2}. \qquad (3\text{-}2)$$

A best-fit to the data in Figure 3-7 was performed using equation 3-2 with the glass index of refraction, n, as a free parameter. The factor of four is to account for the fact that a glass plate in actuality consists of four reflective surfaces each at an angle θ to the normal. A good correspondence between the measured reflectivity data and the best-fit of equation 3-2 can be observed.

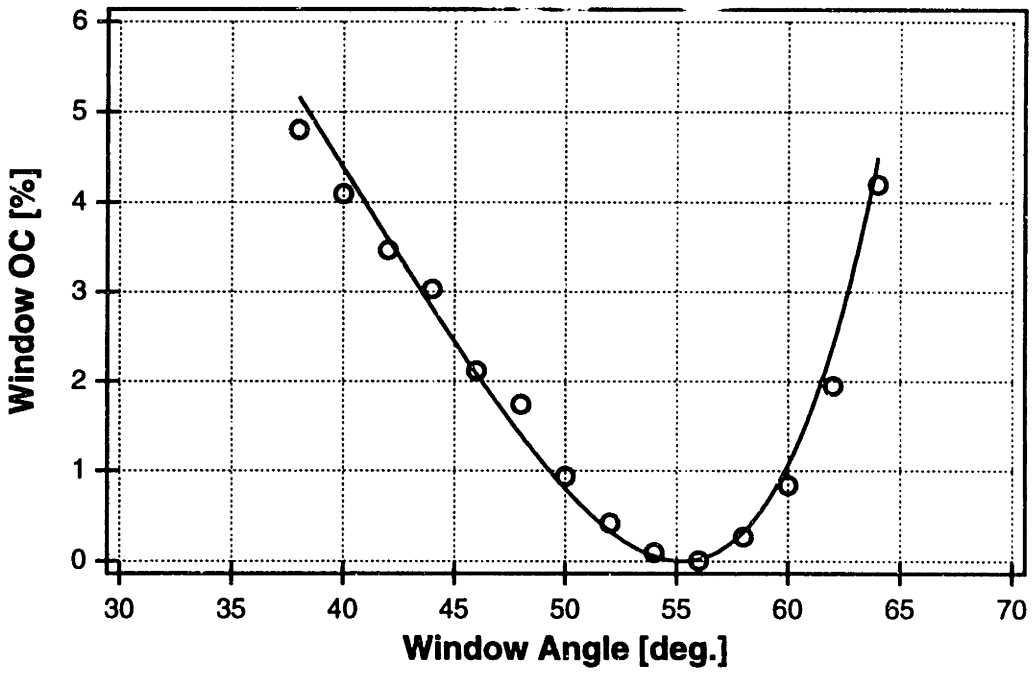

FIGURE 3-7: The data points represent the measured glass window output coupling as a function of glass window angle. The solid line is the best-fit to the data using the index of refraction of the glass window as a free parameter.

Unsaturated gain and parasitic loss measurement

To measure the unsaturated gain and parasitic loss for the *a*- and *c*-axis lasers the absorbed threshold power was measured for a number of output couplers ranging from 0.2-5.4%. For a laser at threshold the unsaturated (small signal) gain is always equal to the cavity loss such that:

$$Re^{-2(\alpha-\gamma P_{th})L} = 1 \tag{3-3}$$

where γ is the gain coefficient in $[(W\cdot cm)^{-1}]$, P_{th} is the absorbed pump power at threshold in [W], α is the loss per unit length $[cm^{-1}]$ in the gain crystal, L is the crystal length in [cm], and R is the net reflectivity of all the cavity mirrors. From equation (3-3) a linear relationship can be established relating the measured quantities P_{th}, R and L, to the unknown quantities α and γ such that:

$$P_{th} = -\frac{1}{2\gamma L}\ln(R) + \frac{\alpha}{\gamma} \tag{3-4}$$

The measured absorbed pump power at threshold is presented in Figure 3-8 as a function of the natural logarithm of the output coupler reflectivity. This allows for the use of equation (3-4) in extracting the loss and unsaturated crystal gain coefficient. If a linear polynomial fit is applied to the data in Figure 3-8, the loss per pass α, and gain coefficient γ can be extracted. The polynomial curve fit parameters, A and B, can be matched to the corresponding terms in equation (3-4) such that

$$P_{th} = -\frac{1}{2\gamma L}\ln(R) + \frac{\alpha}{\gamma} = -A\ln(R) + B \tag{3-5}$$

$$\text{where } A = \frac{1}{2\gamma L} \text{ and } B = \frac{\alpha}{\gamma}. \tag{3-6}$$

The calculated parameters for both, the *a*-axis and *c*-axis, Cr^{4+}:forsterite crystals are shown in Table 3-2.

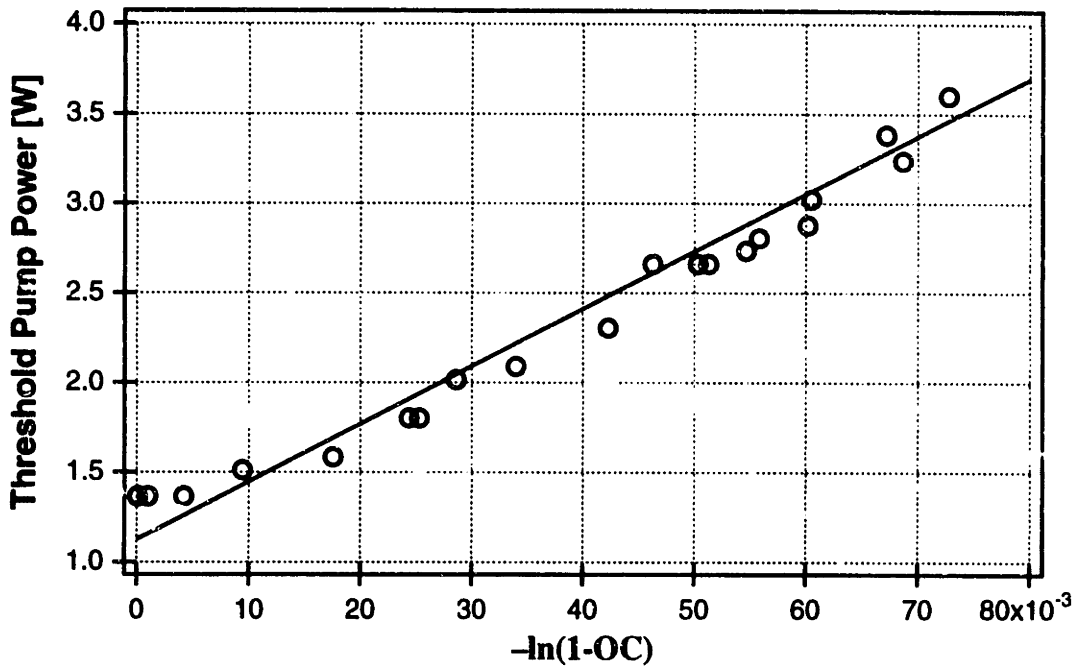

(a)

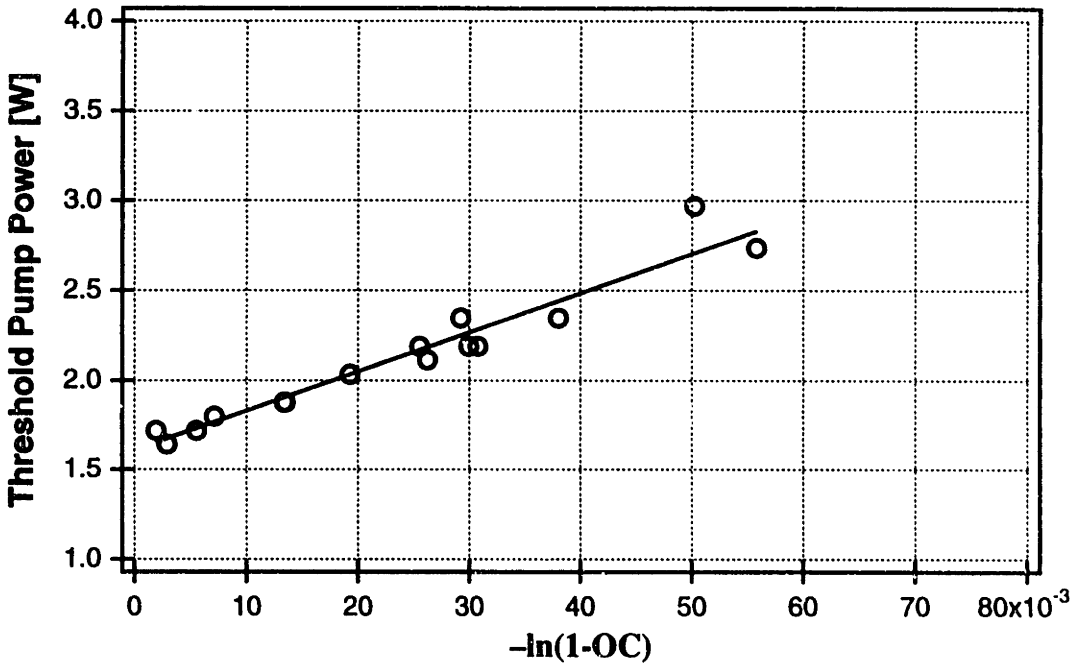

(b)

FIGURE 3-8: Absorbed pump power at threshold versus the logarithm of the output coupler reflectivity for the (a) *a*-axis laser and (b) *c*-axis laser.

TABLE 3-2: Extrapolated values for the a-axis and c-axis Cr^{4+}:Forsterite cw lasers: the loss per unit length, α; single pass loss; gain coefficient, γ; and limiting slope efficiency, η_0.

	a-axis	c-axis
α [cm^{-1}]	0.0097	0.0185
loss per pass	1.75%	3.70%
γ [$(W \cdot cm)^{-1}$]	0.0087	0.0115
η_0	0.30±0.03	0.27±0.07

Limiting slope efficiency

The limiting slope efficiency is the best possible performance for a laser crystal if all parasitic losses in the crystal were eliminated. This quantity can not be measured directly, thus it has to be extracted from observable physical quantities. In general the slope efficiency η_s of an actual cw laser-pumped laser can be derived from energy conservation such that

$$\eta_s = \eta_p \cdot \frac{\lambda_P}{\lambda_L} \cdot \frac{\text{Output Coupling}}{\text{total RT loss}} = \eta_p \cdot \frac{\lambda_P}{\lambda_L} \cdot \frac{1-R}{1-Re^{-2\alpha L}} \tag{3-7}$$

where the quantity λ_P/λ_L which is the ratio of the pump and lasing wavelengths commonly referred to as the quantum limit for a laser, and η_P is a term to account for a possible non-unity pump absorption [46]. In a typical laser system a few assumptions can be made regarding the total output coupling, C=1–R«1, and total round-trip loss, L=1–$e^{-2\alpha L}$≈2αL«1. Using this notation and CL«1 the total loss in the laser can be simplified to

$$\begin{aligned} 1 - Re^{-2\alpha L} &= 1 - R(1 - 2\alpha L) \\ &= C + L - CL \\ &\approx C + L \ . \end{aligned} \tag{3-8}$$

Using equation (3-8), equation (3-7) can be simplified such that

$$\eta_s = \eta_{pP} \cdot \frac{\lambda_P}{\lambda_L} \cdot \frac{C}{C+L} = \eta_{pP} \cdot \frac{\lambda_P}{\lambda_L} \cdot \left(1 + \frac{L}{C}\right)^{-1} = \eta_0 \cdot \left(1 + \frac{L}{C}\right)^{-1}, \tag{3-9}$$

where η_0 is the limiting slope efficiency. Thus, the limiting slope efficiency, η_0 can be related to measurable physical quantities, the output slope efficiency η_S, the parasitic absorption α, the crystal length, and the total reflectivity of the optical components:

$$\eta_0 = \eta_S \cdot \left(1 + \frac{2\alpha L}{1-R}\right). \tag{3-10}$$

Using the slope efficiencies obtained from linear fits to the data in Figure 3-8, limiting slope efficiencies of η_0=0.30±0.03 for the *a*-axis and η_0=0.27±0.07 for the *c*-axis were obtained. The cw slope efficiencies for both, the *a*-axis and *c*-axis, crystals are lower than that measured using laser crystal at cryogenic temperature of η_0=0.42±0.11 [40] or that obtained using a chopped cw (15:1) pump beam, η_0=0.65±0.10 [43]. This discrepancy may be the result of thermal parasitic loss mechanisms, thermal lensing, as well as temperature dependent phonon broadening effects on the lineshape. The experimental conditions in these references are sufficiently different that it is difficult to establish good quantitative comparison. However, both the *a*-axis and *c*-axis crystals yielded comparable limiting slope efficiencies. When comparing the data shown in Table 3-2 it can be seen that the *c*-axis crystal has a less favorable parasitic loss coefficient, but has a higher gain coefficient than the *a*-axis crystal. Thus, if imperfections in crystal growth and polishing can be eliminated both forsterite crystals should, in principle, operate lasers with comparable slope efficiency.

The values for the limiting slope efficiencies were obtained by averaging the slope efficiencies in Table 3-1 and the parasitic absorption coefficient obtained from the line fit in Figure 3-8. In this approach the statistical error in the limiting slope efficiency is reduced by increasing the number of output couplers and extrapolated slope efficiencies in Table 3-1. An alternate approach is to plot the slope efficiency η_S as a function of the inverse output coupling and applying a linear fit commensurate with equation (3-10). This linear fit results in two parameters which can be used to extract the limiting slope efficiency and the parasitic absorption coefficient. When applying this

alternate approach to reduce the systematic error in evaluating the limiting slope efficiency, it is beneficial to have a range of output couplers of evenly spaced values in the 1/(1-R) space [40][47]. This approach however, relies on measuring the slope efficiency at each output coupler; process which requires the acquisition of a large number of data points. An example of calculating the limiting slope efficiency of a cw laser using either method is shown in section 4.3.2.

3.2.4 CW laser wavelength tuning

In comparing the performance of a-axis and c-axis lasers the cw tuning range needs to be investigated. When comparing the fluorescence of the two laser crystals an upper limit on the tuning range can be set. However, this does not necessarily reflect the actual laser tuning range. For the purpose of establishing the tuning range of these lasers a 1.5 mm thick quartz birefringent plate was placed within both laser cavities. By rotating the birefringent plate the laser output wavelength can be continuously tuned. Careful care was taken that the tuning range was not limited by the free-spectral range of the birefringent filter.

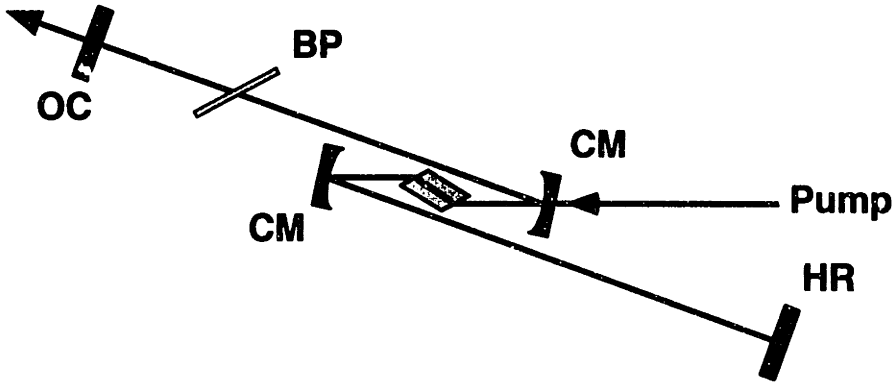

FIGURE 3-9: Symmetric z-cavity: OC, output coupler; CM's, 100 mm radius-of-curvature folding mirrors; HR, high reflector. A a 1.5 mm thick birefringent plate is inserted at Brewster's angle for wavelength tuning of the laser.

Both lasers were continuously tunable from 1205 to 1330 nm (see Figure 3-10). Moreover, the bandwidths for the high-reflectors and output couplers were well in excess of the attained tuning ranges. The free running lasing wavelength without a birefringent filter in the cavity overlapped with the peak of the tuning curve for both crystals. On the short wavelength side the laser

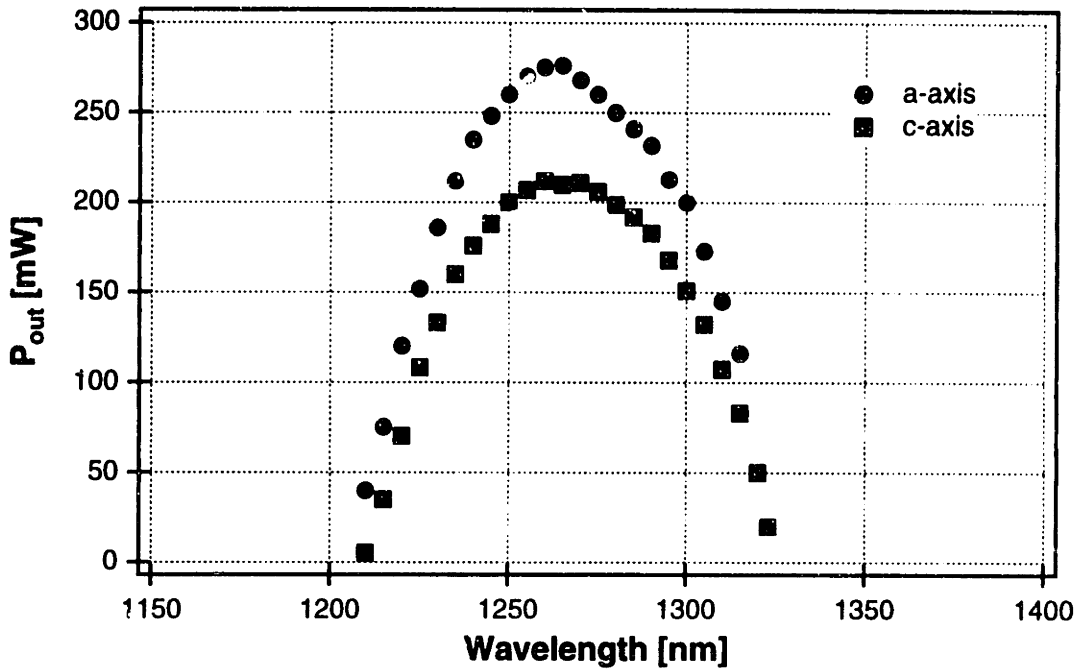

FIGURE 3-10: Tuning range for lasers using the a-axis and c-axis crystals. A birefringent filter was inserted in the cavity for continuous wavelength selection

tuning range seems to be limited by the onset of the broad absorption band in forsterite. The absorption onset for wavelengths shorter than 1200 nm is quite steep, and is in agreement with the short-wavelength tuning limit. On the long wavelength side the tuning limitation is not as clear, but may be explained by a drop in the gain which follows the drop in the fluorescence emission spectrum. The cw tuning range for both crystals was found to be the same and is comparable with the largest cw tuning range reported for Cr^{4+}:forsterite lasers pumped at 1064 nm [44].

3.3 Mode-locked Cr^{4+}:forsterite

The process of modelocking is where a number of oscillating longitudinal axial laser resonator modes are made to have a definite steady-state relative phase relationship. As a result, the temporal output of such mode-locked lasers consists of a train of pulses, the temporal durations of which are inversely proportional to the frequency bandwidth over which the longitudinal modes maintain a definite relative phase. The temporal separation between optical pulses is set by the laser round-trip time. Modelocking techniques can be separated into two general categories, active modelocking schemes and passive modelocking schemes, both of which have been exten-

sively studied and reviewed in the literature. Active modelocking techniques can be divided into two categories, intracavity modulation of the cavity loss on the pulse round-trip time (typically acousto-optic modulation), and synchronous gain pumping. Both of these methods require precise cavity stabilization so that the loss/gain modulation occurs precisely at the cavity round-trip time, and practical implementation generally limit pulse durations to on the order of picoseconds. As the name indicates, passive modelocking techniques are those for which non-linear processes intrinsic to the laser result in the optical pulse generation. Over the years, a number of passive modelocking schemes were developed including colliding pulse modelocking [48], additive pulse modelocking [49][50], and Kerr-lens modelocking [3][51]. Kerr-lens modelocking is to date one of the most frequently used modelocking mechanism for femtosecond pulse generation with solid-state lasers. The shortest optical pulses obtained, to-date, directly from a lasers oscillator are 6.5 fs in duration using a Kerr-lens mode-locked Ti:Al_2O_3 laser [4].

3.3.1 Kerr-lens mode-locked Cr^{4+}:forsterite laser

The large bandwidth of Cr^{4+}:forsterite makes this gain crystal a suitable candidate for the generation of ultrashort optical pulses in the 1.3 μm wavelength range. The cw tuning range of Cr^{4+}:forsterite is almost 90 nm (FWHM), and therefore pulses as short as 19 fs should theoretically be attainable from this material if laser optics can support that bandwidth and if pulse broadening can be suppressed by minimizing and compensating higher order dispersive effects [52]. Initial work in modelocking Cr^{4+}:forsterite lasers was done using active modelocking and synchronously pumped modelocking to achieve picosecond pulses [53], and this was followed by 60 fs pulse generation by active modelocking in conjunction with dispersion compensation [54]. The first passively mode-locked Cr^{4+}:forsterite lasers were based on additive-pulse modelocking [55], and were followed by Kerr-lens mode-locked laser implementations [56][57][58]. Pulse durations as short as 25 fs have been generated using Kerr-lens modelocking in Nd:YAG pumped Cr^{4+}:forstertie systems [59]. Self-starting Kerr-lens mode-locked implementations can be achieved using semiconductor saturable-absorber mirrors [60][61], and more recently color glasses were reported for use in self-starting mode-locked Cr^{4+}:forsterite lasers [62].

The Kerr-lens mode-locked resonator used in this study was a standard z-cavity formed by a pair of 100 mm radius-of-curvature folding mirrors, a high-reflector, a 6% output coupler, and arm lengths of 80 and 120 cm. A 10.0 mm long Brewster-cut Cr^{4+}:forsterite gain crystal of 0.3% at. wt. Cr was mounted in a water-cooled copper heat-sink mount and typically maintained at 10°C. The crystal was cut for pump propagation along the *a*-axis and the incident polarization parallel to the *b*-axis. The Cr^{4+}:forsterite crystal was pumped by the 1064 nm emission from a diode-excited Nd:YAG laser, *Power Path Technology* Model 7C/600. This pump laser was able to generate up to 7 W of cw output power in a TEM_{00} (M^2<1.25) output beam. The unit was powered by a standard 8 A/115 Vac/60 Hz electrical supply, and was equipped with an external closed-circuit chiller for water cooling of the laser diodes. Dispersion compensation was achieved by a double-pass sequence of Shott Glass SF6 prisms placed in the 120 cm long resonator arm. The prism separation was experimentally optimized and set to 23 cm.

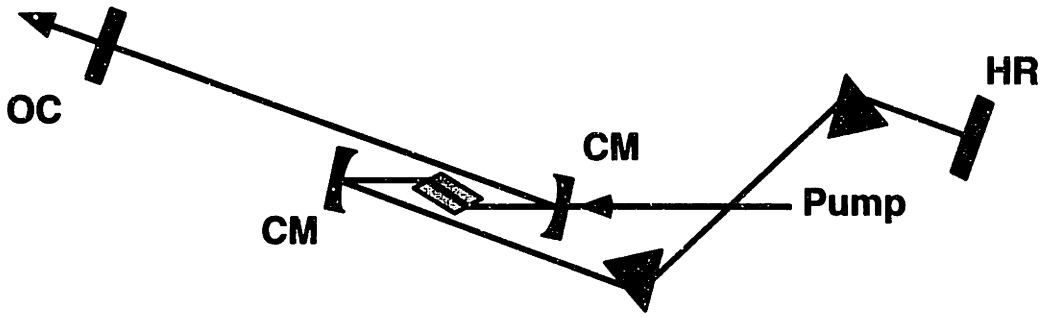

FIGURE 3-11: Schematic diagram of a standard z-cavity Kerr-lens mode-locked Cr^{4+}:forsterite laser resonator: OC, output coupler; CM's, 10 cm radius-of-curvature folding mirrors; HR, high reflector. A pair of SF6 prisms, separated by 23 cm, was used for dispersion compensation. The pump laser was a cw diode-excited Nd:YAG laser.

The laser was typically operated with 5 W of incident power resulting in a mode-locked output of about 300 mW, and a modelocking threshold of 4 W (cw threshold 1.5 W). Modelocking could be initiated by a mechanical perturbation of the cavity, typically by displacing one of the dispersion compensating prisms. The typical output spectrum for this laser had a FWHM of 50 nm. Long term stability was attained by enclosing the laser into an acrylic box to reduce air currents.

To eliminate the need for a user initiated mechanical perturbation to initiate modelocking, the system was modified for regenerative modelocking. The laser cavity in Figure 3-11 was changed to accommodate an 11 mm long Brewster-cut fused-silica acousto-optic modulator (AOM) in the shorter resonator arm. In cw solid-state lasers, there is continuous competition between several longitudinal resonator modes. This mode competition results in a modulation at the cavity round-trip time. In a mode-locked system using regenerative initiation, the cavity beat signal is detected and amplified, processed, and used in a feedback loop to drive the AOM. The phase of the signal is adjusted such that the AOM would have a maximum in transmission when a pulse is present. Low-pass filters at the input and output eliminate any high frequency noise and higher cavity harmonics and the frequency divider is necessary for driving an acousto-optic amplitude modulator [63]. Slight changes in cavity round-trip time are tracked by the feedback circuitry assuring that the AOM is driven at a rate and phase commensurate with the cavity round-trip time. Regenerative modelocking (active modelocking) provides the initial perturbation necessary to initiate Kerr-lens modelocking and allow for highly stable long term operation.

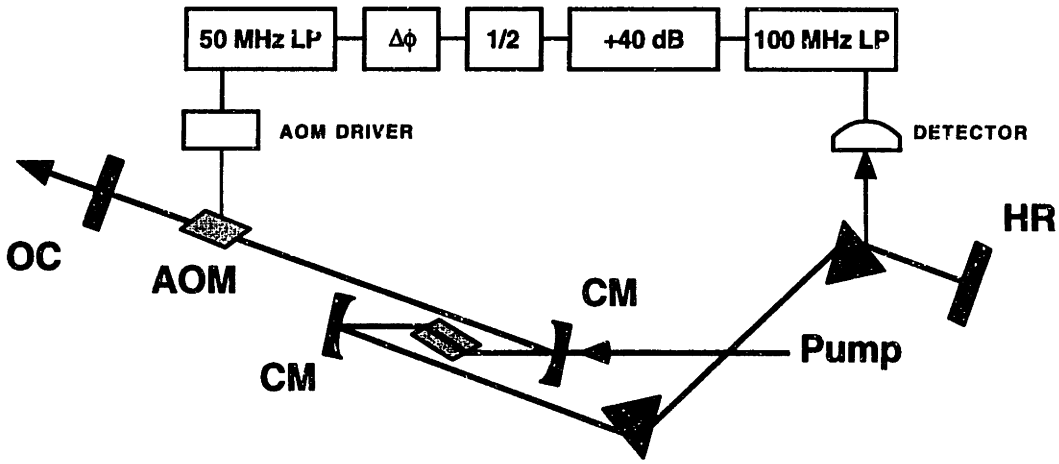

FIGURE 3-12: Regenerative mode-locked Cr^{4+}:forsterite laser system. A standard z-cavity Kerr-lens mode-locked Cr^{4+}:forsterite laser resonator: OC, output coupler; CM's, 10 cm radius-of-curvature folding mirrors; HR, high reflector; AOM, acousto-optic modulator. A pair of SF6 prisms, separated by 23 cm, was used for dispersion compensation. The pump laser was a cw diode-excited Nd:YAG laser.

3.3.2 Short coherence length Cr^{4+}:forsterite laser sources

Mode-locked lasers are commonly used for studying ultrafast dynamics in various applications ranging form solid-state physics to chemistry. In recent years a new application of mode-locked solid-state lasers emerged as their intrinsic short coherence length is of interest for optical coherence tomography (OCT) medical imaging [64][65][66]. Unlike in ultrafast spectroscopy, the temporal properties of optical pulses are not of primary interest in OCT applications, instead the broad bandwidth and consequent short coherence length are utilized. In addition to the broad emission bandwidths, mode-locked lasers typically have high single transverse mode output powers making them ideally suited for coupling into standard single-mode optical fiber delivery systems which are the basis of most OCT system implementations.

Optical coherence tomography is an application of a well established ranging technique referred to as optical coherence domain reflectometry (OCDR) [67][68]. OCDR systems can be used for performing axial distance measurements in free-space and scattering media with high spatial resolution [69]. In OCDR a broadband light source illuminates a Michelson interferometer in which one arm is terminated by a target sample and the other arm is a reference arm in which a moving mirror scans over the axial dimensions of the sample. Interference is observed when the path lengths traveled by reflections from the sample and the reference mirror coincide to within a coherence length. OCDR systems utilize broad-band light sources and perform with spatial resolutions which are inversely proportional to the source bandwidth. In addition, the source has to have a well behaved spectrum for which the Fourier-transform (the interferogram from a scanning Michelson interferometer) does not have many side-bands. To measure the suitability of a source for use on high-resolution OCDR systems the output of a scanning Michelson interferometer is measured. The measured electric field (linear) autocorrelation is referred to as the point-spread-function and its FWHM determines the axial system resolution. In effect, this is a measurement of the laser coherence length. For the case of top-hat-like spectra, the autocorrelation would have considerable side-bands, thus making the source unsuitable for OCDR applications.

To determine the resolution of a mode-locked Cr^{4+}:forsterite laser used for OCDR applications a fiberoptic Michelson interferometer was implemented. The diagnostic system consisted of two single-mode (Corning SMF-28™ CPC6), wavelength-flattened 50/50 fiber splitters, forming

a Michelson interferometer with dual balanced detection. The bandwidth of the fiber-optic components was able to support a 200 nm spectrum centered at 1.3 μm. Both interferometer arms were terminated with high-reflectors, of which one was mounted on a *General Scanning* linear galvanometric actuator. The scanning galvanometer was swept in a sawtooth motion with a velocity of 30 mm/s which induced a Doppler frequency in the reflected light of 50 kHz. Interferograms measured at the output port were bandpass filtered, demodulated, digitized, and stored on a computer.

Measurements of the spectrum and the point-spread-function of the Cr^{4+}:forsterite laser using regenerative modelocking, shown in Figure 3-12, were conducted. The bandwidth of the measured spectrum had a FWHM of 50 nm and the point-spread-function had a FWHM of 15 μm. The theoretical point-spread-function of a free-space OCDR system, ΔL, when the source has a Gaussian spectrum with a FWHM bandwidth, $\Delta\lambda$, and a center wavelength, λ_0, can be calculated to be [70]:

$$\Delta L = \frac{2\ln(2)}{\pi}\frac{\lambda_0^2}{\Delta\lambda} \tag{3-11}$$

The experimental value for the axial resolution is in close agreement with the value calculated from the measured spectrum. For ranging and imaging applications it is desirable to achieve higher spatial resolution than is possible with the bandwidth of the direct laser output.

To increase the spatial resolution, the high peak power of the pulses from the laser can be used for nonlinear broadening of the laser output spectrum through self-phase modulation. Previous studies of the propagation of high peak-power sub-100 fs pulses in standard single-mode fibers have identified four-photon mixing and stimulated Raman scattering as the dominant mechanism that give rise to a modulated spectrum. However, the use of dispersion-shifted fiber eliminates the phase matching necessary to support four-photon mixing and permits the generation of a smooth broadened spectrum whose dominant spectral features are governed by self-phase modulation and normal dispersion [71]. The mode-locked output of the Cr^{4+}:forsterite laser was coupled into a single-mode Corning SMF/DS™ CPC6 dispersion shifted fiber such that 100 mW were delivered into the fiber core. The demodulated field autocorrelation function resulted in a

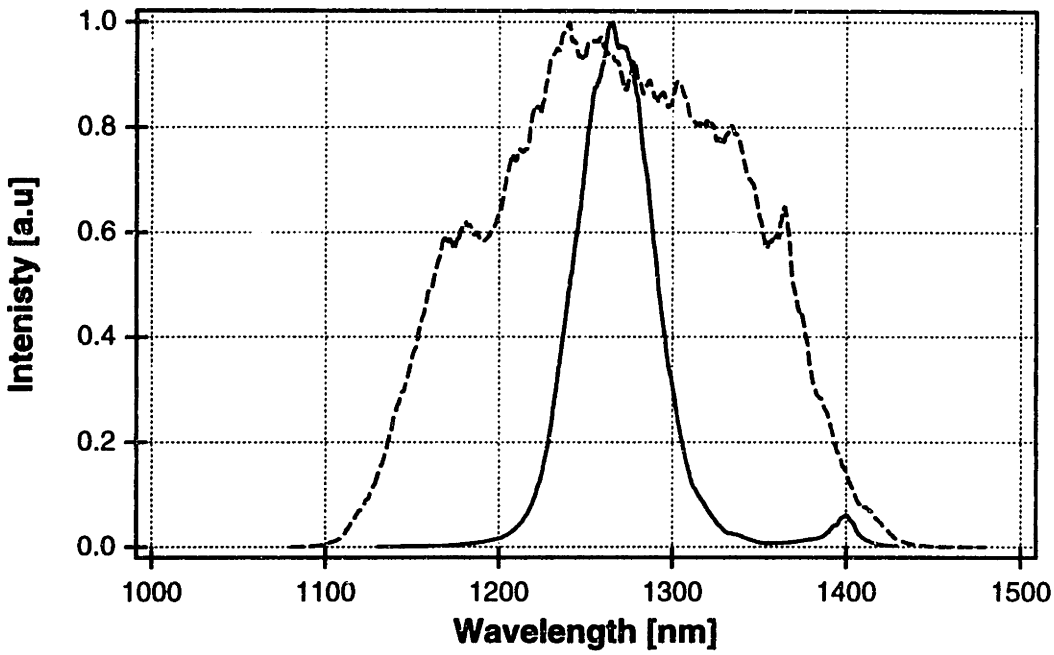

(a)

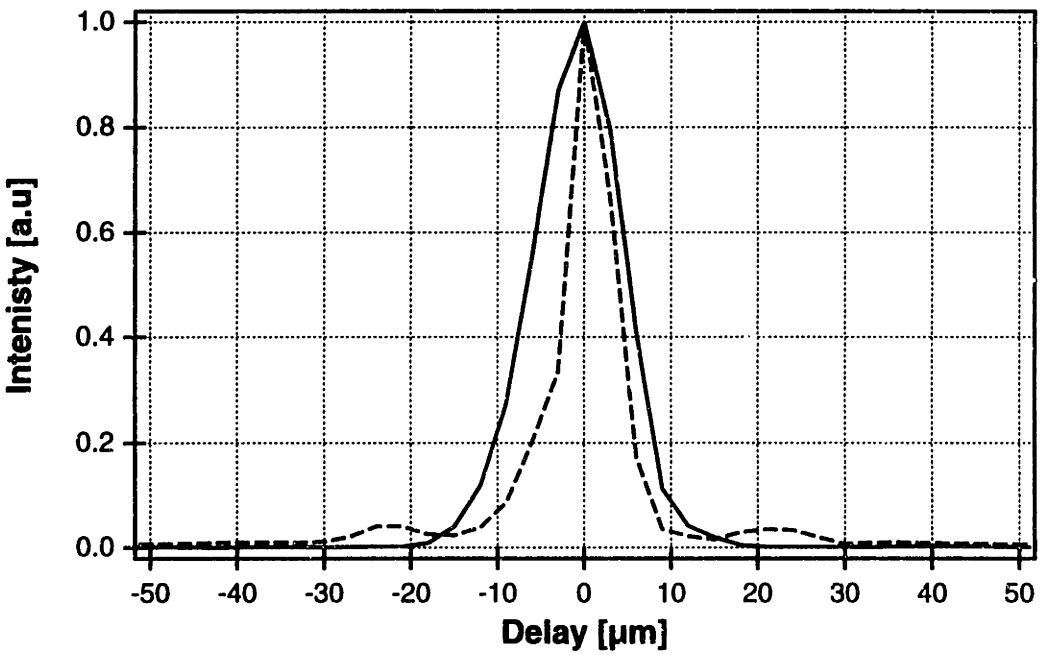

(b)

FIGURE 3-13: (a) Output spectrum form the mode-locked Cr^{4+}:forsterite laser and (b) corresponding coherence envelopes (point-spread-functions). The solid lines are the data directly from the KLM laser; dashed lines are the data after coupling into a section of dispersion-shifted single-mode fiber.

FWHM coherence length of 6 μm [65]. The experimental autocorrelation function envelopes shown in Figure 3-13b, are in close agreement with the traces shown in figure Figure 3-14 which represent the calculated values using the acquired spectra shown in Figure 3-13a.

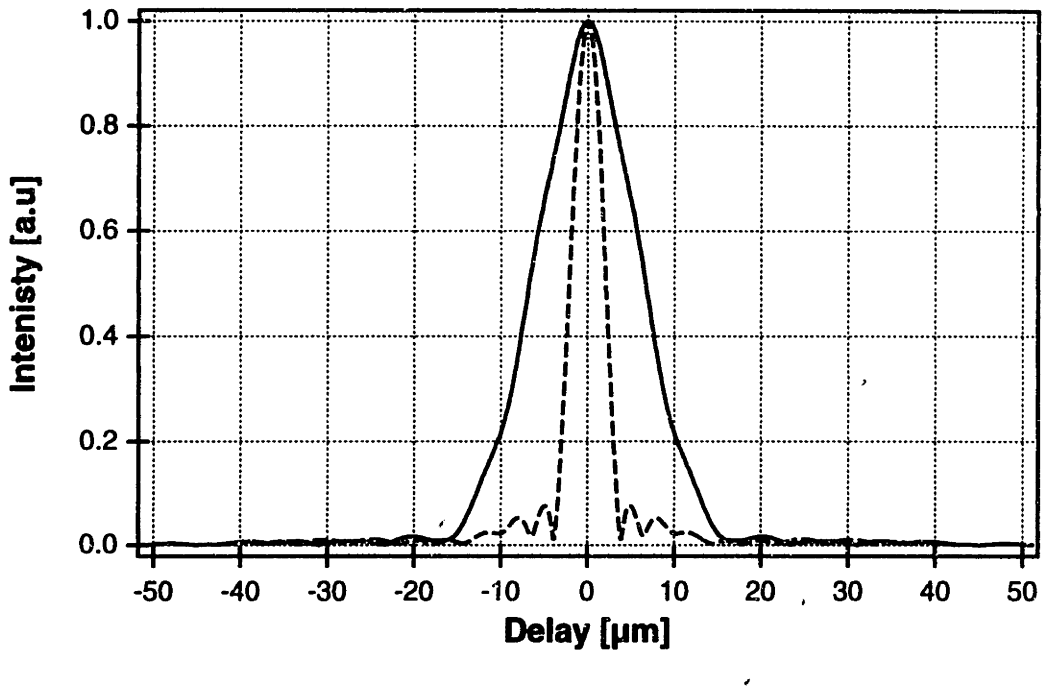

FIGURE 3-14: Calculated coherence envelopes (point-spread-functions) for source spectra shown in Figure 3-13a The solid lines are the data directly from the KLM laser; dashed lines are the data after coupling into a section of dispersion-shifted single-mode fiber

In summary, an all-solid-state Kerr-lens mode-locked Cr^{4+}:forsterite laser source can be used as a low-coherence-length source for high-resolution optical coherence domain ranging. In addition, taking advantage of high peak intensities associated with femtosecond pulse trains, the spectral bandwidth of the source can be increased thereby decreasing the axial point-spread-function, using self-phase modulation in a singe-mode optical fiber. The 1.3 μm wavelength of this source is well placed to take advantage of the favorable window in the absorption and scattering cross sections of biological tissue. Thus, all-solid-state implementations of mode-locked Cr^{4+}:forsterite lasers have applications in ultrafast spectroscopy as well as in optical coherence reflectometry and optical coherence tomography applications [66][65]. Kerr-lens mode-locked Cr^{4+}:forsterite lasers using regeneratively initiated modelocking can be implemented as turn-key systems with long-term stable operation for various applications.

Chapter 4

Near-IR pumping of Cr^{4+}:forsterite

4.1 Introduction

In order to implement a widely accepted and commercially viable laser system, it is necessary to assure that such system is compact, robust and of low cost. Many lasers traditionally use rather expensive and large pump lasers to attain the population inversion required to provide gain. Such pump lasers often require high power supply currents and external water cooling, making them difficult to use outside the research laboratory environment. One class of frequently used pump lasers for Cr^{4+}:forsterite are flashlamp-pumped Nd:YAG lasers. In these systems gas discharge lamps are used to optically excite Nd:YAG crystal rods and to generate the population inversion. This design gained wide-spread acceptance because of its low cost and simple power supply design [72]. However, low power efficiency spurred significant research and development efforts toward the implementation of new, more efficient, and compact pump laser sources which can be used in conjunction with existing laser gain media. Recently pump lasers using high-power diode laser arrays resulted in the introduction of various diode-pumped pump-laser systems. Diode-pumped alternatives to argon-ion lasers are starting to become commercially available and are allowing for more compact and robust implementations of Ti:Al_2O_3 lasers. Similarly, diode-pumped alternatives to traditional flash-lamp pumped Nd:YAG lasers are commercially available from a number of manufacturers. These lasers have typically a better noise figure than lamp pumped or ion lasers and also physically more compact systems. However, the non-diffraction limited emission geometry of laser diode arrays does not allow for a very efficient spatial overlap between the diode-array emission and the laser resonator mode. Consequently, even though the narrow spectral characteristics of laser diodes result in much better power delivery into the useful crystal absorption bands compared to lamp-pumped systems, there is still a significant power loss

due to the emission geometry. Diode-pumped replacements of Nd:YAG (and ion) lasers represent a significant advance in laser development, however due to their still considerable power consumption these systems are generally not compact enough for the implementation of table top or for mobile applications with low power consumption is desired.

An alternate approach to implementing compact, robust and low cost laser systems is the development of direct diode-pumped solid-state lasers. Such lasers have gain materials which can be directly pumped by low-cost semiconductor lasers diodes. Work on such gain materials has resulted in the Cr^{3+}:$LiSrAlF_6$, Cr^{3+}:$LiCaAlF_6$, and Cr^{3+}:$LiSrGaF_6$ which gain materials in the 800-900 nm wavelength region and can be used in conjunction with 670 nm semiconductor diode pump sources. This chapter discuses the implementation of Cr^{4+}:forsterite lasers using pump wavelengths in the near-infrared. Choice of this pump wavelength region is different from the commonly used 1064 nm absorption region and is of interest because these wavelengths are accessible by a wide range of semiconductor laser diodes making the implementation of compact and robust 1.3 μm laser sources possible. A systematic characterization of Cr^{4+}:forsterite cw operation was performed by Carrig *et al.* in reference [40]. This work demonstrated lasing at a number of pump wavelengths ranging from 647-1064 nm. However, room-temperature cw operation was only achieved using the Nd:YAG pump laser whereas at other pump wavelengths lasing was achieved only by cooling the crystal to cryogenic temperatures. The work presented in this chapter focuses on the implementation of a room-temperature operated Cr^{4+}:forsterite laser using near-IR pump wavelengths.

4.2 Near-IR spectroscopic properties of Cr^{4+}:forsterite

The efficient use of low cost, multimode semiconductor laser diodes for pumping solid state lasers requires the use of short gain crystals. Short gain crystals are important for efficient mode-matching of the laser resonator modes to the emission of the diode lasers. Also, short crystal lengths are important in optimizing short-pulse operation of femtosecond Kerr-lens mode-locked lasers to reduce effects of higher-order dispersion, which can in turn limit pulse duration. Past spectroscopic studies on Cr^{4+}:forsterite [40] indicate that the absorption coefficients in the near-infrared is sufficiently large the be considered for the use of gain crystals shorter than 5 mm.

4.2.1 Near-IR absorption

Measurement of absorption coefficients in Cr^{4+}:forsterite show that the absorption in the near-IR peaks at 740 nm and is significantly higher than at the commonly used 1064 nm pump wavelength. A cw *Coherent Mira 900* Ti:Al_2O_3 laser was operated using the short wavelength mirror set allowing for the laser emission to be tuned from 670 nm to 820 nm. Measurements of the absorption coefficient were conducted on a 3 mm long, Brewster-cut, Cr^{4+}:forsterite crystal of doping density 0.3% at. Cr. This material is of the same kind as typically used for 1064 nm pumped Cr^{4+}:forsterite systems. The Ti:Al_2O_3 laser was tuned to the desired wavelength, propagated along the crystallographic a-axis with the polarization oriented along the crystallographic *b*-axis and commensurate with the Brewster crystal interface. Power measurements were taken of the incident and transmitted radiation which were used to measure the absorption coefficients at selected wavelengths. The measured absorption coefficient in Cr^{4+}:forsterite peaks at 740 nm

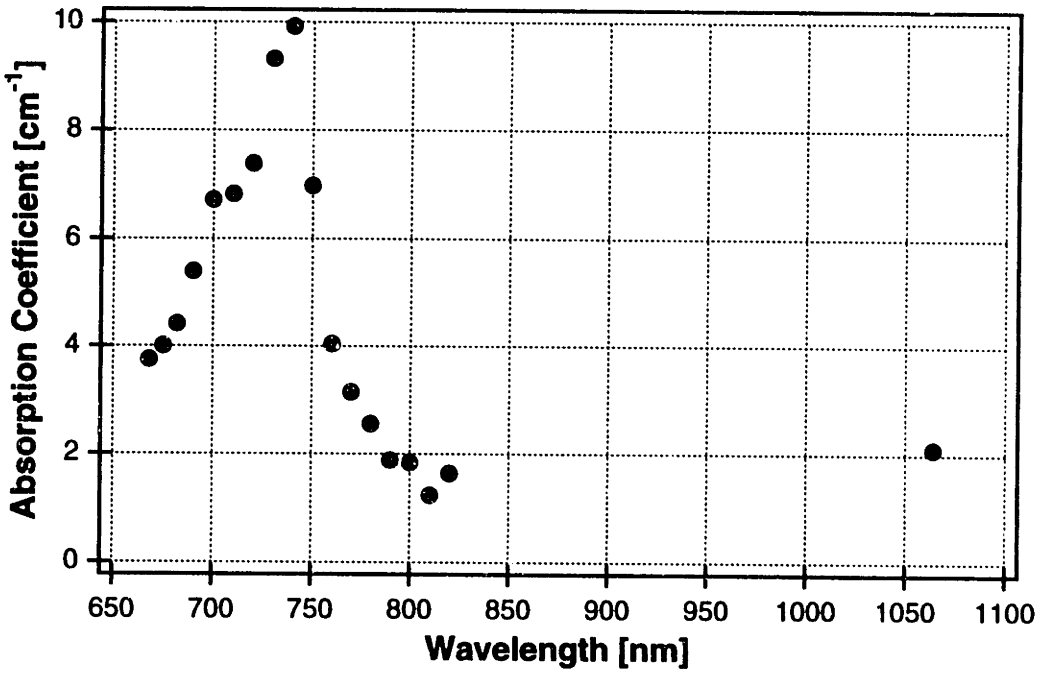

FIGURE 4-1: Cr^{4+}:forsterite absorption coefficients for various wavelengths between 670-820nm. On the right, the absorption coefficient for the commonly used 1064 nm pump wavelength.

where it is significantly larger than at the commonly used 1064 nm Cr^{4+}:forsterite pump wavelength. Typical crystal lengths for laser design are selected such that the total absorbed power in

the gain crystal is about 85-90%. In general it is problematic to fabricate forsterite laser crystals with high doping densities of Cr^{4+} without introducing increased loss at the emission wavelengths. Thus, an increase in the absorption coefficients makes it possible to use thinner crystals without the need for an increase in doping densities.

Shorter crystal lengths result in a reduction of the parasitic absorption at the lasing wavelength and a higher figure of merit. The figure of merit is defined as the ratio of absorption at the pump wavelength to absorption at the emission wavelength:

$$FOM = \frac{\alpha(pump)}{\alpha(emission)}. \tag{4-1}$$

The absorption at the laser emission wavelength was measured as α(1260 nm)=0.0217 cm^{-1}. Using equation (4-1) the figure of merit using 740 nm excitation can be calculated to be 470, whereas for a 1064 nm excitation it is about 90. The figure of merit can, in general, be increased by either increasing absorption coefficient, or improving the quality of the crystal resulting in a diminished parasitic absorption at the lasing wavelength. By using a near-IR pump wavelength the pump absorption coefficient was, in-effect, increased without the need for changing the crystal growth parameters which resulted in laser gain crystals with a more favorable figure-of-merit. High crystal doping densities are in general problematic because they also result in increased parasitic absorption and this in turn decreases the FOM.

4.2.2 Near-IR fluorescence

One of the attractive features of Cr^{4+}:forsterite laser systems is that they have a broad emission band in the 1.3 μm wavelength region. In considering the use of near-IR pump wavelengths for use with Cr^{4+}:forsterite gain crystals it is necessary to assure that the emission spectrum is commensurate with the one obtained when using a 1064 nm pump source. The laser transition levels involved in Cr^{4+}:forsterite systems are shown in Figure 4-2. It can be seen that when using near-IR pump wavelengths the absorption results in the $^3A_2 \rightarrow {}^3T_1$ transition and through a non-radiative decay path the excited state level, $^3T_2$, is accessed, which is the same excited state level involved in systems using a 1064 nm pump excitation. However, if the pump polarization is oriented parallel to the a-axis excited-state-absorption effects can preclude efficient pumping and

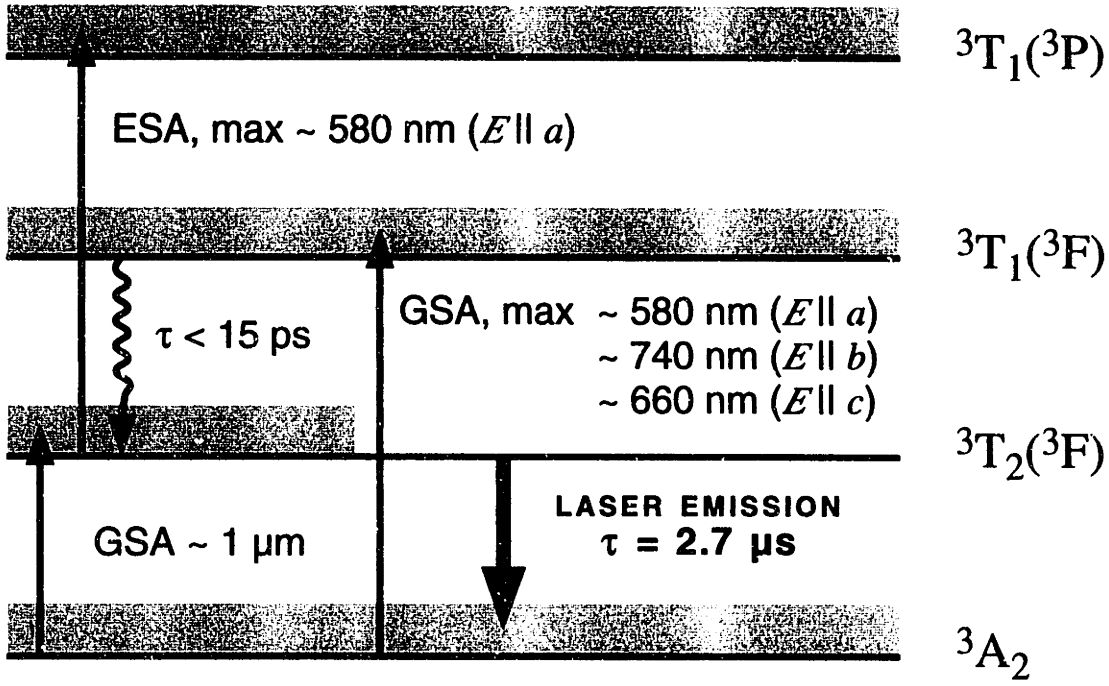

FIGURE 4-2: Energy levels involved in laser operation of near-IR pumped Cr^{4+}:forsterite systems. Optical transitions are indicated by straight lines, and the wavy line indicates a non-radiative relaxation path [73].

will diminish pumping efficiency and such pump orientation should be avoided [73]. Thus in near-IR pumped Cr^{4+}:forsterite crystals the pump polarization should be parallel to either the chromatographic *a*- or *c*-axis.

To measure the fluorescence spectrum with near-IR excitation, a tunable cw Ti:Al_2O_3 laser with the emission wavelength set to 740 nm was used. The Cr^{4+}:forsterite crystal was oriented such that the incident light propagated along the crystallographic *a*-axis (normal to the [100] plane) and with the polarization parallel to the *b*-axis (normal to the [010] plane). The measured fluorescence spectrum shown in Figure 4-3 is virtually identical to the ones obtained when using the 1064 nm pump wavelength.

4.3 CW laser operation

Since the fluorescence spectrum is virtually identical for either, near-infrared and 1064 nm pump wavelengths, and referring to pervious work on lasers operated with crystals at cryogenic temperatures, it seemed promising to pursue work towards the development of a near-IR pumped

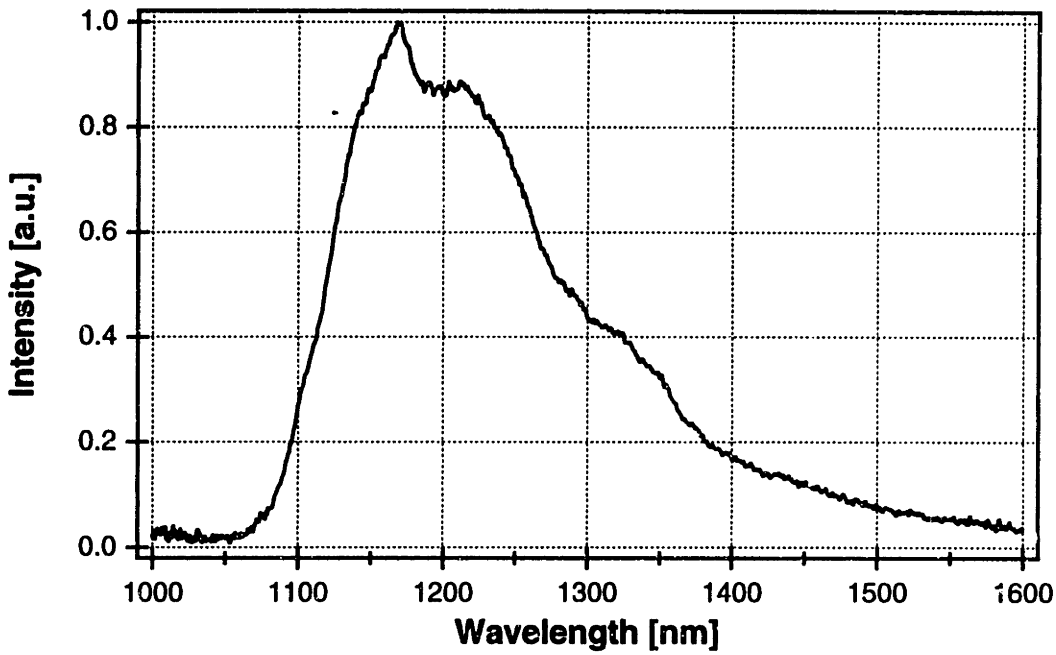

FIGURE 4-3: Fluorescence emission spectrum of a Cr^{4+}:forsterite crystal when pumped along the *a*-axis using a Ti:Al_2O_3 laser with the emission wavelength set to 740 nm and the polarization along the *b*-axis.

room-temperature operated system. Previous studies using near-IR pumping achieved lasing by chopping the pump and operating at low temperatures [40] or by transient pumping [74]. The work on near-IR pumped Cr^{4+}:forsterite at cryogenic (77 K) temperature utilized a 20 mm long crystal commensurate with the absorption length which was required for use with 1064 nm pumping. Due to the larger absorption coefficient in the 740 nm region the entire incident pump power was absorbed in the first few millimeters of the crystal and the remaining length resulted in parasitic absorption at the lasing wavelength and introduced excess loss. The added loss in the crystal was then offset by the increased gain available when the crystal was operated at cryogenic temperatures and laser operation could be attained. Thus, a choice of a pump wavelength in the near-IR, in combination with the use of a short crystal, should yield a Cr^{4+}:forsterite laser operating at room-temperature. This study is of particular interest since it represents an important step to the development of a direct diode-pumped forsterite laser and new compact laser geometries that take advantage of short crystal lengths.

4.3.1 Layout of cw Cr^{4+}:forsterite laser

To demonstrate cw room-temperature lasing a standard symmetric *z*-cavity with arm lengths of 50 cm and two 50 mm radius-of-curvature folding mirrors was used. A 3.0 mm long Brewster-cut Cr^{4+}:forsterite gain crystal of 0.3% at. Cr was mounted in a water-cooled copper heat-sink mount and typically maintained at 10°C. The gain crystal was padded with thin indium foil and compressed (254 μm before compression with a 50% compression ratio) into the water-cooled copper mount to achieve good thermal contact and temperature control. The crystal was oriented for pumping along the crystallographic *a*-axis with the pump polarization incident parallel to the *b*-axis. The pump laser, a *Coherent Mira 900* Ti:Al_2O_3 laser pumped by a *Coherent Innova 200*

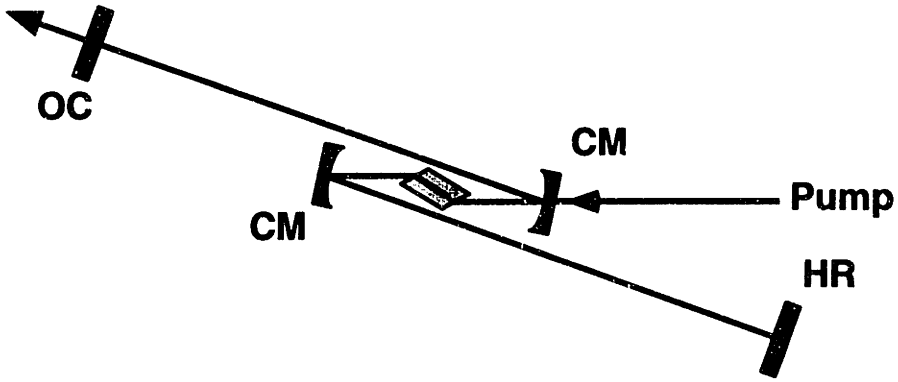

FIGURE 4-4: Symmetric *z*-cavity: OC, output coupler; CM's, 50 mm radius-of-curvature folding mirrors; HR, high reflector. The Cr^{4+}:forsterite crystal was 3.0 mm long, Brewster-cut, water cooled and maintained at 10°C.

argon-ion laser, was optimized for cw operation and continuously tunable from 680 nm to 820 nm wavelength range, with an average output power of up to 2 W. The pump beam was delivered into the crystal using a 60 mm focusing lens. The curved folding mirrors used to characterize near-IR pumping of a Cr^{4+}:forsterite laser were optimized for operation with a 1064 nm pump. Consequently the pump transmission through the curved folding mirrors measured T(740 nm)=51%, thus care had to be taken to record the *true* incident power onto the crystal. The pump beam diameter within the crystal was optimized to match the intracavity waist diameter. The laser cavity was re-optimized at each pump power to exclude any performance artifacts due to thermal lensing in the gain crystal. No measurable thermal lensing was observed with the available pump powers.

4.3.2 Slope efficiency of cw laser operation

To characterize the continuous-wave performance of the near-IR pumped Cr^{4+}:forsterite laser, a systematic study of the laser output for various output couplers was performed. The partial reflectors (output couplers) were available with transmissions measured to as 0.7%, 2.4%, and 4.9%. To expand the set of output couplers it was possible to replace the high reflector (R≥99.9%) with one of the output couplers. Placing output couplers in place of both cavity end-mirrors allowed for measuring the laser performance at three additional, calibrated, output couplings: 0.7%+2.4%=3.1%; 0.7%+4.9%=5.6%; 2.4%+4.9%=7.3%. If the power at both output ports measured simultaneously and plotted against the incident pump power onto the crystal, laser slope efficiencies can be calculated. The pump laser was set to a wavelength of 740 nm corresponding to the peak absorption of Cr^{4+}:forsterite and the pump beam diameter within the crystal was set to match the intracavity waist diameter (about 26 μm in the tangential and 16 μm in the saggital direction).

Cavity configurations with various output couplers ranging from 0.7% to 7.3% were tested. The laser output power increased linearly with increasing incident pump power onto the crystal throughout the tested range. The maximum pump power used was limited by the available output power from the Ti:Al_2O_3 laser. The lowest threshold was obtained for a 0.7% output coupler and was as low as 130 mW at the free-running output wavelength of 1260 nm. Linear polynomial fits were performed to the data in Figure 4-5 so that slope efficiencies and threshold pump powers were extracted for each of the output couplers. The obtained data are shown in Table 4-1. It can be seen that slope efficiencies for a range of output couplers (2-6%) were fairly uniform at ~14.5% and dropped outside this range. When performing a linear polynomial fit to the data in Figure 4-6 and applying the formalism from section 3.2.3 the absorption coefficient at the lasing wavelength (parasitic absorption) was calculated to be $\alpha(1260)=0.0217\ cm^{-1}$. Another quantity which can be extracted form the linear fit in Figure 4-6 is the small signal gain in this system, $\gamma(1260)=0.286\ cm^{-1}$. Using the obtained value for the parasitic absorption and the absorption coefficient at the pump wavelength, $\alpha(740\ nm)=9.92\ cm^{-1}$, the figure of merit for this system is in excess of *FOM*=450. As a result of the use of a pump wavelengths with large absorption coefficients, lasers with large *FOM*'s can be obtained without the need to improve the quality of crystals. If crystals with higher doping densities are implemented, one of the typical problems is the increased para-

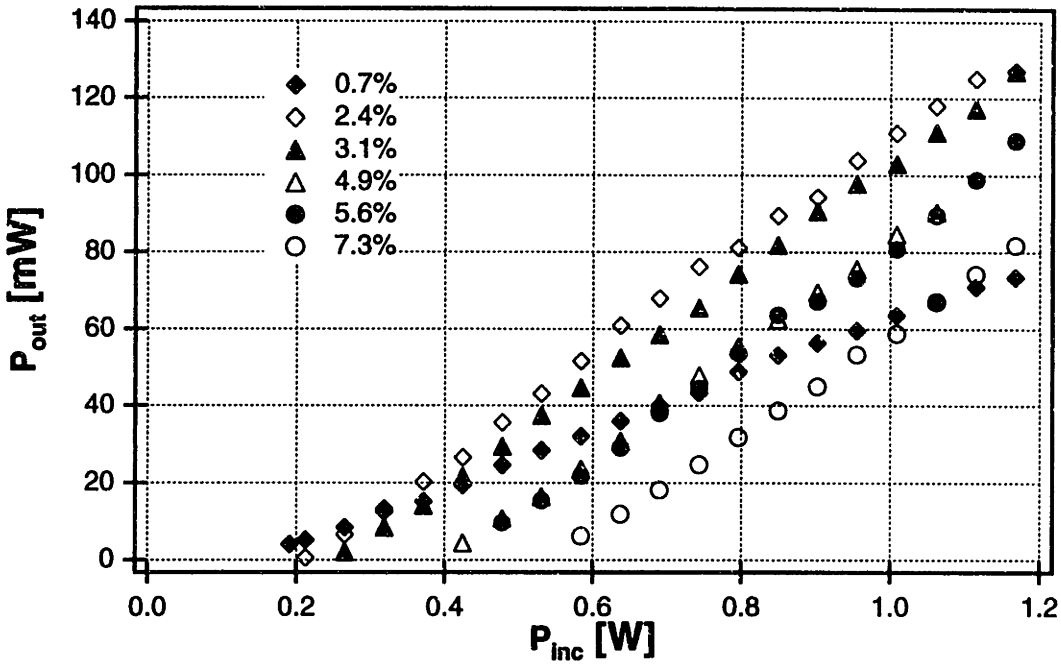

FIGURE 4-5: Cr^{4+}:forsterite laser output as a function of incident 740 nm pump power for various output couplers wit a typical free-running lasing wavelength of 1260nm.

TABLE 4-1: Slope efficiency and absorbed threshold pump power for each of the output couplers used.

Output coupling	Slope efficiency, η_s	Threshold [mW]
0.7%	7.6%	133
2.4%	14.3%	198
3.1%	14.7%	250
4.9%	14.6%	383
5.6%	15.1%	405
7.3%	13.7%	521

sitic absorption. When pump wavelengths with high absorption coefficients are used in conjunction with shorter gain crystals the system performance is not as affected by the increase in parasitic loss.

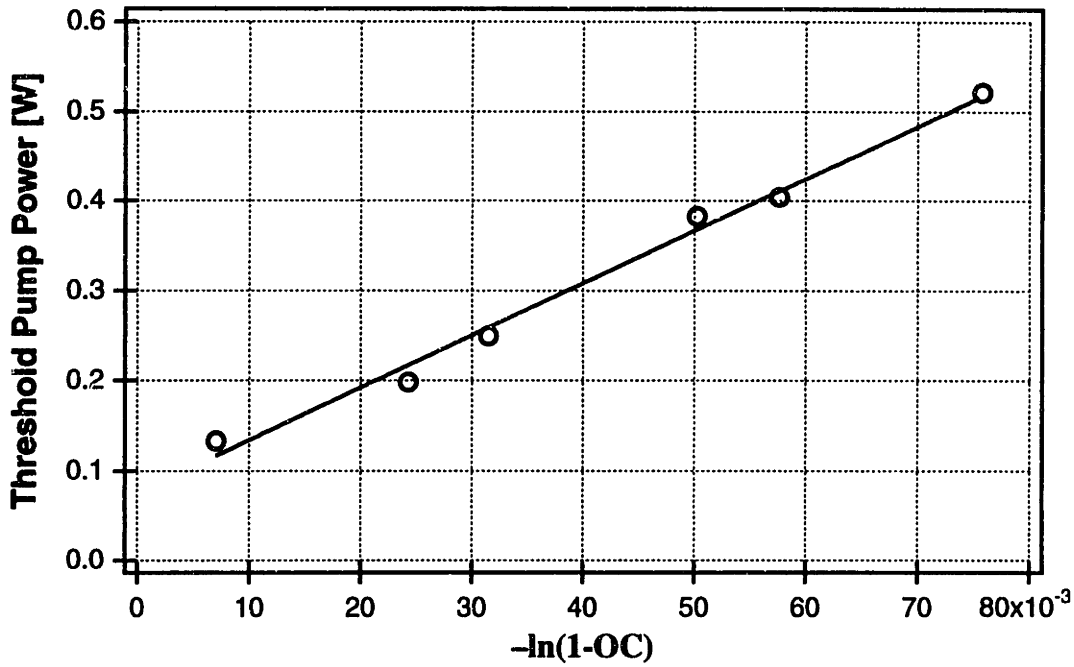

FIGURE 4-6: Threshold absorbed pump power versus the logarithm of the output coupler reflexivity. By performing a linear fit to data the limiting slope efficiency for a near-IR pumped Cr^{4+}:forsterite laser was estimated as 20±4%.

Using the calculated parasitic absorption, α(1260 nm), and the slope efficiency data, η_s, in Table 4-1 the value for the limiting slope efficiency, η_0, can be extracted. Using equation (3-10) the limiting slope efficiency for each output coupler can be calculated, and an average value with the corresponding measurement error can be estimated. Thus, a slope efficiency in the absence of any parasitic absorption (a theoretically perfectly grown Cr^{4+}:forsterite gain crystal) was estimated as η_0=20±4%. An alternate approach to determining the limiting slope efficiency is to use equation 3.B and perform a linear fit to the data in Figure 4-7. The limiting slope efficiency using this method was estimated as η_0=19±4%. Even though the two approaches yield comparable values the latter one may, for this data set, be subject to a larger systematic error. In this measurement there is a cluster of data points for larger output couplings which in effect weights one end of the linear curve fit. This data cluster in turn has more significance in determining the abscissa intercept and may result in a systematic error to the limiting slope efficiency. When applying this analysis it is desirable to use a set of output couplers which result in a more equal data point spacing of inverse output coupling values. Output couplers of intermediate reflectivities where unavailable for this experiment.

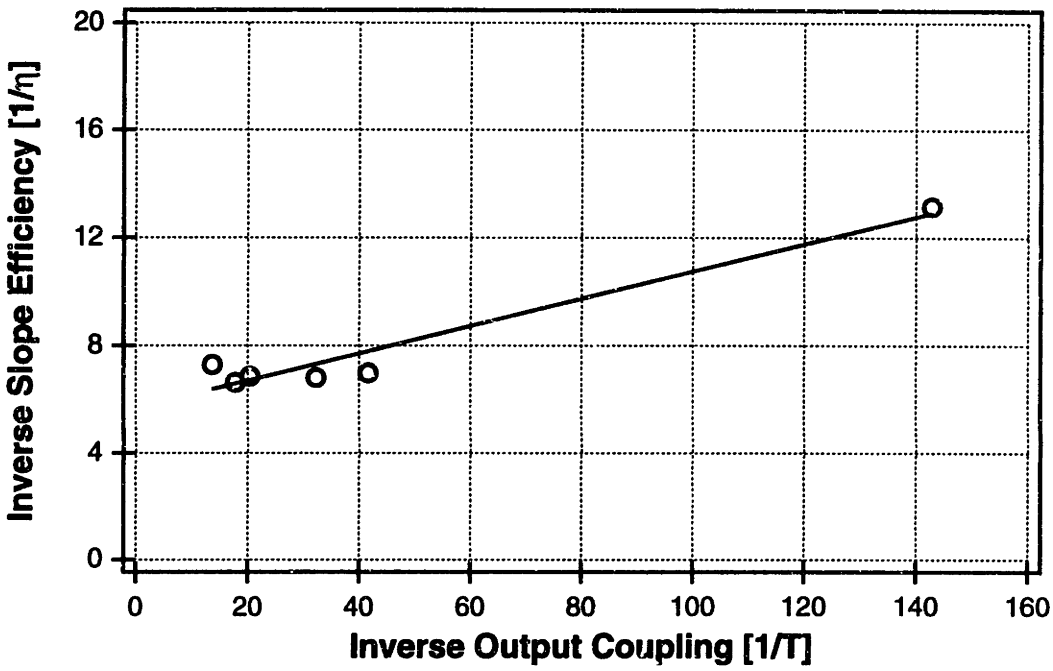

FIGURE 4-7: Inverse slope efficiency plotted versus inverse output coupling. Using the 740 nm pumped C4+:forsterite laser a limiting slope efficiency of 19±4% was estimated

The estimated limiting slope efficiency of η_0=20±4% is considerably lower than both, the limiting slope efficiency reported by Carrig and Pollock [40], η_0=35±9%, and the theoretical quantum defect limit of 59% (ratio of pump and lasing wavelengths, λ_P/λ_L). One of the differences in the way the two values were obtained is that Carrig and Pollock performed their experiments with a Cr^{4+}:forsterite gain crystal cooled to 77 K. Their work indicated a considerable drop in gain with increasing temperature and this may account for the decrease in limiting slope efficiency. However, when comparing the limiting slope efficiency measured for a room-temperature operated 1064 nm pumped system (see section 3.2.3), η_0(1064 nm)=30±3%, with the value when using a 740 nm pump, η_0(740 nm)=20±4%, one can see that the ratio is commensurate with the different quantum defect ratio for the two pump wavelengths.

4.3.3 CW tuning range

One of the important specifications of laser systems is the attainable output wavelength spectrum. Solid-state lasers with vibronically broadened energy levels typically allow for the making of cw lasers with broad tuning ranges. Continuous wave Cr^{4+}:forsterite systems operated

at cryogenic temperatures and pumped at 1064 nm have been demonstrated with a tuning range 1200 to 1320 nm [44]. To evaluate the cw tuning performance of this laser a Shott Glass SF6 prism was inserted into the cavity so that continuous laser tuning could be achieved by tilting the high-reflector end mirror. The gain crystal was 3.0 mm long, Brewster-cut and was maintained at

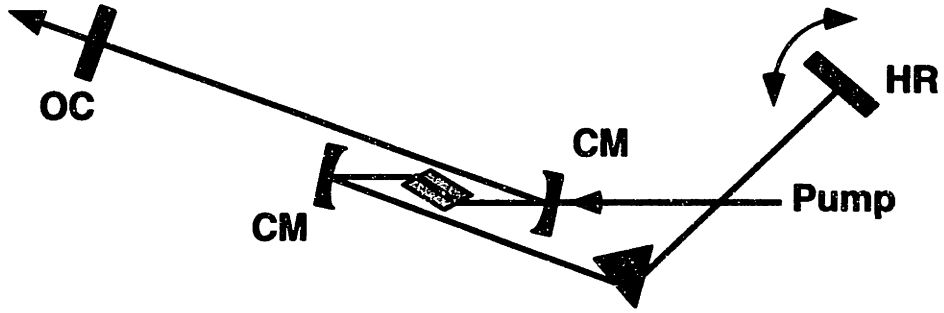

FIGURE 4-8: Standard z-cavity with dispersive prism for wavelength tuning: OC, output coupler; CM's, 50 mm radius-of-curvature folding mirrors; HR, high reflector. The Cr^{4+}:forsterite crystal was 3.0 mm long, Brewster-cut, water cooled and maintained at 10°C. Wavelength tuning is achieved by tilting the high reflector.

a temperature of 10° C. The pump laser was set to a wavelength of 740 nm and the incident power onto the crystal was 1.2 W (1.1 W absorbed). When pumped at 740 nm, and using a 0.7% output coupler, the laser was continuously tunable from 1175 to 1375 nm. This 200 nm tuning range is to our knowledge the largest cw tuning range reported to date for a Cr^{4+}:forsterite laser. The tuning range was somewhat smaller when higher output couplings were used. In general the tuning range is limited by a combination of various factors including the reflectivity bandwidth of the optical components at short wavelengths, and decreasing gain on the long wavelength side.

4.3.4 Pump wavelength selection

Initial work with Cr^{4+}:forsterite lasers was based on systems which were implemented using 1064 nm wavelength pump lasers. This was a convenient choice of wavelengths due to the overlap with a local maximum in the absorption spectrum with Cr^{4+}:forsterite and availability of Nd:YAG pump lasers with 1064 nm emission. However, in general it is desirable to develop lasers which can be directly pumped by means of semiconductor diode lasers. These devices typically have rel-

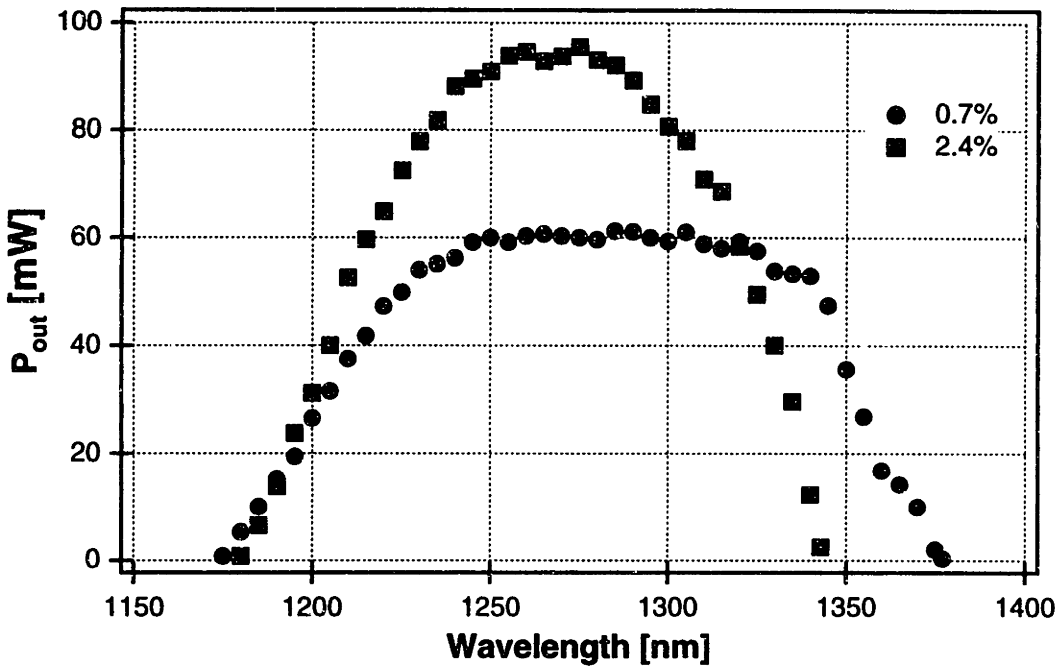

FIGURE 4-9: Continuous wave tuning range obtained for two different output couplers when the lasers was pumped at 740 nm. A tuning range of 200 nm, 1175-1375 nm, was obtained for a 0.7% output coupler.

atively large wavelength fabrication tolerances, and if exact wavelengths are needed these typically result in low fabrication yields. The work presented in this section quantifies how the choice of near-IR pump wavelengths affects the performance of a Cr^{4+}:forsterite laser.

The Cr^{4+}:forsterite laser cavity shown in Figure 4-4 was operated with a number of pump wavelengths ranging from 690-820 nm. Pump wavelengths were accessed by a tunable cw Ti:Al_2O_3 but can also be generated by GaAsInP or AlGaAs semiconductor laser diodes making direct diode pumping possible. The laser layout used for this set of experiments is identical to the one shown in Figure 4-4 using a 0.7% output coupler. The output powers as a function of incident pump powers onto the laser crystal are shown in Figure 4-10. The highest slope efficiency was attained for pumping at 740 nm where about 95% of the incident pump power was absorbed. However, if the pump wavelength is tuned away from the design wavelength of 740 nm to either 710 nm or 760 nm, the slope efficiency remains virtually unchanged. When the pump wavelength was tuned to even longer wavelengths, another region of slowly changing slope efficiencies was found around 780-820 nm. Although absorption is rapidly changing in the 710-760 nm range, the

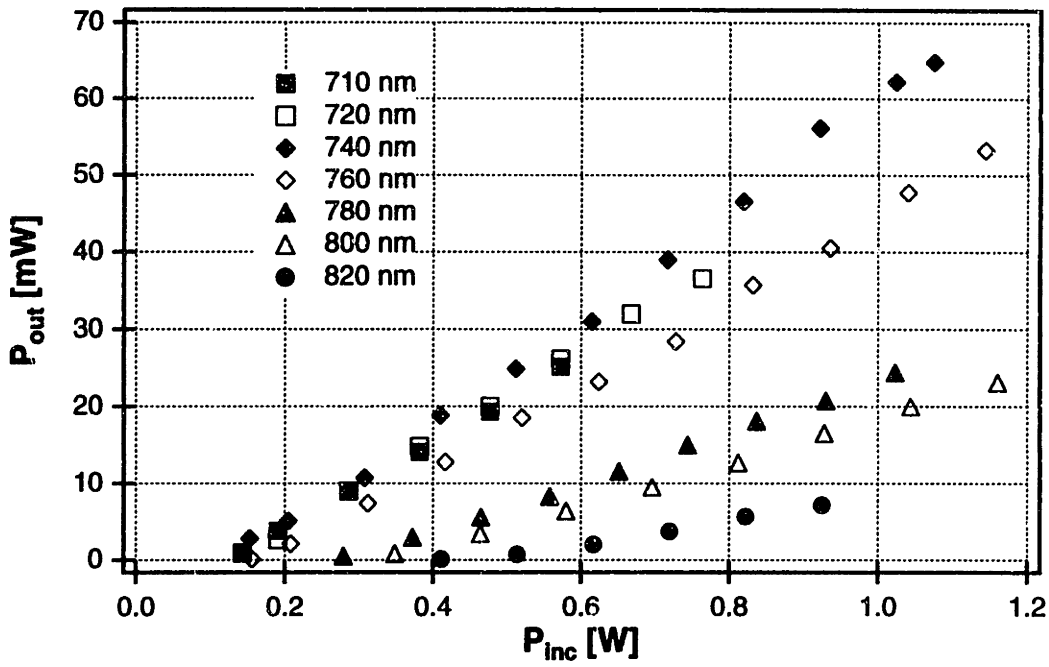

FIGURE 4-10: Cr^{4+}:forsterite laser output performance as a function of incident pump power onto the crystal for different pump wavelengths with a 0.7% output coupler.

majority of the pump (70-95%) is absorbed in the 3 mm crystal length, making the laser operation relatively insensitive to exact pump wavelengths in this region. Due to smaller absorption coefficients in the 780-820 nm range, the pump power is not absorbed as strongly in the 3.0 mm crystal (39-53%), resulting in a smaller overall slope efficiency. However, due to the slowly varying absorption coefficient in this region the slope efficiency is comparable for all pump wavelengths in this range. This insensitivity to exact pump wavelengths makes this system suitable for pumping with sources which have relatively large wavelength selection tolerances.

The laser output powers shown in Figure 4-10 are displayed as a function of the pump power incident onto the crystal. However, since the crystal length is fixed, and the absorption length varies for different wavelengths, the actual absorbed power in the crystal is not the same for a given incident power. Consequently the slope efficiency does not reflect the best laser performance at a given pump wavelength. When the power incident onto the crystal is converted to the actual absorbed power one can obtain a better measure of what the actual laser performance would be for given design wavelength. Typically when a laser system is designed, the gain medium length is

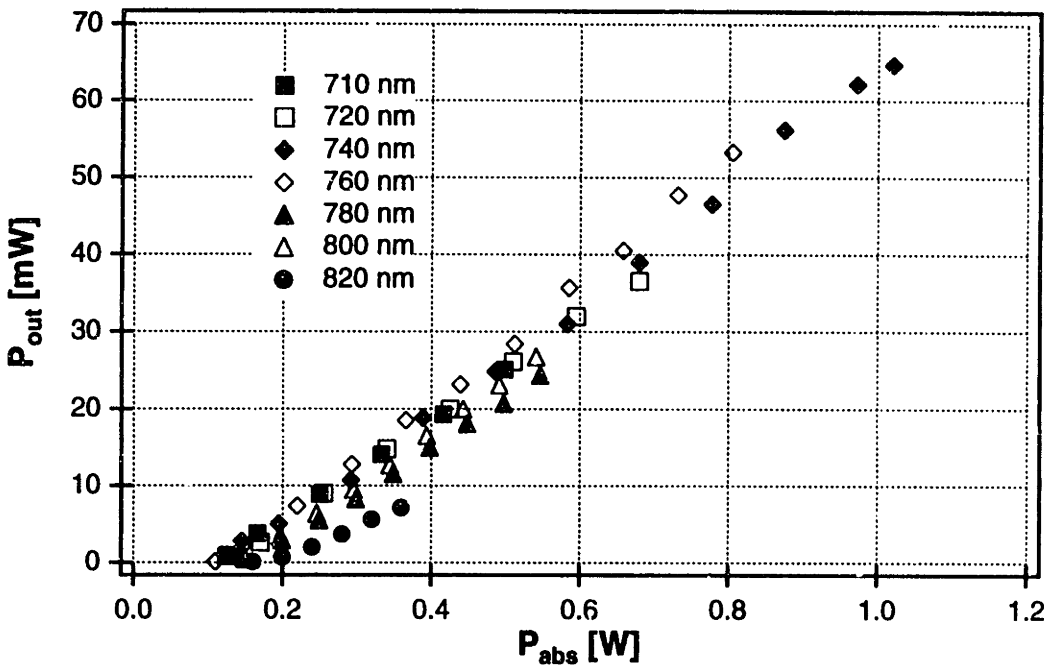

FIGURE 4-11: Cr^{4+}:forsterite laser output performance as a function of absorbed pump power in the crystal for different pump wavelengths with a 0.7% output coupler.

chosen such that the about 85% of the incident pump power is absorbed. The data in Figure 4-11 shows that the slope efficiencies for all wavelengths in the 710-800 nm are comparable. Thus, by properly scaling the crystal length a Cr^{4+}:forsterite laser can perform equally well for a range of near-IR pump wavelengths. The crystal length can be scaled up to the point where parasitic residual absorption at the emission wavelength significantly reduces the figure of merit.

It should be pointed out that part of the efforts of this work is directed to developing a direct diode pumped version of a Cr^{4+}:forsterite laser. One of the aspects of this effort is the development of a system which can be pumped by broad-area, non-diffraction limited, semiconductor laser diodes. Systems utilizing such devices require that the gain media have a short absorption length and use pump lasers with emission wavelengths as close as possible to the in the 740 nm absorption peak. Additional issues associated with direct diode pumping of solid-state lasers are addressed in section 4.6.

4.4 Compact cavity implementation

To further investigate the possibility of developing a compact forsterite laser a Cr^{4+}:forsterite laser for which the z-cavity had arm lengths as short as 10 cm was implemented. The Cr^{4+}:forsterite gain crystal was 3.0×3.0×3.0 mm^3 in size, Brewster-cut, padded with thin indium foil and compressed (254 μm before compression with a 50% compression ratio) into a copper mount to achieve good thermal contact. A pair of 50 mm radius-of-curvature folding mirrors, a flat high reflector and a flat output coupler were used to form the laser resonator. For this laser the pump beam diameter in the crystal was not modified from that optimized for the longer cavity discussed in section 4.3.1. This configuration performed with identical output powers as the cavity design that had arms lengths of 50 cm. One of the constraints in implementing compact laser systems is the need for external water cooling for the gain crystals. Heat extraction from the gain medium is essential since temperature increases typically result in gain reduction for Cr^{4+}:forsterite [44]. To demonstrate cw laser operation without water cooling the compact cavity laser was operated at room temperature (~20°C) by mounting the crystal in a copper heat sink and ambient air cooling only. Stable cw operation was achieved with only modest, <10%, decrease in output power. These observations are of particular interest since the thermal conductivity of forsterite is only 5 W/(m·K) [39][75][76] which is considerably less than for other solid-state materials such as YAG, 13 W/(m·K), or sapphire, 34 W/(m·K) [77]. The additional heat-load is sufficiently small that the excess heat can be extracted to the copper mount without suffering a significant gain reduction. In actual system implementation miniature thermo-electric cooler units could be added to facilitate additional heat extraction to an air cooled mount. Since the thermal conductivity of forsterite is small it is important to achieve a good crystal-indium-copper mount contact for good crystal cooling. Moreover, it is beneficial to keep the crystal dimensions as small as possible to reduce heat transfer problems in forsterite.

A photograph of the compact Cr^{4+}:forsterite resonator is shown in Figure 4-12; the pump laser for the proof-of-concept layout was a tunable cw Ti:Al_2O_3 laser.

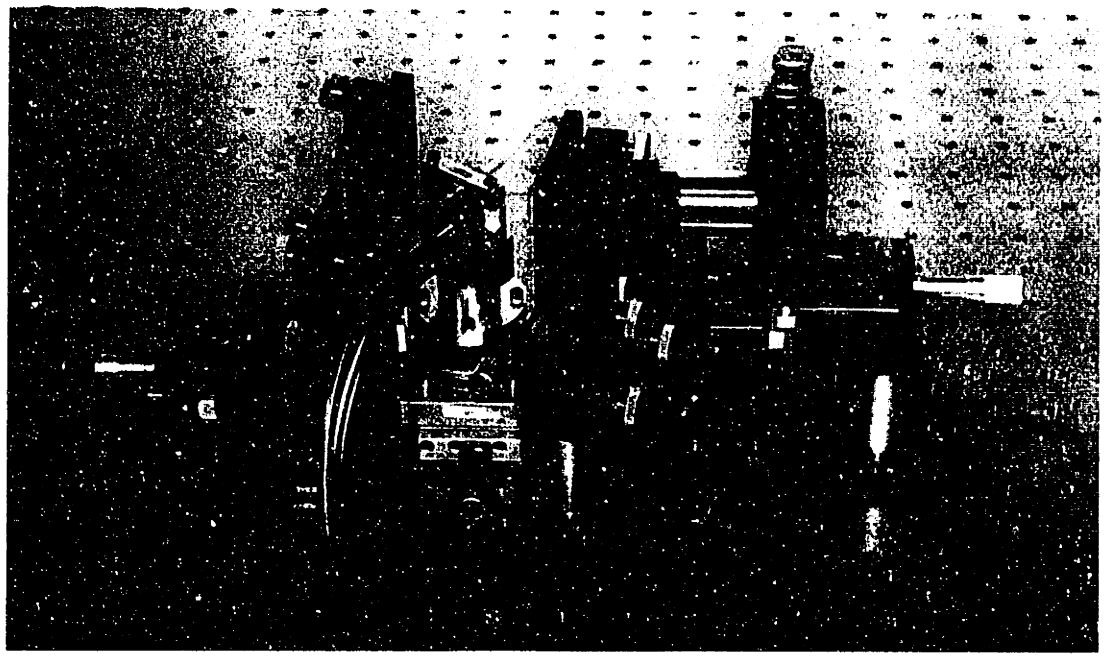

FIGURE 4-12: Compact Cr^{4+}:forsterite laser using a standard symmetric z cavity.

4.5 Modelocked near-IR pumped Cr^{4+}:Forsterite laser

Previous work on Cr^{4+}:forsterite lasers demonstrated short pulse operation using active modelocking (31 ps) [53], regenerative self-modelocking (48 fs) [54][56], additive-pulse modelocking (150 ps) [55], Kerr-lens modelocking (25 fs) [58][59] and modelocking using a semiconductor saturable Bragg reflector [60][61]. The shortest pulses to-date from a Cr^{4+}:forsterite laser were 25 fs in duration, obtained using a 5% output coupling, with 7 W of pump power resulting in 300 mW of output power [59]. All work to date on short pulse generation in Cr^{4+}:forsterite lasers was based on systems using 1064 nm laser pump sources. Due to the absorption coefficient at 1064 nm ($\alpha<2$ cm^{-1}) crystal lengths longer than 10 mm are required for viable laser operation and most published work listed above utilized crystal lengths of about 20 mm. For short femtosecond pulse generation, the use of short crystals potentially provide better performance by reducing effects of higher-order dispersion [52]. Thus, near-IR pumping opens the possibility for the generation of shorter femtosecond pulses than published results obtained from 1064 nm pumped Cr^{4+}:forsterite lasers.

Work on Kerr-lens mode-locked operation was conducted using a standard *z*-cavity with a pair of dispersion compensating prisms placed inside the cavity (see Figure 4-13). Two 50 mm radius-of-curvature folding mirrors, a flat high reflector and a flat output coupler were utilized. The gain crystal was 3.0 mm long, Brewster-cut and was maintained at a temperature of 10° C. The cavity geometry was chosen for aberration free operation and the angle of incidence onto the curved folding mirrors was adjusted such that the overall astigmatism and coma of the cavity were zero. The cavity arm lengths were set to 50 and 60 cm, and a pair of Shott Glass SF6 prisms with a 21 cm separation was placed in the longer arm. Shott Glass SF6 prisms were used by Yanovsky *et al.* [59] to obtain the shortest to-date, 25 fs, pulses from a Cr^{4+}:forsterite laser were also a well suited choice for this implementation. The curved folding mirrors and the flat high reflector had a reflectivity $R>99.99\%$ for the range 1150-1370 range. The output coupler had a reflectivity $99.5\%<R<99.3\%$ for the range 1200-1360, with a 0.125" thick fused silica substrate.

The pulse duration was measured using a colinear interferometric intensity autocorrelator based on a 0.3 mm $LiIO_3$ (lithium iodate) crystal for Type I second harmonic generation (SHG) at a phase matching angle of 24.27°. The phase matching bandwidth of the $LiIO_3$ crystal was well in

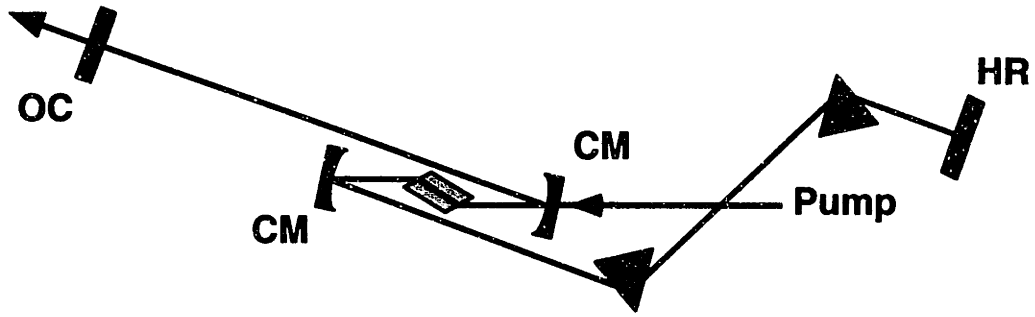

FIGURE 4-13: Schematic diagram of a standard z-cavity laser resonator: OC, output coupler; CM's, 5 cm radius-of-curvature folding mirrors; HR, high reflector. A pair of SF6 prisms was used for dispersion compensation. The crystal was pumped by a Ti:Al_2O_3 laser tuned to 740 nm.

excess of the mode-locked pulse spectrum (see Figure 4-14). The autocorrelator was balanced

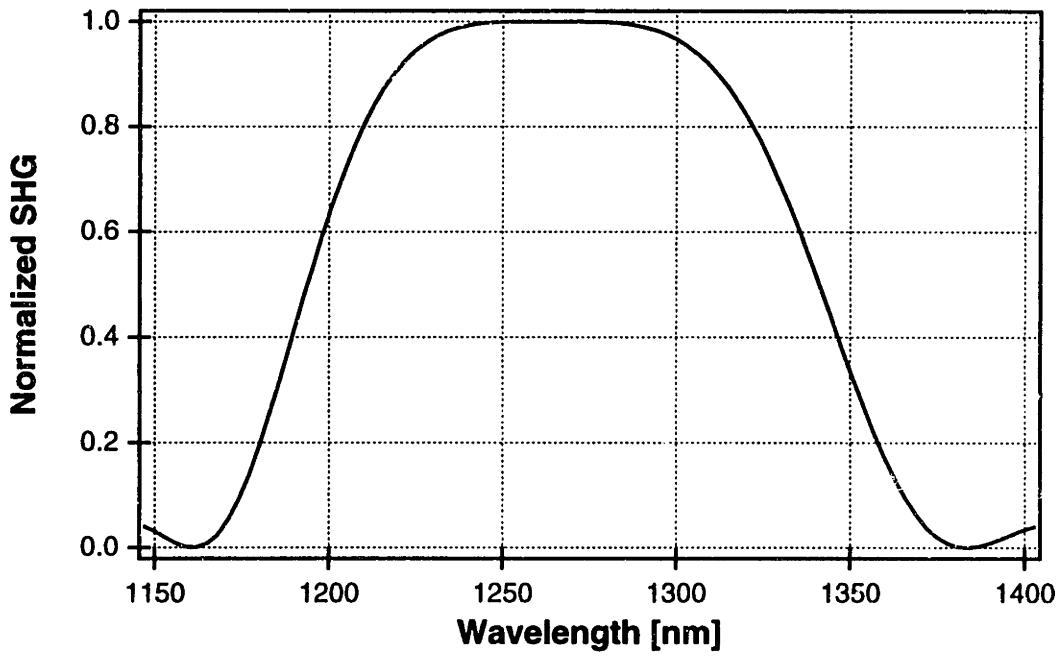

FIGURE 4-14: Wavelength dependence of second-harmonic (SHG) intensity for a 0.3 mm thick $LiIO_3$ crystal at a phase matching angle of 24.27°.

such that a matching fused silica substrate was placed in one interferometer arm to compensate for any dispersion introduced by the 50-50 beam-splitter substrate. Both interferometer end-mirrors were metallic gold coated glass substrates, and focusing into the $LiIO_3$ crystal was done by a gold coated off-axis parabolic reflector. A *General Scanning* linear galvanometric actuator was

used to sweep one of the interferometer arms and induce the necessary time delay to record the pulse autocorrelation. A digital oscilloscope was used for data acquisition and data transfer to a computer.

The near-IR pumped Kerr-lens mode-locked Cr^{4+}:forsterite laser generated pulses of 52 fs in duration at a repetition rate of 140 MHz. The corresponding spectrum was measured to have a 34 nm FWHM bandwidth. The pulse intensity autocorrelation and the corresponding pulse spectrum are shown in Figure 4-15. The peak-to-background ratio is close to the theoretical value of eight confirming good fringe contrast. The time-bandwidth product for this laser is 0.325. Assuming a $sech^2$ output intensity pulse shape the theoretical time-bandwidth product is

$$\Delta\nu\Delta t = 0.315 \tag{4-2}$$

which indicates that the output pulses are transform limited within the experimental uncertainty. Since the pulses were not dispersion compensated before autocorrelation, and any residual chirp is probably the result of dispersion in the output coupler. Modelocking was induced by mechanical perturbation of the cavity, typically by displacing one of the prisms. Long-term stable modelocked operation (hours) was achieved by enclosing the laser in an acrylic cabinet to reduce air currents. Typical output power for the mode-locked laser was ~20 mW when pumped at 740 nm with ~1 W incident power onto the crystal. The modelocking threshold was ~0.8 W of incident pump power.

The near-IR pumping of a KLM Cr^{4+}:forsterite laser is beneficial for femtosecond pulse generation. Short gain crystals lengths are important in optimizing short-pulse operation of femtosecond KLM lasers to reduce contributions of higher-order dispersion, and can limit pulse duration [52]. The pulse durations obtained here are believed to be limited by the low pump power and limited self-phase modulation in the gain medium. The shortest pulse to-date from a mode-locked Cr^{4+}:forsterite laser is 25 fs [59] and it is anticipated when higher pump powers become available a near-IR pumped KLM Cr^{4+}:forsterite laser can match and perhaps reduce the pulse when compared to 1064 nm pumped systems.

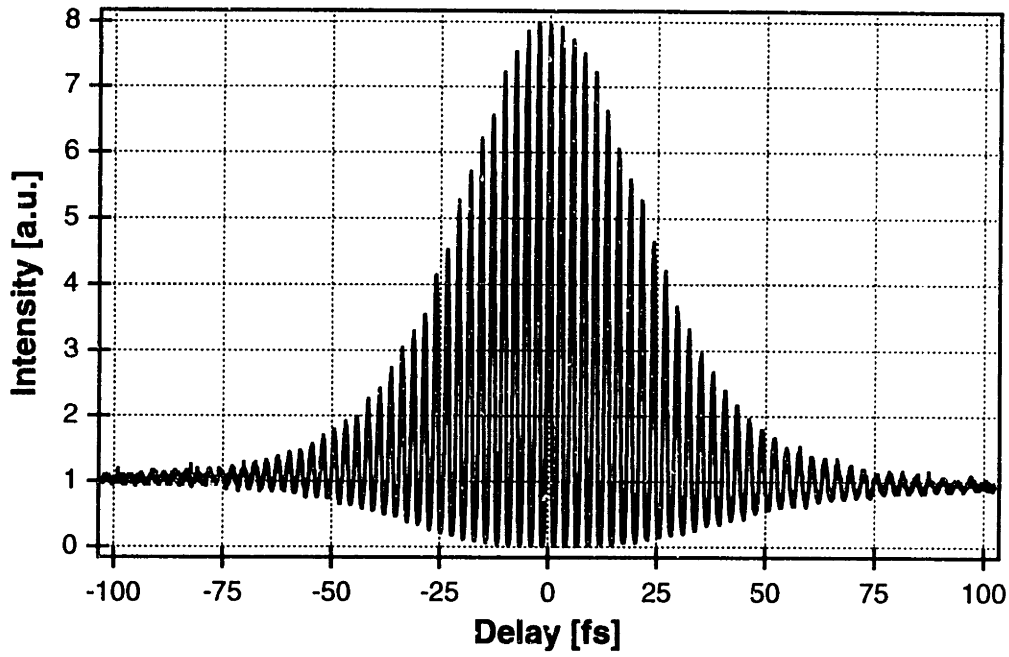

(a)

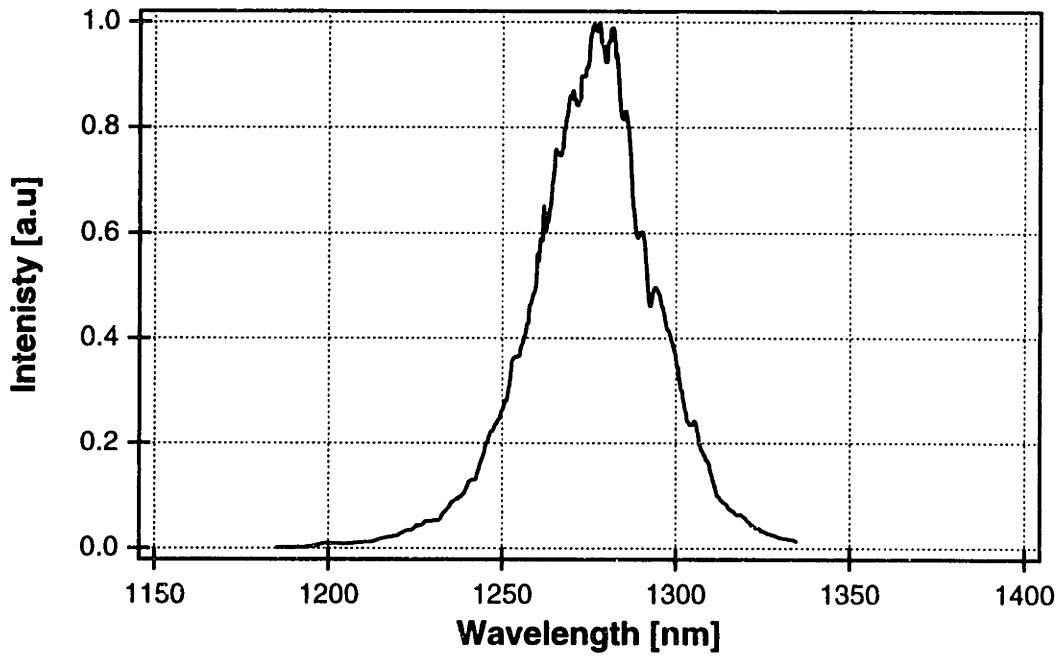

(b)

FIGURE 4-15: Measured spectrum (a) and interferometric autocorrelation trace (b) of a mode-locked near-IR pumped Cr^{4+}:forsterite laser using a 3 mm gain crystal and a pair of SF6 dispersion compensating prisms.

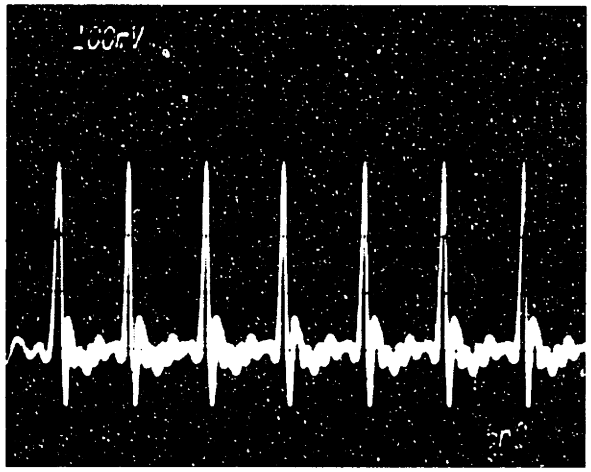

FIGURE 4-16: Oscilloscope trace of a pulse train at 140 MHz generated by a mode-locked Cr^{4+}:forsterite laser pumped at 740 nm.

4.6 Diode pumping considerations

The design and optimization of direct semiconductor pumping is an important step to widespread commercialization of tunable broad-band and ultrafast solid-state lasers. The work in previous sections demonstrates the feasibility of pumping in the near-IR wavelength region, 680-820 nm, of Cr^{4+}:forsterite lasers. This wavelength region is accessible by semiconductor pump sources and a number of such devices are readily available from commercial sources. This section will present issues which must be addressed for designing and implementing a direct diode-pumped Cr^{4+}:forsterite laser.

Currently there are a variety of commercial laser diodes available, ranging from single-mode TEM_{00} devices, to diffraction limited high power semiconductor sources, to broad-area multimode (high power) diodes. Single-mode devices are waveguide devices operating in the lowest guided mode, TEM_{00}. These devices have a diffraction limited spatial output beam but are generally restricted to low output powers and are not suitable for diode pumping of solid-state lasers. Another class of devices are high power, diffraction limited semiconductor sources based on tapered semiconductor laser/amplifier technology. Tapered semiconductor devices can generate diffraction limited output beams with output powers commensurate with those necessary for direct diode pumping of solid-state lasers. However, the fabrication and implementation of these devices is rather complex and results in high per-unit cost. Though tapered devices are very attrac-

tive from a technological point of view, at this time, their limited availability and high cost do not make them viable pump sources for solid-state lasers. At this time the most attractive choice for direct-diode pumping of solid-state laser are broad-area multi-mode semiconductor laser diodes. These devices are available at various wavelengths and with output powers which are suitable for direct diode pumping of solid-state lasers.

4.6.1 Broad-area semiconductor laser diodes

To achieve optimal efficiency in pumping laser gain media it is necessary to achieve good spatial overlap between the resonator mode and the pump beam. For the case where the pump laser beam is diffraction limited (gaussian) and using the appropriate imaging system it is possible to obtain a full overlap with the intracavity resonator mode. Thus, when using diffraction limited semiconductor pump sources, the results obtained with the tunable cw $Ti:Al_2O_3$ pump laser can be directly applied to the implementation of such diode pumped systems. However, when using non-diffraction limited pump sources, other imaging constraints have to be taken into account and it is in general not possible to achieve a perfect overlap of the resonator mode and pump beam. In general there will be reduction in pump power delivered to the resonator gain region and pump sources with larger nominal output powers will be required than if diffraction limited sources were used.

One of the difficulties in using broad-area laser diodes is due to the difference in emission patterns of the two axes of the device. The emission pattern in the direction perpendicular to the junction is nearly diffraction limited, whereas in the direction defined as parallel to the diode junction the emission is one of a broad area, multi-mode, source. These devices are single mode slab waveguides formed by the epilayers (y-direction), and 50-200 μm wide multimode waveguides in the plane parallel to the epilayers (x-direction). The two different beam propagation directions also have virtual sources at different points resulting in an astigmatic output radiation pattern. Devices of this kind can be implemented with output powers as high as several watts (depending on the emission wavelength) and in general increases in power are attained by increasing the width of the multimode waveguide.

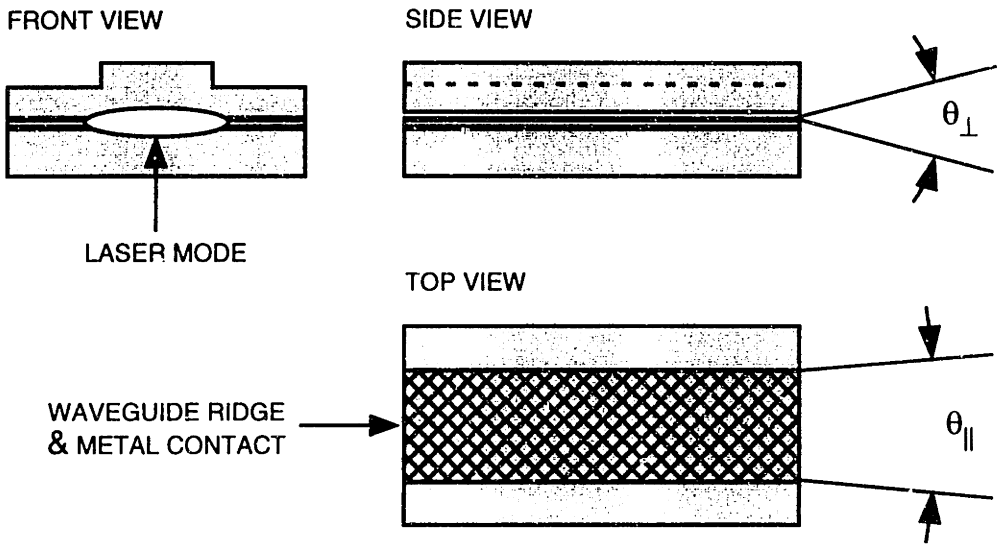

FIGURE 4-17: Schematic of a broad-area semiconductor laser diode. The emission pattern can be separated into two directions: perpendicular to the diode junction, and parallel to the junction.

4.6.2 Pump emission mode control

For efficient optical pumping of lasers it is important to attain a good overlap between the resonator mode inside the gain medium and the emission mode of the pump laser. However, when using non-diffraction limited laser diodes particular care has to be taken to achieve efficient power delivery into the resonator mode [78][15]. The pump-diode emission perpendicular to the junction is diffraction limited and with proper imaging a perfect overlap between the pump beam and resonator mode can be attained. The beam profile parallel to the junction however, is many times diffraction limited and is in practice the limiting factor to an optimal overlap between the resonator mode and pump beam.

For non-diffraction limited beams the quantity which has to be conserved at all times is the *brightness* of the optical source. This quantity is defined as the product between the beam waist (radius) w_0, the far-field half-angle θ and the index of refraction of the medium n

$$w_0 \theta n = C \geq \frac{\lambda}{\pi} \tag{4-3}$$

where C is a constant that is characteristic of the beam quality; as the spot size at the focus decreases, its corresponding far-field angle increases.The ratio C to λ/π, where λ is the beam wavelength, gives the beam quality in the number of times diffraction limited.

Using the brightness theorem one can calculate the smallest spot waist w_{xc} to which a broad area-diode can be mode matched for a gain crystal of a given length L [78]. In general, the resonator mode within the gain crystal can be approximated by a cylinder of length L into which the pump beam is focused using geometrical imaging. The magnification factor for the imaging system is selected such that the pump beam size at the crystal face is minimized with respect to the waist within the crystal. Thus, using the brightness theorem and assuming a linear diode beam expansion inside the crystal, the waist at the face can be written as

$$w_p\left(\frac{L}{2}\right) = w_{p0} + \frac{\theta_{xp}L}{2} = w_{p0} + \frac{L}{2}\frac{w_{xd}\theta_{xd}}{w_{p0}n_f}, \tag{4-4}$$

where θ_{xp} is the diffraction angle within the crystal of index of refraction n_f and w_{xd} and θ_{xd} are the diode waist and diffraction angle respectively. By minimizing equation (4-4) the smallest waist inside the crystal can be obtained such that

$$\frac{d}{dw_{p0}}\left[w_p\left(\frac{L}{2}\right)\right] = 0 \Rightarrow w_{p0}^{(min)} = w_{xc} = \sqrt{\frac{Lw_{xd}\theta_{xd}}{2n_f}}. \tag{4-5}$$

Focusing to a smaller spot increases the divergence angle and overfills the cylinder at either end. If the beam is focused to a larger spot the divergence angle will be smaller and the pump will fill a larger cylinder corresponding to a larger intracavity mode. Thus, under optimal conditions the laser resonator mode should be matched to the diode beam size at the crystal face such that:

$$w_{xf} = \sqrt{2\frac{Lw_{xd}\theta_{xd}}{n_f}}. \tag{4-6}$$

In laser design the gain medium length is typically on the order of the absorption length. Thus, from equation (4-6) it follows that if long gain crystals are used to achieve a good overlap between the resonator and pump-diode mode it is necessary to resort to a large intracavity waist

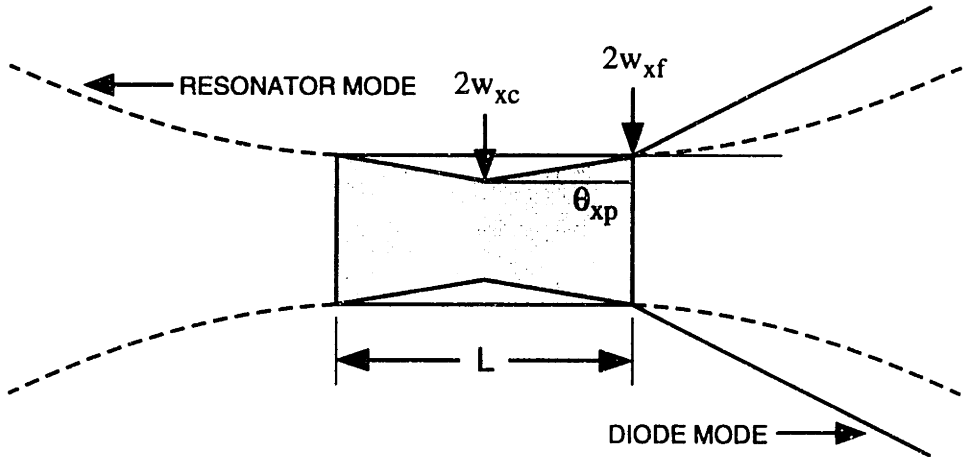

FIGURE 4-18: Overlap between a gaussian resonator mode and broad-area diode laser mode in a gain crystal of length *L*.

size. However, larger intracavity modes, in general, result in larger threshold pump powers and are not a desirable option for low gain systems. This is the reason why most direct diode-pumped lasers have large absorption coefficients which allow for the use of short gain media. However, some exceptions occur in the cases where thermal gain quenching is of concern where it actually may be necessary to consider larger intracavity modes in order to off-set a potential gain reduction due to crystal temperature increase [15].

Typical broad-area diode pumping systems consist of a collimating lens at the diode, a pump focusing lens to focus the beam into the gain crystal and a beam expanding optics assembly. The collimating optic is in general a high numerical aperture (NA) lens used to collimate the diode output beam. In such a system the collimating lens and the focusing lens are used to shape both the diffraction limited (orthogonal, *y*-direction), as well as the non-diffraction limited beam (parallel, *x*-direction). The beam expanding optics are used to expand the beam in the parallel direction only. Beam expansion can be achieved by using a pair of cylindrical lenses for which the ratio of focal lengths determines the telescope magnification factor. Beam expansion can also be achieved by the use of a pair of anamorphic prisms. Anamorphic prisms (see Figure 4-20) can be used for obtaining a wide range of magnifications by changing the prism angles with respect to the incident ray. The expanded output beam is parallel to the input but displaced. Magnification

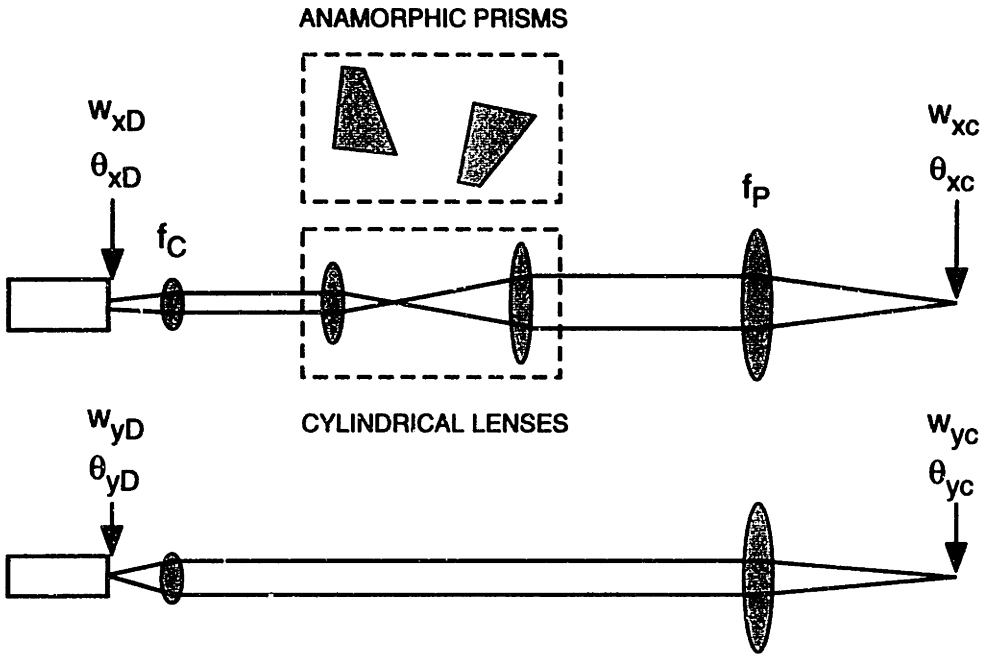

FIGURE 4-19: Separate beam shaping for the perpendicular, *x*-direction, and parallel, *y*-direction, of the broad-area pump diode emission profile. Beam expansion can be attained by using a cylindrical telescope or a pair of anamorphic prisms.

factors are limited at the input/output by the prism size. Even though there is no functional difference between anamorphic prisms and cylindrical telescopes the prisms are preferred since they require less physical space and are not subject to aberrations associated with cylindrical optics.

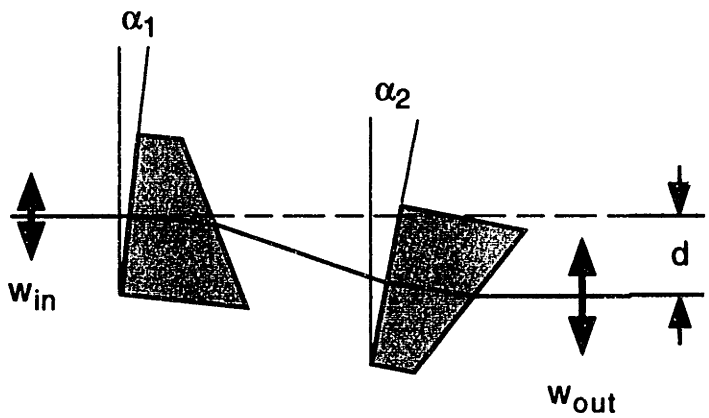

FIGURE 4-20: A pair of anamorphic prisms used for beam expansion. The prism angles, α_1 and α_2, with respect to the incident ray determine the magnification factor. The output beam is expanded and displaced by a distance *d* but parallel to the input beam.

The beam expansion factor, B/X, is a function of the diode collimating lens f_C, the focusing lens f_P, and the waist size w_{xc} calculated in equation (4-5). Thus, for optimal diode coupling of the x-direction diode emission profile into a crystal of length L and index of refraction n_f, the required beam expansion factor is given as

$$B/X = \frac{f_P}{f_C} \cdot \frac{w_{xd}}{w_{xC}} \cdot n_f . \tag{4-7}$$

In a typical set-up with f_C=8 mm, f_P=80 mm, w_{xd}=50 μm, θ_{xd}=2.4°, L=3 mm, and n_f=1.64, the waist size using equation (4-5) is calculated to be w_{xc}=44 μm and the required beam expansion factor is B/X=19. The beam shaping for the x-direction is coupled to the beam shaping of the y-direction (diffraction limited component) by means of the collimating and focusing lenses. Thus, for the above choice of optics and a diode with w_{yd}=1 μm and θ_{yd}=18° the pump beam in the crystal would be w_{yc}=16 μm. It should be pointed out that the example presented here shows a number of problems for actual system implementation. Beam expansion factors B/X=19 are in general difficult to implement and may require large optics for beam propagation. The fact that both diode beam axes are coupled may also result in sub-optimal coupling of one of the beam axes into the resonator mode. In theory a beam shaping assembly can be designed to achieve the best possible overlap between the resonator mode and pump beam. However, in practice the choice of optics is an optimization between the mode overlap and the complexity of a pump-diode beam imaging system. The modeling presented is rather simple for actual diode-pumping cases, but gives a good starting point to the experimental optimization of an actual diode-pumped system.

An alternate approach to beam shaping discussed above is to use very short focal length, several hundreds of microns, cylindrical micro-lens close to the diode facet [15]. The cylindrical micro-lens can be used to collect the fast diverging, y-direction, and a spherical lens can collimate both axes simultaneously. In this arrangement all necessary beam shaping is achieved by the use of the cylindrical lens and a spherical lens telescope. The complexity is shifted from uni-axial beam expanders to the need for direct access to the diode emission facet and the need for precise positioning of the cylindrical micro-lens. Beam shaping based on the use of cylindrical micro-

lenses for collimating the fast diverging diode axis was not available for the work discussed in this section. In general, the use of non-diffraction limited sources will always result in a less than unit overlap between the pump beam and the intracavity laser mode.

4.6.3 Diode pumping wavelength selection

Pumping Cr^{4+}:forsterite lasers using near infrared wavelengths ranging from 680-820 nm was demonstrated. This range of pump wavelengths is accessible by a number of commercially available semiconductor laser diode devices on either side of the 740 nm Cr^{4+}:forsterite absorption peak. On the short wavelength side there are InGaAlP diodes ranging from 660-680 nm, at wavelengths longer than 780 nm high power AlGaAs devices can be obtained. At this time no commercial high power devices are available at the highest absorption point at 740 nm but there is no fundamental limitation to developing a device closer to the optimal pump wavelength. Considering that the absorption coefficient is higher in the 660-680 nm range laser diodes at these wavelengths are preferred rather than devices with emission at wavelengths longer than 780 nm.

Broad-area semiconductor diode laser devices with emission at 670 nm are available from various commercial sources and have typical output powers of 500 mW with and emitter widths (parallel to the junction) of 100 μm. Since the Ti:Al_2O_3 laser could not be tuned to 670 nm, it is useful to develop a formalism which relates operation at a known wavelength to other wavelengths. In general it is difficult to extrapolate laser properties to other wavelengths, however, behavior close to threshold is similar for different pump wavelengths and can be predicted with some certainty. It can be assumed that the total power absorbed for a given gain crystal at threshold is a constant such that

$$A(\lambda)\gamma P(\lambda) = \text{const.} \tag{4-8}$$

where $A(\lambda)$ is the fraction of incident power which is absorbed in the crystal and $P(\lambda)$ is the incident power onto the crystal. The quantity γ is the mode coupling efficiency, a measure of best overlap between the gaussian resonator mode and the pump beam within the gain medium; γ equals to unity for a gaussian pump beam, and less otherwise. To determine the feasibility of pumping Cr^{4+}:forsterite lasers using 670 nm broad-area diode lasers the data from pumping with

the $Ti:Al_2O_3$ laser at 740 nm can be used as a benchmark. In practice, the mode coupling efficiency γ needs to be determined experimentally.

4.6.4 Diode pumping of a *z*-cavity Cr^{4+}:forsterite laser

The work on near-infrared pumping presented in the previous sections was done using a standard *z*-cavity with 50 mm radius-of-curvature folding mirrors. For direct diode pumping of gain crystals with modest absorption coefficients ($\alpha(670)\approx 3.8\ cm^{-1}$) and lengths as long as 3 mm to achieve good mode overlap throughout the whole crystal length it is beneficial to have a larger intracavity waist size. In a *z*-cavity, parameters used for modifying the waist size in the crystal are the laser arm lengths and the radius-of-curvature of the folding mirrors. In general, the waist size increases with a decrease in laser arm length or an increase in radius-of-curvature of the spherical folding mirrors. However, with increasing the intracavity waist size it can be expected that the lasing threshold will increase as well. Thus in designing a diode pumped system the waist size and the associated change in lasing threshold may have to be considered along with the optimal overlap between the pump beam and the intracavity resonator mode.

TABLE 4-2: Dependence of intracavity waist inside a 3 mm long Cr4+:forsterite gain crystal for a symmetric *z*-cavity with folding mirrors of radius-of-curvature ROC and arm length *l*. The waist sizes inside the crystal are w_{xC} for tangential, and w_{yC} for the saggital direction at the center of the stability region.

ROC [mm]	*l* [cm]	w_{xC} [μm]	w_{yC} [μm]
50	15	51	32
50	50	26	16
100	15	114	71
100	50	54	34

For work on direct-diode pumping Cr^{4+}:forsterite of a symmetric *z*-cavity with 100 mm radius-of-curvature folding mirrors, a 0.7% output coupler and 15 cm long cavity arms was implemented. A 3.0 mm long Brewster-cut Cr^{4+}:forsterite gain crystal of 0.3% at. Cr was mounted in a water-cooled heat-sink mount and typically maintained at 10°C. The gain crystal was pumped

with a Ti:Al_2O_3 laser at 740 nm and would start lasing at a threshold of about 380 mW of incident pump. Using equation (4-8) the minimum required incident power from a laser diode can be estimated as

$$P(670) = \frac{A(740)}{A(670)} \cdot \frac{1}{\gamma} \cdot P(740) \tag{4-9}$$

where $A(670)$ and $A(740)$ are the fractions of incident power absorbed in the crystal at 670 and 740 nm respectively, γ is the mode coupling efficiency, and $P(740)$ is the incident Ti:Al_2O_3 laser power at threshold. The assumption is made that there is a full overlap between that intracavity resonator mode and the incident Ti:Al_2O_3 laser mode. Using the absorption coefficients in Figure 4-1 for a 3 mm long gain crystal the absorbed powers are $A(670)$=0.68 and $A(740)$=0.95. Thus 400 mW of incident power needed for achieving threshold using a 740 nm TEM_{00} Ti:Al_2O_3 laser translate into (γ·560) mW needed for a broad-area 670 nm diode pump source. This implies that even if unity mode-coupling efficiency was attainable a single 500 mW, 670 nm, laser diode can not provide the 560 mW of pump power necessary for exceeding threshold.

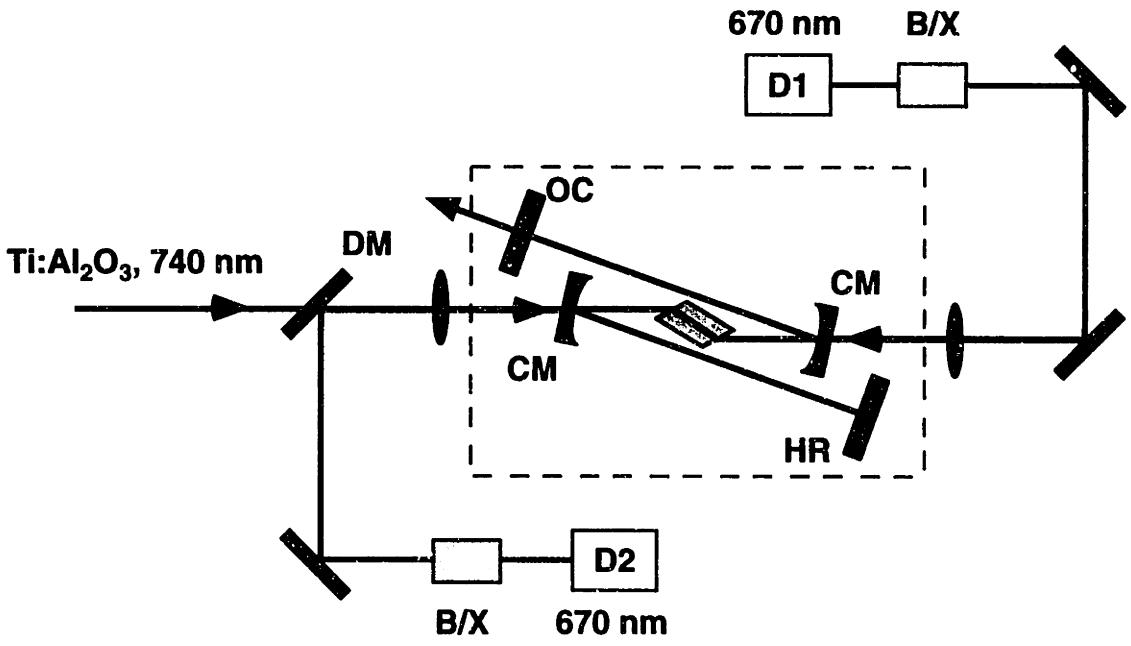

FIGURE 4-21: Experimental set-up for the work on diode pumping of Cr4+:forsterite with 670 nm semiconductor diode lasers. Curved mirrors, CM; high-reflector, HR; output couple, OC; 670 nm pump-diodes, D1 and D2; beam expanders, B/X; DM, dichroic mirror.

To quantify the diode mode coupling efficiency, γ, a system with simultaneous Ti:Al_2O_3 laser and diode pumping was implemented. The Ti:Al_2O_3 laser was used for pumping through one folding high-reflector and the diode pump beam was coupled into the crystal through the second one. First the pump lens and resonator were optimized for operation with the 740 nm Ti:Al_2O_3 laser resulting in an incident threshold pump power of 360 mW. This was followed by a optimization of the resonator for pumping with the added laser diode (D1 in Figure 4-21). The optimization criterion consisted of minimizing the contribution of the Ti:Al_2O_3 pump laser to the total laser threshold. Various diode beam focusing lenses and various beam expansions were tested. Best results were obtained when the diode output was collimated with a Thorlabs Inc. C240TM-B aspheric lens, f_C=8.00 mm, passed through a pair of anamorphic prisms with a beam expansion factor B/X=3.5 in the x-direction, and focused into the crystal with an f_f=76.2 mm lens. The pump-diode used for this work was a *Coherent Laser Group* S-67-500C-100H, 670 nm, 500 mW laser diode with a stripe width of 100 μm and FWHM diffraction angles θ_x=5°, θ_y=22°. After passing through the beam shaping optics and the curved resonator mirror the total incident diode power onto the laser crystal was 400 mW. Using one laser diode (D1) it was possible to reduce the required Ti:Al_2O_3 laser incident power necessary for exceeding threshold to 200 mW. Using equation (4-9) and knowing that P(740)=(360-200) mW and P(670)=400 mW the mode coupling coefficient can be calculated as γ=0.55. One 500 mW rated diode, delivered 400 mW of incident power to the crystal, which was in turn equivalent to 160 mW of incident 740 nm Ti:Al_2O_3 laser power. The equivalent 740 nm Ti:Al_2O_3 laser power is a measure of how much power each diode is actually delivering into the resonator mode. Moreover, the conversion to 740 nm allows for direct comparison with the results obtained in section 4.3.

The measured threshold values shown in Table 4-3 indicate that more than 510 mW of additional incident diode power need to exceed threshold. Thus, two 670 nm, 500 mW, laser diodes are not sufficient to achieve lasing in Cr^{4+}:forsterite. However, in the above discussed set-up specific improvements to the two-diode-pumped system may be sufficient to obtain lasing. The total delivery of the diode emission to the crystal face was about 80%. The loss was divided between the pump transmission through the curved mirror which was 90% and other losses which were due to the beam shaping optics. An increase in transmission combined with an increase in diode output power and/or shift to longer emission wavelengths (710 nm) would yield a significant

TABLE 4-3: Summary of pump powers required to achieve lasing thresholds for the set-up in Figure 4-21. The $Ti:Al_2O_3$ beam is assumed to be a TEM_{00} mode with unity coupling into the cavity mode. The column "ΔDiode" denotes the additional diode power required to achieve threshold without the $Ti:Al_2O_3$ laser. "Equiv. TEM_{00}" is the power equivalent to an incident 740 nm $Ti:Al_2O_3$ beam.

	$Ti:Al_2O_3$ only	$Ti:Al_2O_3$ and one laser diode		
	TEM_{00} @740 nm	TEM_{00} @740 nm	diode @670 nm	Δdiode @670 nm
Incident Power [mW]	360	200	400	510
Absorbed Power [mW]	340	190	272	350
Equiv. TEM_{00} [mW]	—	—	160	200
Mode Coupling	1.00	1.00	0.55	0.55

improvement to exceeding laser threshold. Finally, an overall increase in crystal doping, and the associated increase in the absorption coefficient, would allow to further reduce the crystal length and improve the mode coupling coefficient γ.

4.6.5 Diode pumping of an end-pumped cavity Cr^{4+}:forsterite laser

To achieve better diode-pumping efficiency the laser layout can be changed such that the z-cavity is replaced by an end pumped resonator. In this geometry a Brewster-flat cut crystal is high-reflection coated on the flat end, a curved folding mirror and an output coupler form the laser resonator. One of the advantages to using an end-pumped cavity configuration is that there is the potential for achieving better overlap between the resonator mode and pump beam. In end-pumped lasers the required pump power can be delivered through the high-reflection coated crystal end which allows for closer access to the crystal face. Since there is no folding mirror to pump through, a shorter focal length lens can be used for tighter pump beam focusing into the crystal. In addition, since there is no Brewster interface on the crystal end-pumping allows for efficient pumping with both pump polarizations.

To evaluate the operation of the end-pumped Cr^{4+}:forsterite laser a 4 mm long crystal of 0.3% at. Cr was used. The crystal was cut at Brewster's angle at one end, flat (normal incidence) at the other end where a dielectric coating was deposited. The coating was high reflection at Cr^{4+}:forsterite lasing wavelengths, R(1260)=99.8%, and high transmission at the pump-diode

emission wavelength, T(670)=86%. As in previous cavity configurations the crystal was mounted in a water-cooled copper heat-sink and maintained at 10°C. A 100 mm radius-of-curvature folding mirror and a 0.7% output coupler formed a resonator with an arm length of 15 cm. The cavity was set up such that a 740 nm Ti:Al_2O_3 laser was used for pumping through the curved folding mirror, and the flat crystal end was used for diode pumping.

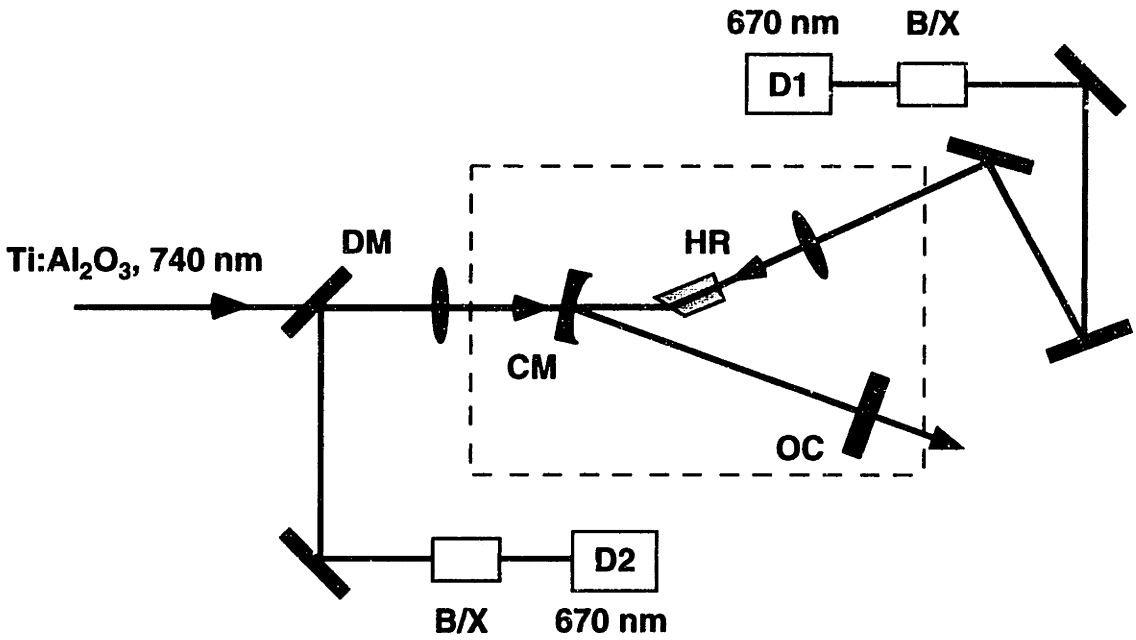

FIGURE 4-22: Experimental set-up for the work on end-pumping of Cr4+:forsterite with 670 nm semiconductor diode lasers. Curved mirrors, CM; high-reflector, HR; output couple, OC; 670 nm pump-diodes, D1 and D2; beam expanders, B/X; DM, dichroic mirror.

The end-pumped cavity configuration allowed for measuring how different diode pump polarizations perform. Typically pump lasers for Cr^{4+}:forsterite laser systems are oriented parallel to the crystallographic *b*-axis. In 1064 pumped systems pumping with the polarization along the *c*-axis is not considered as an option since the absorption coefficient is evan smaller than for the *b*-axis. However, the absorption coefficient for *b*-axis pumping peaks at 740 nm, and for *c*-axis pumping peaks at 660 thus both polarizations can be utilized with 660-720 nm pump sources [38][73]. Even though the absorption coefficients for both polarizations are high enough for efficient pumping, the fluorescence for pumping along the *c*-axis is only half of that for pumping along the *b*-axis [79]. To test actual laser performance the 740 nm Ti:Al_2O_3 pump laser polariza-

tion was oriented parallel to the Cr^{4+}:forsterite *b*-axis providing the necessary power to attain lasing. The threshold for pumping with only the Ti:Al_2O_3 laser the incident threshold pump power was 360 mW.

Using one laser diode (D1) polarized a long the *b*-axis and the Ti:Al_2O_3 laser, it was possible to reduce the contribution of later to the total incident threshold pump power to 190 mW. Using equation (4-9) and knowing $P(740)$=(360-190) mW and $P(670)$=375 mW the mode coupling coefficient can be calculated as γ=0.63. The 500 mW rated diode, delivered 375 mW of incident power to the crystal, which was in turn equivalent to 170 mW of 740 nm Ti:Al_2O_3 laser power. To change the incident pump polarization, a half-waveplate was inserted in the beam path and set such that the polarization was rotated to be parallel to the crystallographic *c*-axis. Under such pumping conditions, to exceed threshold it was necessary to have at least 310 mW of incident Ti:Al_2O_3 pump power. The 500 mW rated diode, delivered 375 mW of incident power to the crystal, which was equivalent to 80 mW of 740 nm Ti:Al_2O_3 laser power.

TABLE 4-4: Summary of pump powers required to achieve lasing thresholds for the set-up in Figure 4-22 using the D1 pump-diode. The column "*b*-diode" contains data for the pump polarization along the *b*-axis (parallel to the emission polarization) and "*c*-diode" is for the pump polarization along the *c*-axis. "Equiv. TEM_{00}" is the power equivalent to an incident 740 nm Ti:Al_2O_3 beam.

	Ti:Al_2O_3 and *b*-axis diode		Ti:Al_2O_3 and *c*-axis diode	
	TEM_{00} @740 nm	diode @670 nm	TEM_{00} @740 nm	diode @670 nm
Incident Power [mW]	200	375	310	375
Absorbed Power [mW]	190	255	295	255
Equiv. TEM_{00} [mW]	—	170	—	80
Mode Coupling	1.00	0.63	1.00	0.63

Implementing an end-pumped Cr^{4+}:forsterite laser allows for more efficient pumping using broad-area pump-diodes. In the this configuration both polarizations can be used with equal crystal insertion loss. However, in Cr^{4+}:forsterite, the pump efficiency is polarization dependent and is along the *c*-axis 45% of the one along the *b*-axis. For either case the laser emission is polarized parallel to the crystallographic *b*-axis. The results in this section indicate that lasing with diode pumping only should be possible with three pump-diodes and an end-pumped Cr^{4+}:forsterite res-

onator. Two diodes can be polarization multiplexed for pumping through the flat crystal end, and one diode for pumping through the curved folding mirror. Three diodes are likely to generate (170+80+160)=410 mW of equivalent 740 nm Ti:Al_2O_3 power and only 360 mW are required to obtain lasing.

4.6.6 Future efforts in direct diode-pumping of Cr^{4+}:forsterite lasers

At this time direct-diode pumping of Cr^{4+}:forsterite lasers, though feasible with three 500 mW, 670 nm pump diodes, can not exceed the proof-of-concept stage. Considering that the diodes can provide at most 50 mW of 740 nm Ti:Al_2O_3 equivalent pump power above threshold, and using the slope efficiency data in Table 4-1, the maximum attainable power is less than 5 mW. The addition of a fourth pump diode (for pumping through the curved folding mirror) could increase the laser output to about 10 mW, too little for practical applications. A change in pump-diode wavelength from 670 nm to 715 nm would however be a very significant development. It can be expected that this shift in the pump wavelength would result in a 20% increase in absorbed pump power and a corresponding increase in output power. Most significant though would be increasing the doping density of Cr^{4+}:forsterite and the resulting increase in the absorption coefficient. A larger absorption coefficient would allow for the use of even shorter gain crystals resulting in a better overlap between the resonator mode and pump beam, or the use of smaller resonator modes in laser crystals, both approaches would result in a more efficient use of incident pump power.

Chapter 5

Optical frequency domain reflectometry using rapid wavelength tuning of a cw Cr^{4+}:forsterite laser

5.1 Introduction

Optical ranging techniques have applications in various fields from engineering to medicine. These techniques can in general be divided into three major categories: optical time domain reflectometry (OTDR) [80], optical coherence domain reflectometry (OCDR) [69], and optical frequency domain reflectometry (OFDR) [81][82]. In OTDR distance measurements are based on time of flight; measuring the time elapsed between when the light source is turned-on and the arrival of a reflection from the target. This method is analogous to microwave radar systems and is very suitable for the measurement of large distances in optical systems with moderate resolution. The limitations on the feature size that can be measured are given by the time discrimination sensitivity of the detection electronics. In comparison, both OCDR and OFDR are based on interferometry and allow for very high resolution axial measurements. In OCDR a broadband light illuminates a Michelson interferometer in which one arm is terminated by the sample under investigation and the other acts as a reference arm in which a moving mirror scans over the axial dimensions of the sample. Interference is observed when the path lengths traveled by reflections from the sample and reference mirror coincide to within a coherence length. This technique requires that the reference arm length be scanned commensurate with the dimensions of the sample making it unsuitable for ranging in large samples. A related technique, known as spectral radar, measures the spectrum of the interferometer output for a fixed delay [83]. In spectral radar, axial information is acquired by Fourier transforming the spectrum so that scanning the reference

arm of the interferometer is not required. OCDR and spectral radar systems utilize broad band light sources (white light sources, superluminescent diodes, mode-locked lasers) and have spatial resolutions which are inversely proportional to the source bandwidth. OFDR uses a similar interferometer configuration, but holds the reference path length fixed and scans the wavelength of a narrow-band source. OCDR, spectral radar, and OFDR have been all been demonstrated for use in optical coherence tomographic imaging systems [69][83][84]. This chapter introduces the use of a rapid wavelength tuned solid-state laser to OFDR applications. A system prototype based on a Cr^{4+}:forsterite laser is presented, but this technique can also be generalized to other solid state laser systems.

5.2 Theoretical background to OFDR

Optical frequency domain reflectometry systems use continuous wave optical sources for which this output frequency is continuously swept through a preset frequency span. Ranging is preformed by means of a Michelson interferometer for which both arms are of fixed length, one terminated by a reference mirror, and the other by the sample under investigation. The signal at the output port of the interferometer is used to recover the reflectivity and relative position the reflections from the sample.

5.2.1 Ranging using tunable cw laser sources

To quantify the operational characteristics of an OFDR system a simple fiber-optic Michelson interferometer will be considered. The two interferometer arms will be of unequal length, one terminated by a mirror with unity reflectivity, and the longer arm will be terminated by a reflector of reflectivity R. For simplicity it will be assumed that the source has a constant amplitude and a linearly changing frequency over time which can be expressed as:

$$E(t) = E_0 e^{j(\omega_0 t + \pi\gamma t^2 + \phi_t)} \tag{5-1}$$

where E_0 is the field amplitude, ω_0 is the initial sweep frequency, γ is the slope of the linear frequency sweep, and ϕ_t is the randomly fluctuating optical phase at time t [85]. The photocurrent at the detector is proportional to the optical field intensity and is a result of interference between the

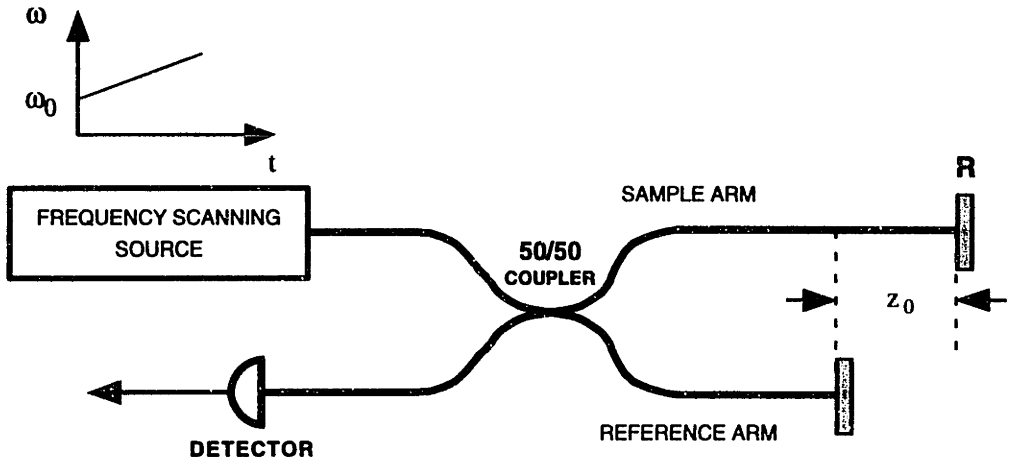

FIGURE 5-1: Schematic of a fiber-optic implementation of OFDR system. One interferometer arm is longer by a distance z_0, and is terminated by a end-mirror of reflectivity R.

optical field from the source with a delayed version of that field. Assuming a 50/50 fiber coupler in Figure 5-1 the optical intensity at the detector is given by

$$I(t) = \left|E(t) + \sqrt{R}E(t-\tau_0)\right|^2 \tag{5-2}$$

where $\tau_0 = 2z_0\left(\frac{n}{c}\right)$ (n is the index of refraction of the optical fiber) is the accumulated delay in the longer interferometer arm. Combining (5-1) and (5-2) and consolidating terms the intensity incident on the detector can be rewritten as

$$I(t) = E_0^2\left[1 + R + 2\sqrt{R}\cos\left(\omega_b t + \omega_0\tau_0 - \frac{1}{2}\omega_b\tau_0 + \phi_t - \phi_{t-\tau_0}\right)\right] \tag{5-3}$$

where $\omega_b=2\pi\gamma\tau_0$ is the beat frequency. In reality the detector performs an integration of the instantaneous optical intensity. Without making any assumptions about the coherence properties of the

source or interferometer arm mismatch, the measured detector signal is proportional to the normalized autocorrelation function of the instantaneous photocurrent and is given by

$$\begin{aligned}\mathbf{R}_{\mathbf{I}}(T) &= \frac{\langle I^*(t)I(t+T)\rangle}{\langle I^*(t)I(t)\rangle} \\ &= (1+R)^2 \\ &\quad +2R\cos(\omega_b T)\cdot\langle\cos(\phi_{t+T}+\phi_{t-\tau_0}-\phi_{t-\tau_0+T}-\phi_t)\rangle \\ &\quad -2R\sin(\omega_b T)\cdot\langle\sin(\phi_{t+T}+\phi_{t-\tau_0}-\phi_{t-\tau_0+T}-\phi_t)\rangle\end{aligned} \tag{5-4}$$

where $\langle\ \rangle$ denotes a time average. This formalism allows to relate the measured interferogram to the time-dependent fluctuations in phase (and frequency) of the source.

If it is postulated that the optical phase fluctuations are a zero-mean random variables, it can be assumed that the phase changes in different time slots are statistically independent. Thus, using $\Delta\phi_t=\phi_t-\phi_{t-\tau}$, and time-averaging relationships

$$\begin{aligned}\langle\cos(\Delta\phi_\tau)\rangle &= e^{-\frac{1}{2}\langle\Delta\phi_\tau^2\rangle} \\ \langle\sin(\Delta\phi_\tau)\rangle &= 0\end{aligned} \tag{5-5}$$

equation (5-4) can be simplified for two separate conditions depending on the relative magnitude between the measurement time T and the time of flight τ_0:

- For $|T|\le\tau_0$:

$$\begin{aligned}\mathbf{R}_{\mathbf{I}}(T) &= (1+R)^2+2R\cos(\omega_b T)\cdot\langle\cos(\phi_{t+T}-\phi_t)\rangle\cdot\langle\cos(\phi_{t-\tau_0+T}-\phi_{t-\tau_0})\rangle \\ &= (1+R)^2+2R\cos(\omega_b T)e^{-\langle\Delta\phi_T^2\rangle}\end{aligned} \tag{5-6}$$

- For $|T|\ge\tau_0$:

$$\begin{aligned}\mathbf{R}_{\mathbf{I}}(T) &= (1+R)^2+2R\cos(\omega_b T)\cdot\langle\cos(\phi_{t+T}-\phi_{t-\tau_0+T})\rangle\cdot\langle\cos(\phi_t-\phi_{t-\tau_0})\rangle \\ &= (1+R)^2+2R\cos(\omega_b T)e^{-\langle\Delta\phi_{\tau_0}^2\rangle}\end{aligned} \tag{5-7}$$

If it is further assumed that the phase (frequency) fluctuations are generated by a laser with a Lorentzian lineshape, the variance $\Delta\phi_\tau$ can be related to the laser emission linewidth $\delta\lambda$ as

$$\langle \Delta\phi_\tau^2 \rangle = 2\frac{|\tau|}{\tau_c} \tag{5-8}$$

where the laser coherence time is defined

$$\tau_c = \frac{1}{\pi}\frac{\lambda^2}{\delta\lambda}\frac{n}{c}. \tag{5-9}$$

Substituting expression (5-8) into (5-6) and (5-7) the final expression for the measured photodetector current can be obtained to be:

- For $|T| \le \tau_0$:

$$\mathbf{R_I}(T) = (1+R)^2 + 2R\cos(\omega_b T)e^{-2\frac{|T|}{\tau_c}} \tag{5-10}$$

- For $|T| \ge \tau_0$:

$$\mathbf{R_I}(T) = (1+R)^2 + 2R\cos(\omega_b T)e^{-2\frac{\tau_0}{\tau_c}}. \tag{5-11}$$

To summarize, the above expressions describe the measured detector current for a Michelson interferometer with unequal arm lengths $z_0 = \frac{1}{2}\tau_0\left(\frac{c}{n}\right)$. At the interferometer input was a laser source for which the center frequency was linearly changed over time. The source had random frequency fluctuations corresponding to a Lorentzian source of linewidth $\delta\lambda$. The first operating region is the case for which the interferometer arm mismatch is very large (large value of τ_0) compared to the measurement time T. These terms, although not typically representative of operating conditions in actual OFDR ranging measurements, do have to be considered when evaluating the signal to noise performance and will be discussed in section 5.2.2. Equation (5-11) describes the operating region of typical OFDR ranging systems and is used to recover the axial distance and reflectivity information of samples.

The information about the interferometer arm mismatch, z_0, is frequency encoded in the beat frequency $\omega_b=2\pi f_b$. To recover this information the spectral density function corresponding to the photocurrent can be obtained by taking the Fourier transform of the combined time dependent functions described by equations (5-10) and (5-11). This results in a general expression for the spectral density of the photocurrent:

$$S_I(f) = \int_{-\infty}^{+\infty} \mathbf{R_I}(T)e^{-j2\pi fT}dT$$

$$= (1+R)\delta(f) + 2Re^{-2\frac{\tau_0}{\tau_c}}\delta(f \pm f_b)$$

$$+ \frac{R\tau_c}{1+\pi^2\tau_c^2(f \pm f_b)^2}\left\{1 - e^{-2\frac{\tau_0}{\tau_c}}\left[\cos(2\pi(f \pm f_b)\tau_0) + \frac{2\tau_0}{\tau_c}\frac{\sin(2\pi(f \pm f_b)\tau_0)}{2\pi(f \pm f_b)\tau_0}\right]\right\}. \quad (5\text{-}12)$$

The first term in the spectral density is a delta function at dc which corresponds to the average level of optical power incident on the photodetector. The second term is a delta function centered at the beat frequency and scaled by a decaying exponential containing the ratio of the interferometer arm mismatch and the source coherence length. This is the term which contains the frequency encoded distance information used in optical ranging and the magnitude of this term contains information about the reflectivity of the sample investigated. However, as the time of flight τ_0 approaches the coherence time of the optical source τ_c, the amplitude of the reflections signal is reduced and consequently does affect the signal-to-noise performance. The last term in equation (5-12) is a continuous function of the frequency and is strongly dependent on the coherence time of the optical source used. This term is centered at the beat frequency and can be thought of as the phase or frequency noise of the optical source. In an ideal optical source with a delta-function lineshape this term would be zero.

Up to this point it was assumed that the amplitude of the laser is constant throughout the entire frequency sweep and the frequency ramp was of infinite duration with no tuning limitations. In reality of course, the laser output has a limited tuning range as well as an output intensity profile which both affect the OFDR system performance. The larger the tuning range of the optical source the finer the spatial resolution of the OFDR system. To illustrate this dependence a

source of constant electric field for all emission frequencies, and zero otherwise is considered. Moreover, to simplify the analytic expressions it will be assumed that an ideal tunable source ($\phi_t \to 0$ and $\tau_c \to \infty$) is used such that the autocorrelation equation (5-4) can be rewritten as:

$$\mathbf{R_I}(T) = \begin{cases} (1+R)^2 + 2R\cos(\omega_b T) \ldots -\frac{1}{2}\Delta T \le T \le \frac{1}{2}\Delta T \\ 0 \ldots \text{otherwise} \end{cases} . \tag{5-13}$$

If equation (5-13) is thought of as the multiplication of a square emission spectrum with the interferogram function the spectral density function can be written as a convolution of the Fourier transform of a square pulse and the Fourier transform of the non-zero part of $\mathbf{R_I}(T)$ such that:

$$S_I(f) \sim \left[\frac{\sin(\pi f T)}{\pi f T}\right]^2 \otimes [(1+R)\delta(f) + 2R\delta(f \pm f_b)] \tag{5-14}$$

and the spectral density function can then be evaluated as:

$$S_I(f) \sim (1+R)\left[\frac{\sin(\pi f \Delta T)}{\pi f \Delta T}\right]^2 + 2R\left[\frac{\sin(\pi(f \pm f_b)\Delta T)}{\pi(f \pm f_b)\Delta T}\right]^2 . \tag{5-15}$$

Applying the Rayleigh criterion [86] to an OFDR system described by equation (5-15) the resolving power (resolution) is set by $\Delta f_{min}=(\Delta T)^{-1}$ such that the smallest separation for which two similar reflectors can be resolved is given by

$$\Delta z_{min} = \frac{1}{4}\left(\frac{c}{n}\right)\frac{1}{\Delta \nu_{max}} = \frac{1}{4}\cdot\frac{\lambda_0^2}{\Delta\lambda_{max}} \tag{5-16}$$

where $\Delta\nu_{max}$ and $\Delta\lambda_{max}$ are the tuning range and λ_0 is center wavelength of the optical source. However, this calculated resolution may not represent the actual resolution in an OFDR system. These issues are of particular importance when this ranging system is used in conjunction with a sample consisting of multiple reflection planes of unknown reflectivities (or a multiply scattering medium). Various reflections may have to be resolved from a single photocurrent signal. The nature of the *sinc* function results in the appearance of sidelobes adjacent to the main signal at the beat frequency which can obscure any adjacent reflection signals. Sidelobes can be eliminated by

using light sources with non-square emission spectra for which the Fourier transforms decay to the noise floor without sidelobes.

For an optical source that can be tuned over a frequency range with an overall Gaussian tuning profile, smooth Gaussian autocorrelation signals at the beat frequencies can be expected. In general, for a source with a gaussian tuning profile and a wavelength FWHM of $\Delta\lambda$, centered at λ_0, the system resolution can be calculated to be

$$\Delta z_{min} = \frac{2\ln(2)}{\pi} \cdot \frac{\lambda_0^2}{\Delta\lambda_{max}}. \tag{5-17}$$

The use of a rectangular tuning profile results in a narrower FWHM of the spectral density function than in the case of a Gaussian tuning profile. However, as the tuning profile of the light source becomes more rectangular, the sidelobes of the spectral density function increase and can obscure signals from adjacent reflectors which reduce the effective system resolution.

5.2.2 Signal-to-noise considerations

Measurement systems are considered to be operating with the best signal-to-noise performance when optimized such that shot-noise dominates all other sources of noise. Shot-noise arises from current fluctuations due to the conversion of light into the electrons. This noise has a constant spectral density function and is commonly referred to as *white noise*. However, in practice this signal-to-noise figure may be difficult to attain and the actual values are strongly dependent on the performance of the optical source. To gain an understanding of engineering limitations to the signal-to-noise performance of an ODFR system the second and third term in equation (5-12) have to be closely examined.

The second term in equation (5-12) represents the *signal* centered at a frequency relating it to the sample position and reflectivity. However, the amplitude of this term is scaled by a term dependent on the ratio of the delay and source coherence time. Thus, there is an appreciable signal degradation for large delay times. The third term is a continuous function of photocurrent frequency and is strongly affected by the delay and source coherence time. This term represents the distribution of the phase noise around the beat frequency. For an ideal case where the source is

represented by a tunable delta-function ($\phi_t \to 0$ and $\tau_c \to \infty$) this term would vanish. The relative magnitude of these two terms can be seen in Figure 5-2 as a function of interferometer arm mismatch normalized to the source coherence length. The traces were calculated assuming unity

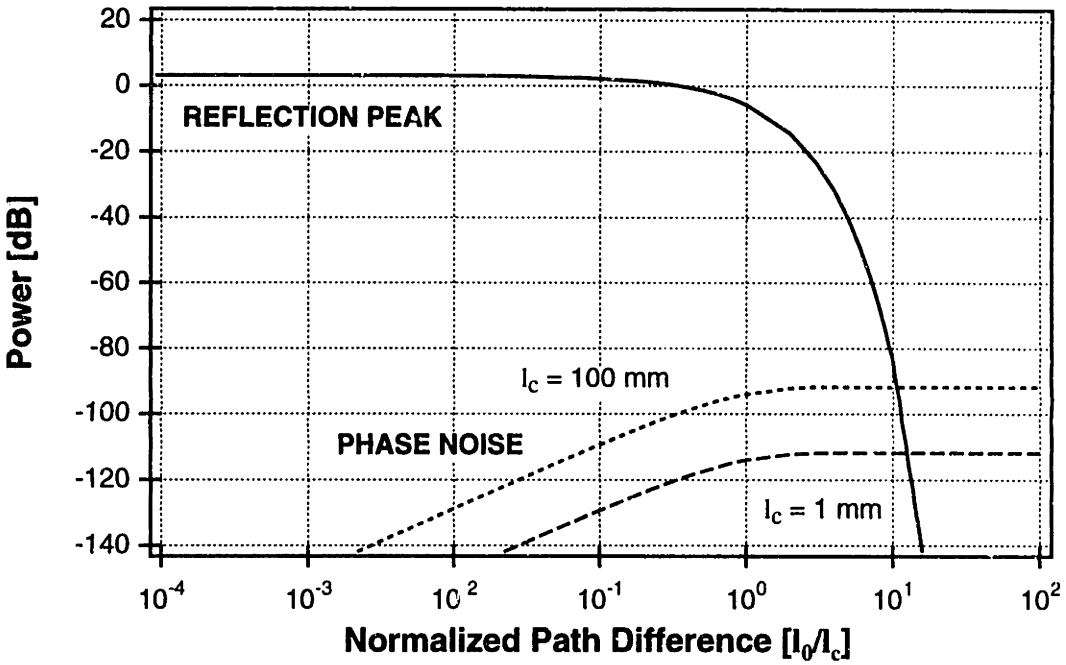

FIGURE 5-2: Normalized beat signal magnitude and phase noise as functions of interferometer arm mismatch normalized to the source coherence length. The curves were calculated for a high-reflector in the sample arm, and the phase noise was evaluated for sources with coherence lengths of 1 mm and 100 mm.

reflectors in both interferometer arms and source coherence lengths of 1 mm and 100 mm. The *reflection peak* curve is the signal magnitude of the second term, whereas the *phase noise* curve is magnitude of the third term in equation (5-12). It can be seen that the ranging signal remains fairly constant until the interferometer arm mismatch becomes comparable to the coherence length of the optical source at which point it becomes subject to a sharp decrease. The phase noise increases monotonically with increasing ranging distance up where the interferometer arm mismatch equals to the coherence length at where it flattens out. The actual magnitude of the phase noise in Figure 5-2 does depend on the specific value of source coherence length but the qualitative features are representative of the general OFDR system behavior. Thus in actual systems the scan length should be kept to less than one coherence length.

From Figure 5-2 it can be seen that shot-noise limited operation may be possible for interferometer mismatches smaller than the source coherence length. The effects of classical noise from the optical source (amplitude fluctuations and 1/f noise) can in general be significantly reduced by the use of a dual-balanced detection configuration. Such configuration will also eliminate the first (dc) term in equation (5-12) and allow for amplification of the detected optical beat signal without saturation of the electronic amplifier. An additional limiting factor in obtaining good signal-to-noise performance can be the dynamic range of the analog-to-digital converter used for digitizing the data. However, to assure best OFDR system performance it is necessary to operate in a regime of low phase noise by keeping the scan lengths to less than the coherence length of the optical source.

5.2.3 Frequency vs. wavelength tuning

When modeling the OFDR system the optical source was one for which the frequency was varied as a linear function of time such that:

$$\nu(t) = \nu_0 + \frac{1}{2}\gamma t . \tag{5-18}$$

In some applications, including the ones discussed in the following sections, it is the wavelength of the source which is a linear function of time such that:

$$\lambda(t) = \lambda_0 + \frac{1}{2}\gamma t , \tag{5-19}$$

and a linear wavelength function corresponds to a non-linear time dependency of the frequency:

$$\nu(t) = \frac{c}{\lambda_0 + \frac{1}{2}\gamma t} . \tag{5-20}$$

This functional, dependence results in a prohibitively complex analytical analysis of OFDR ranging systems. Fortunately under certain operating conditions equation (5-20) can be approximated by (5-18) such that the formalism developed in this section can also be applied to the understanding of OFDR systems for which the wavelength is tuned as linear function of time. For this pur-

pose equation (5-20) is compared to the best line fit to the linear dependence described by (5-18). The magnitude of the residuals between the data and the linear fit are a measure of this approximation. Figure 5-3 is a simulation of a laser source tuned from 1175 to 1375 nm in 4 ms, the solid

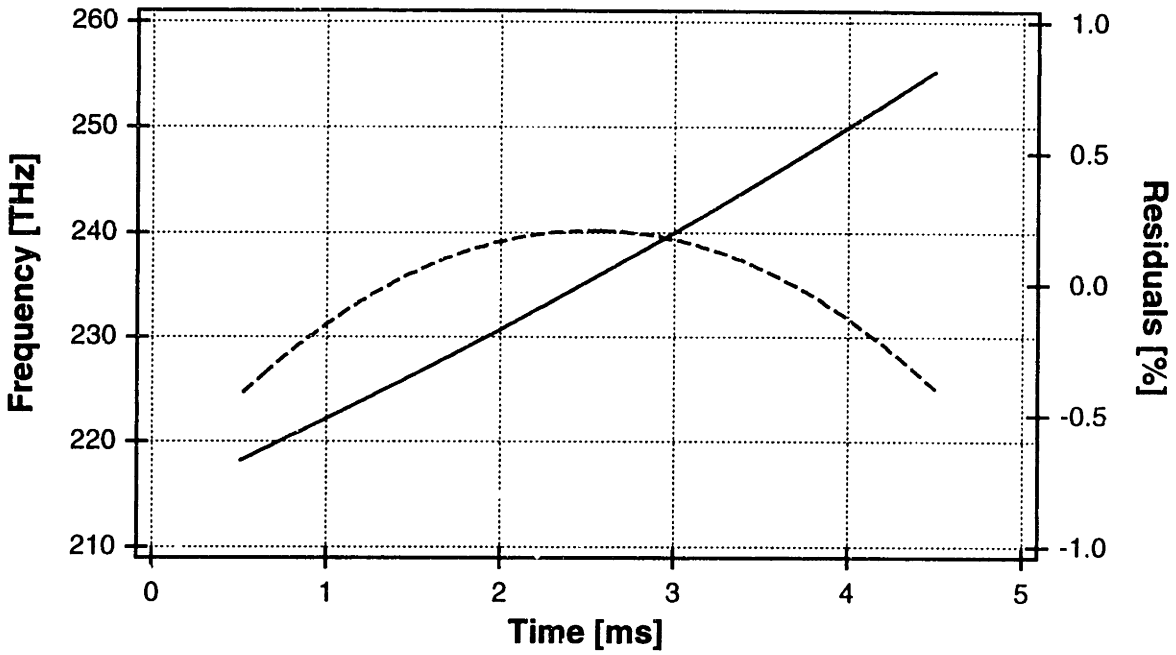

FIGURE 5-3: The solid line represents the calculated frequencies for linear wavelength tuning described by equation (5-20). The dashed line are the normalized residuals between the data and best line fit. This frequency range corresponds to a linear wavelength sweep of the Cr^{4+}:forsterite cw operating range from 1175 to 1275nm.

line shows the frequency time function for a linear wavelength sweep. The residuals are a percentage deviation from a best line fit to the solid line. The deviation is less than 0.5% for a 200 nm tuning range and the fit can be improved if a smaller tuning range is utilized.

In general, as long as the frequency sweeps are near-linear the OFDR system analysis developed in this section can be applied and the relative reflectivity and position of a sample can be obtained by calculating the Fourier transform of the detector photocurrent signal. For the instance of linear frequency tuning there will be a linear dependence between the beat frequency and interferometer arm mismatch. For this to be experimentally verified high-reflectors should be placed in

both interferometer arms and the beat frequency recorded as function of the relative length change. If a near-linear beat frequency *vs.* interferometer arm mismatch dependence can not be obtained, other formalisms must be developed [87][88][89].

5.3 Rapidly tuned cw Cr^{4+}:forsterite laser

In OFDR systems, the path length differences between the sample and reference arm reflections cause variations in the beat frequencies of the detector signal. Since larger path differences result in larger modulation frequencies, taking the Fourier transform gives a reflectivity profile as a function of frequency which can in turn be related to the sample dimensions. In general, the wider the span of frequencies the source sweeps through, the finer the axial resolution. Likewise, the faster the frequencies are swept, the faster the data acquisition. Previous work in the use of tunable sources for OFDR was typically based on frequency tunable semiconductor diode laser systems. Frequency tuning in these systems utilized current tuning [90], thermal tuning [91][89], acousto-optic tuning [81], or gratings placed in external cavities with semiconductor amplifiers [92][84]. Also, a temperature tunable Nd:YAG ring laser [82], and tunable dye laser [93] were used as sources for OFDR systems. Recent work in optical coherence tomography systems (OCDR systems) led to the use of mode-locked solid-state lasers in medical imaging application [64][65]. In these applications mode-locked operation of these lasers resulted in broad emission bandwidths and permitted very high axial ranging resolution. The 200 nm cw tuning range of Cr^{4+}:forsterite presented in section 4.3.3 motivated implementation of a rapidly tuned version for OFDR application. This source would be capable of matching the resolution of OCDR systems based on more complex mode-locked Cr^{4+}:forsterite lasers.

5.3.1 Tunable laser layout

In OFDR systems, it is important that the cw laser operation has a narrow and stable emission band which can be continuously tuned over a large wavelength range. To assure a large axial resolution it is important that the intensity profile is smooth (gaussian-like) and that the Fourier transform is without significant sidelobes. Narrow linewidths in lasers are achieved by placing wavelength filtering elements such as gratings, Fabry-Perot etalon filters, birefringent filters, or prisms in the resonator. Intra-cavity gratings can provide a very narrow filter function, but are too

lossy to be suitable for use with low gain laser systems like Cr^{4+}:forsterite. Fabry-perot etalons can be designed to have a very narrow bandwidth but a single etalon with a free spectral range sufficiently large to cover the whole tuning range not Cr^{4+}:forsterite would be too small for practical use. The use of a sequence of multiple etalons is possible but increases the complexity of the optical system. A birefringent filter can be inserted at Brewster's angle for low loss, but can typically not be rotated sufficiently fast to provide for rapid laser tuning over a broad bandwidth. Wavelength selection in a laser resonator can also be achieved with the use intracavity dispersive prisms placed in front of a cavity end-mirror (see section 4.3.3). Continuous tuning of the laser can be achieved by angular deflection of the cavity end-mirror and multiple prisms can be used in sequence to provide stronger wavelength filtering. In general, the actual number of prisms needed for a specified narrow line operation will depend on the laser wavelength, and the choice of particular prism material.

The Cr^{4+}:forsterite laser used for this work consisted of a standard astigmatism compensated z-cavity with four dispersive prisms for continuous wavelength selection. The cavity arm lengths were set to 50 and 70 cm, with two 50 mm radius-of-curvature folding mirrors, and a 0.7% output coupler. A 3.0 mm long Brewster-cut Cr^{4+}:forsterite gain crystal of 0.3% at. Cr was mounted in a water-cooled copper heat-sink mount and typically maintained at 10°C. The gain crystal was padded with thin indium foil and compressed into the water-cooled copper mount to achieve good thermal contact and temperature control. The crystal was oriented for pumping along the crystallographic *a*-axis with the pump polarization incident parallel to the *b*-axis. The pump laser, a *Coherent Mira 900* Ti:Al_2O_3 laser pumped by a *Coherent Innova 200* argon-ion laser, was optimized for cw operation at 740 nm, with an average output power of 2 W. The curved folding mirrors used to characterize near-IR pumping of a Cr^{4+}:forsterite laser were optimized for operation with a 1064 nm pump. Consequently the pump transmission through the curved folding mirrors measured T(740 nm)=51% resulting in the absorption of about 50% total pump power. Narrow band operation of the solid state laser in this system was achieved by using a sequence of four dispersing prisms as an intra-cavity filter. A sequence of two SF6 prisms, was followed by a sequence of LaFN28 prisms with approximately 10 cm separation between each prism. The cavity end-mirror was a bare gold coated pyrex substrate placed on the shaft of a *Cambridge Technologies 6800* mirror positioning system. Depending on the amplitude of the drive

signal an angular tilt of up to ±10° at frequencies of up to 1 kHz could be achieved. The reflectivity bandwidth of the curved mirrors and output coupler was identical to the one used to obtain the 200 nm cw tuning range reported in section 4.3.3.

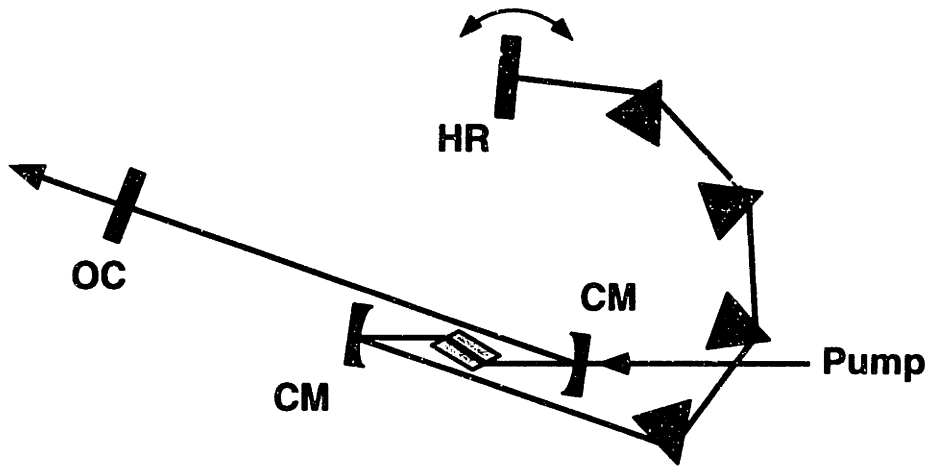

FIGURE 5-4: Schematic of the rapid wavelength tuning Cr^{4+}:forsterite laser. Standard z-cavity with four dispersive prisms for narrow-band tunable cw operation. OC, output coupler; CM's, 50 mm radius-of-curvature folding mirrors; HR, bare-gold high reflector mounted on a tilting galvanometer.

To characterize the angular tuning sensitivity the laser output wavelength was recorded as a function of the high-reflector tilt angle. Depending on the wavelength the prisms will refract the incident beam at a slightly different angle. Only a narrow range of wavelengths will be reflected back into the resonator by the end mirror. Wavelength tuning becomes more selective the larger the wavelength dependent angular dispersion. A larger angular frequency spread can be achieved with either, the use of prism materials with higher index of refraction, or with the use of a sequence of multiple dispersing prisms. To minimize intracavity losses, the apex angle should be chosen such that the incident and exit rays are at Brewster's angle, eliminating losses for *p*-polarized beams. The apex angle to choose is

$$\text{Apex} = \pi - 2\theta_B(\lambda_0) \tag{5-21}$$

where $\theta_B(\lambda_0)$ is Brewster's angle at the center wavelength.

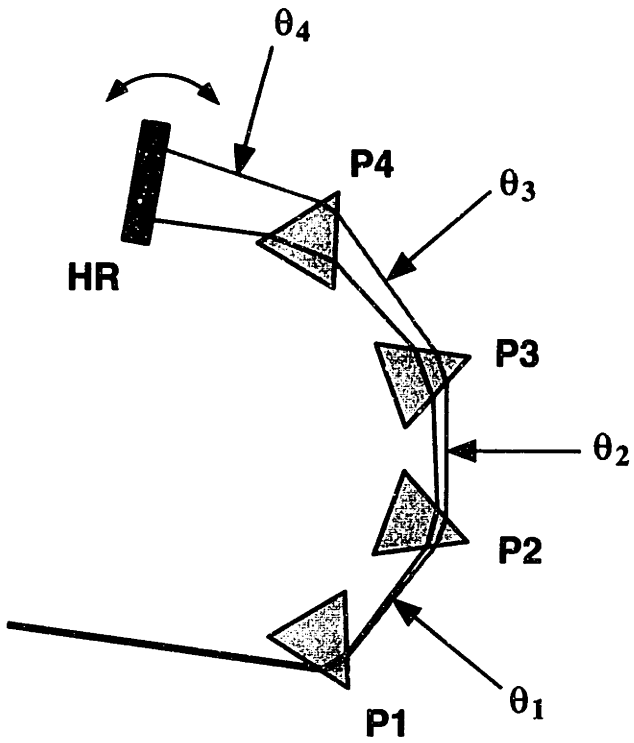

FIGURE 5-5: Dispersive prism sequence used for frequency tuning of the laser shown in Figure 5-4. Theoretical data for the angular dispersion are given in Table 5-1, experimental data are shown in Figure 5-6.

To measure the angular tuning dependence of the laser the high-reflector was tilted in steps such that at each point steady state laser operation was obtained. Tilting of the end-mirror through an angle of 0.61° continuously tuned the laser wavelength from 1200 to 1275 nm. The measured angular wavelength spread is in good agreement with the calculated values shown in Table 5-1. A

TABLE 5-1: Angular wavelength dispersion for a sequence of four Brewster's prisms shown in Figure 5-5. The Brewster's angles were calculated at a center wavelength of 1235 nm, and the angular dispersion, θ, was obtained using a range of wavelengths from 1200 to 1270 nm.

Prism Position	Prism Material	θ [deg.]
P1	SF6	0.170
P2	SF6	0.339
P3	LaFN28	0.483
P4	LaFN28	0.626

linear relationship between the tilt angle and the output wavelength was measured, thus as long as a linear angle-change of the end-mirror can be maintained one can expect a linear change in laser output wavelength. However, to fully verify the suitability of this tuning mechanism for OFDR measurements it has to be assured that a linear scan of end-mirror tilt indeed results in a near-linear change of the laser output frequency (see section 5.2.3). A comparison of the actual angular change in frequency and the best line fit to the data in Figure 5-6 indicated a high degree of linearity.

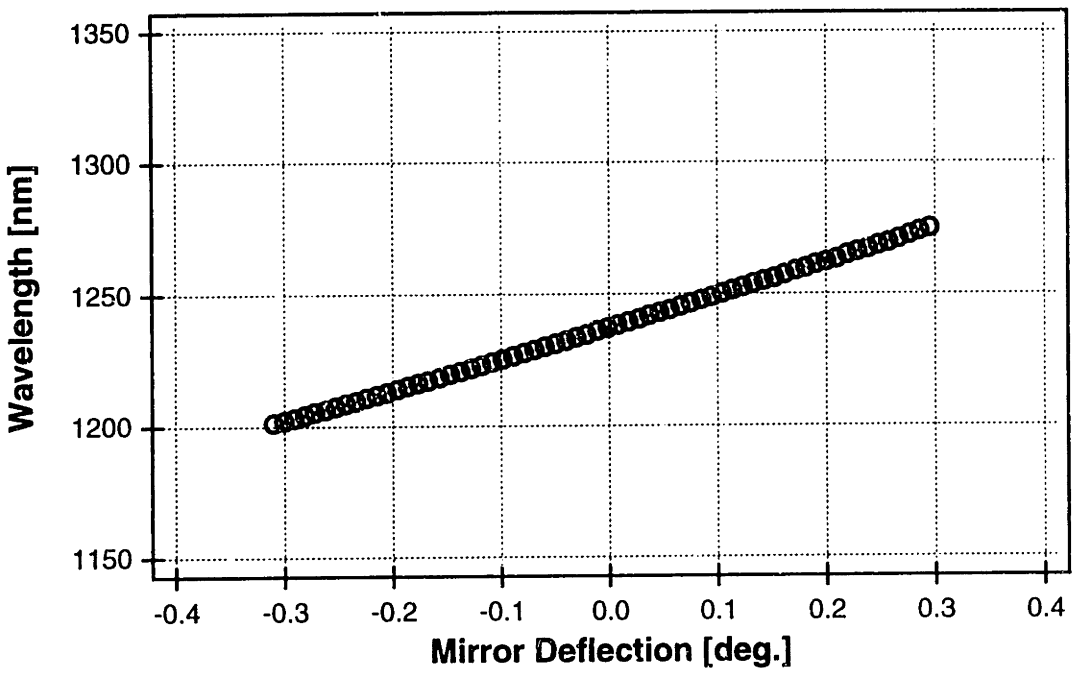

FIGURE 5-6: Laser output wavelength as a function of high-reflector tilt angle.

This laser was typically operated such that 0.9 W of the pump power was absorbed in the crystal and a maximum output power of 9 mW was obtained. The obtained wavelength tuning range of 75 nm is less than the 200 nm reported in section 4.3. One of the factors for diminished laser performance can be attributed to the fact the some of the prisms (LaFN28) were not cut for Brewster's angle operation at the actual center wavelength. In addition, the bare-gold coating of the high-reflector was of poor quality, and due to it's softness could not be effectively cleaned. Both of these factors result in increased cavity losses and account for the decrease in tuning range and output power. The use of low-loss, Brewster's angel cut prisms and a dielectric coated high-

reflector should result in a tuning range and output powers comparable to those presented in section 4.3. Another quantity of importance for OFDR systems is the laser linewidth. The linewidth measurement was performed using a HP 70004A optical spectrum analyzer (OSA) and averaging 5000 spectrum traces with a resolution of 0.08 nm. The average linewidth (FWHM) for the laser with only two prisms (SF6) was measured to be 1.0 nm, and a laser with all four prisms (2×SF6 and 2×LaFN28) was 0.2 nm. For a 1.2 m long laser cavity, a 0.2 nm emission linewidth spans more than 300 cavity modes which are in competition for the same available gain. The measured linewidth of 0.2 nm corresponds to a coherence length of 3.7 mm and a coherence time of 12.4 ps.

The laser geometry presented allows for rapid laser wavelength tuning by tilting of the high-reflector and the tuning rate is determined by the high-reflector rotation speed. Measurements of the laser characteristics under step-by-step tuning indicate suitability for use in high-resolution OFDR system. However, the tuning behavior for the case of step-by-step tuning may not be representative to the rapid-tuning specifications thus it is necessary to evaluate the actual laser performance when part of an actual OFDR system.

5.3.2 OFDR system performance

The OFDR system was based on a wavelength tunable Cr^{4+}:forsterite laser for which the wavelength tuning rate could be continuously varied up to 1 kHz. The galvanometric end-mirror positioning system was driven with a symmetric triangle drive waveform. This galvanometric actuator was equipped with a shaft position encoder providing feedback on the actual mirror deflection such that the linearity of the tilt rate was continuously monitored on an oscilloscope. The high-reflector tilt rate was a linear function of time for all drive frequencies, implying a linear change in optical frequency as a function of time.

The output of the laser was coupled into a fiberoptic Michelson interferometer with dual-balanced detection. One of the interferometer arms was terminated by a high-reflector, reference mirror, and a sample of interest could be placed into the other arm. The sample was placed onto translation stages allowing for positioning in the plane orthogonal to the optical propagation axis. However, for the purpose of characterizing the OFDR system the sample arm was made to be identical to the reference arm but with a high-reflector placed on a translation stage which could

be moved along the optical axis. The translation stage allowed the measurement of the OFDR beat frequency for known path delays and to characterize system performance. A polarization controller was also placed in the reference arm and used to cancel out any polarization imbalance in the interferometer

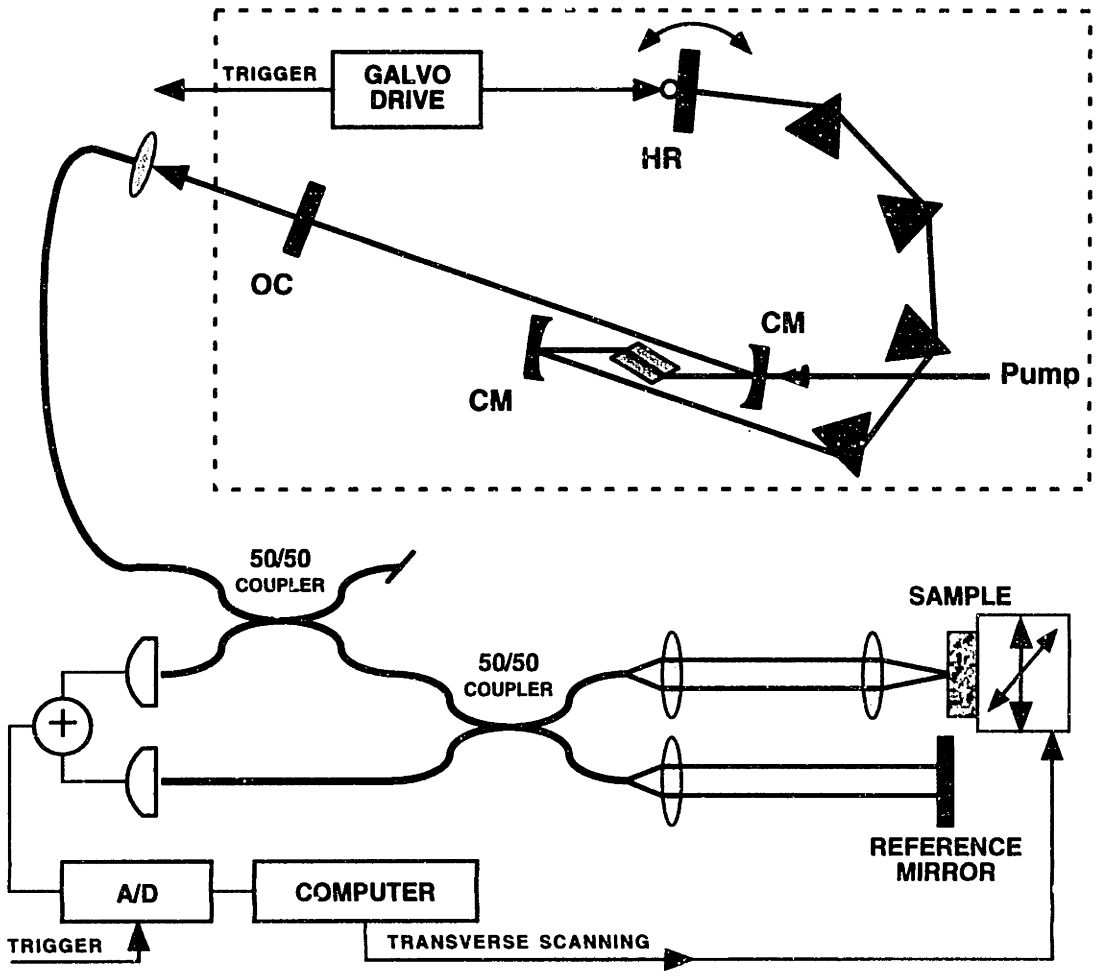

FIGURE 5-7: Schematic diagram of the experimental set-up. Rapidly wavelength tunable cw Cr^{4+}:forsterite laser, fiber-optic Michelson interferometer and data acquisition components for OFDR measurements.

Dual-balanced detection was used to eliminate the dc-term in equation (5-12), as well as to minimize the effects of laser noise in the emission spectrum. The ac-coupled detector signal was measured by a *LeCroy* 7400A 150 MHz digital oscilloscope which was also used as an 8-bit analog-to-digital (A/D) converter. To reduce the system noise bandwidth the detector signal was passed through a 20 MHz low-pass filter. This cut-off frequency was well above any of the beat

frequencies used in this system. The gain of the oscilloscope was always maximized in order to utilize the full dynamic range of the A/D converter. The digitized oscilloscope traces were transferred to a computer for processing and display.

To verify laser tuning at OFDR scanning speeds the laser output and high-reflector angular deflection were recorded as a function of time. In addition, the laser output was also measured by an OSA. Because of its relatively slow scan speed, the OSA was operated in the peak-hold mode with 5000 scans recorded to obtain a representative spectrum. The OSA data represent the true, calibrated wavelength tuning range of the laser. When using the wavelength *vs.* mirror deflection calibration from Figure 5-6 it was possible to extract the wavelength tuning range of a single scan. The trace in Figure 5-8a is a single scan of the laser output. The trace in Figure 5-8b is the result of 5000 peak-hold OSA scans. Both traces were acquired with the galvo driven with a 100 Hz triangle waveform and remained virtually unchanged for drive frequencies up 1 kHz. The fact that both measurements led to equivalent results confirms that the tuning range and spectrum shape remain unchanged with increasing tuning rates. Thus, a wavelength calibration obtained from the step-by-step calibration (i. e. Figure 5-6) can be applied to other tuning rates and is representative for the use in OFDR applications.

In order to investigate the performance of the OFDR system for high speed ranging the laser was operated with high-reflector scan frequencies up to 1 kHz. Figure 5-9 shows the digitized interferograms and the corresponding 16-bit fast-Fourier-transforms (FFT) for 100 Hz, and Figure 5-10 for a 1 kHz triangle-wave drive. As expected, different arm mismatches are encoded as different modulation frequencies of the measured interferograms. The interferogram modulation frequency was calculated for a range of optical path mismatches and verified the linear relationship between these two quantities (see Figure 5-11). Since OFDR measures the absolute path difference between two interferometer arms to the beat frequency of the interferogram, it is not possible to distinguish which of the arms is actually longer. To avoid misinterpretation of acquired data it is important that the reference arm is always shorter than the distance to the sample under investigation. The FWHM of the Fourier transforms in Figures 5-9 and 5-10 set the axial spatial resolution of the as 15 μm and is in close agreement with the value expected form the laser spectrum shown

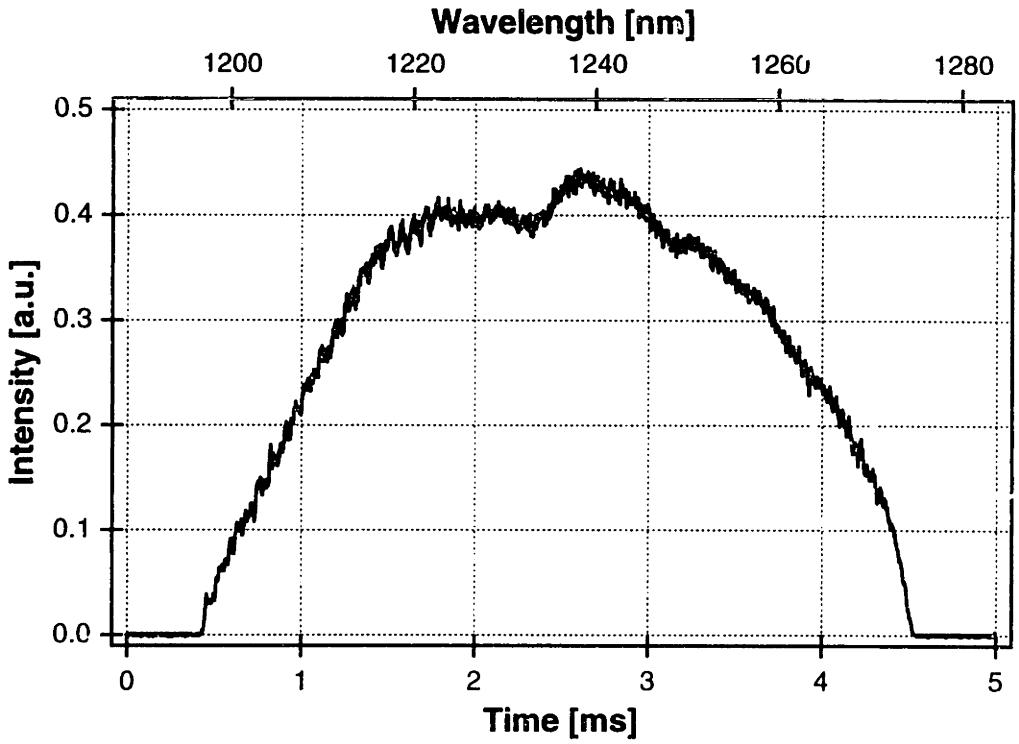

(a)

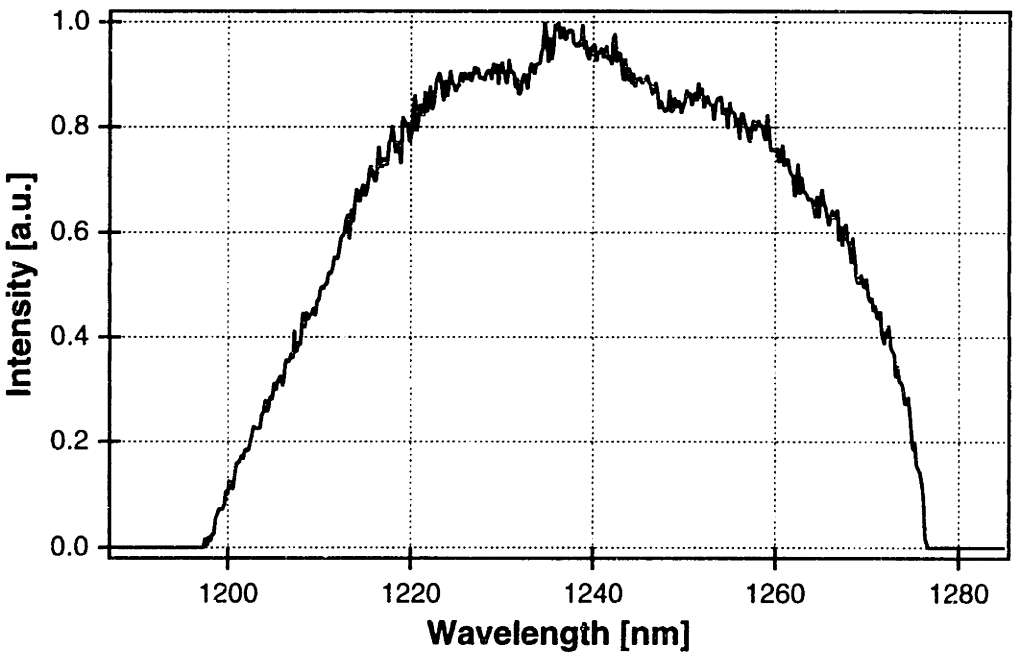

(b)

FIGURE 5-8: (a) Laser output as a function of scan time. Wavelengths were obtained using Figure 5-6. (b) Normalized peak-hold spectrum, 5000 traces.

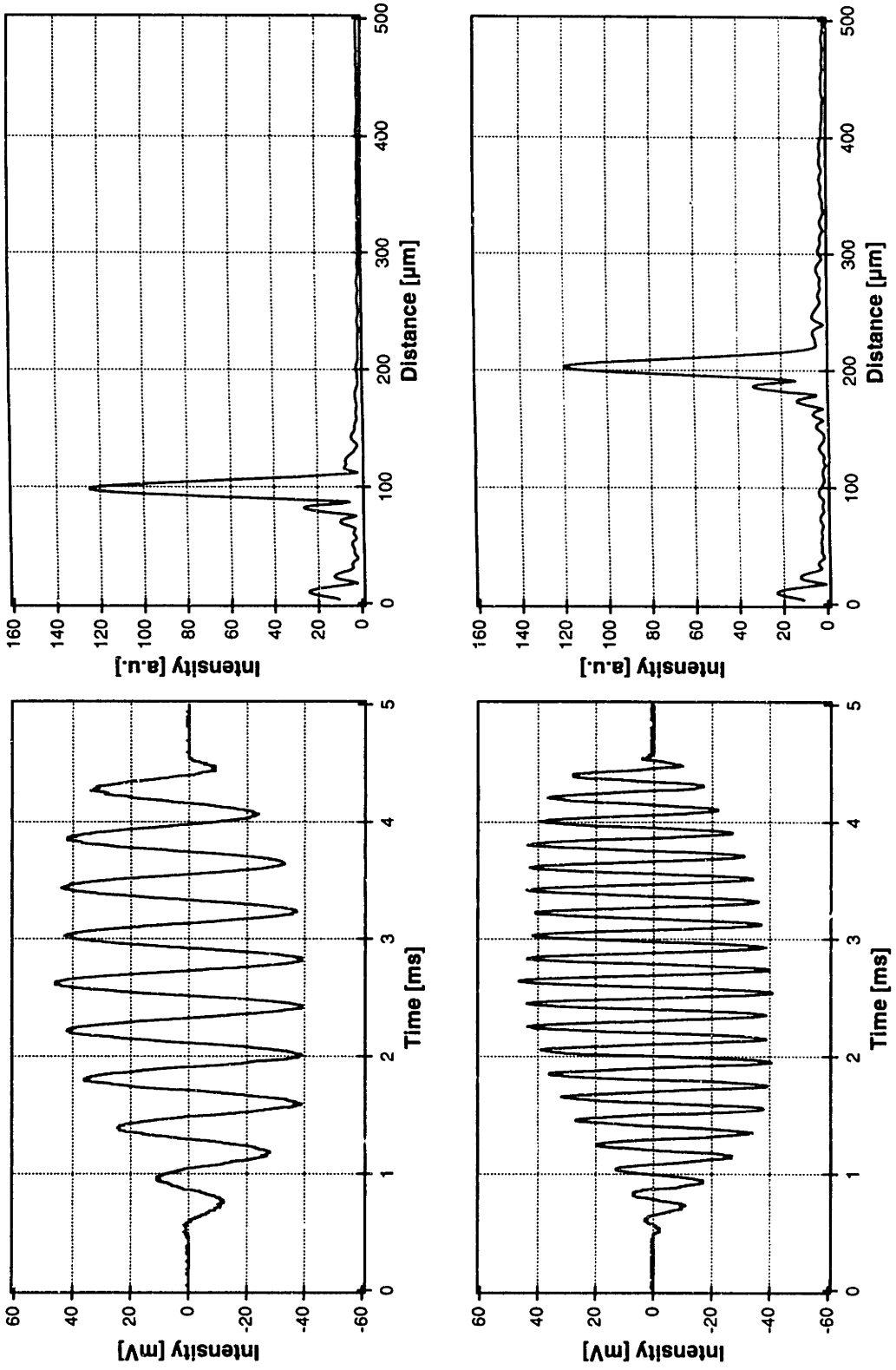

FIGURE 5-9: Interferograms for 100 and 200 μm arm length difference of the Michelson Interferometer and the corresponding Fourier transforms. The tuning frequency was 100 Hz and resolution of the system was measured to be 15 μm.

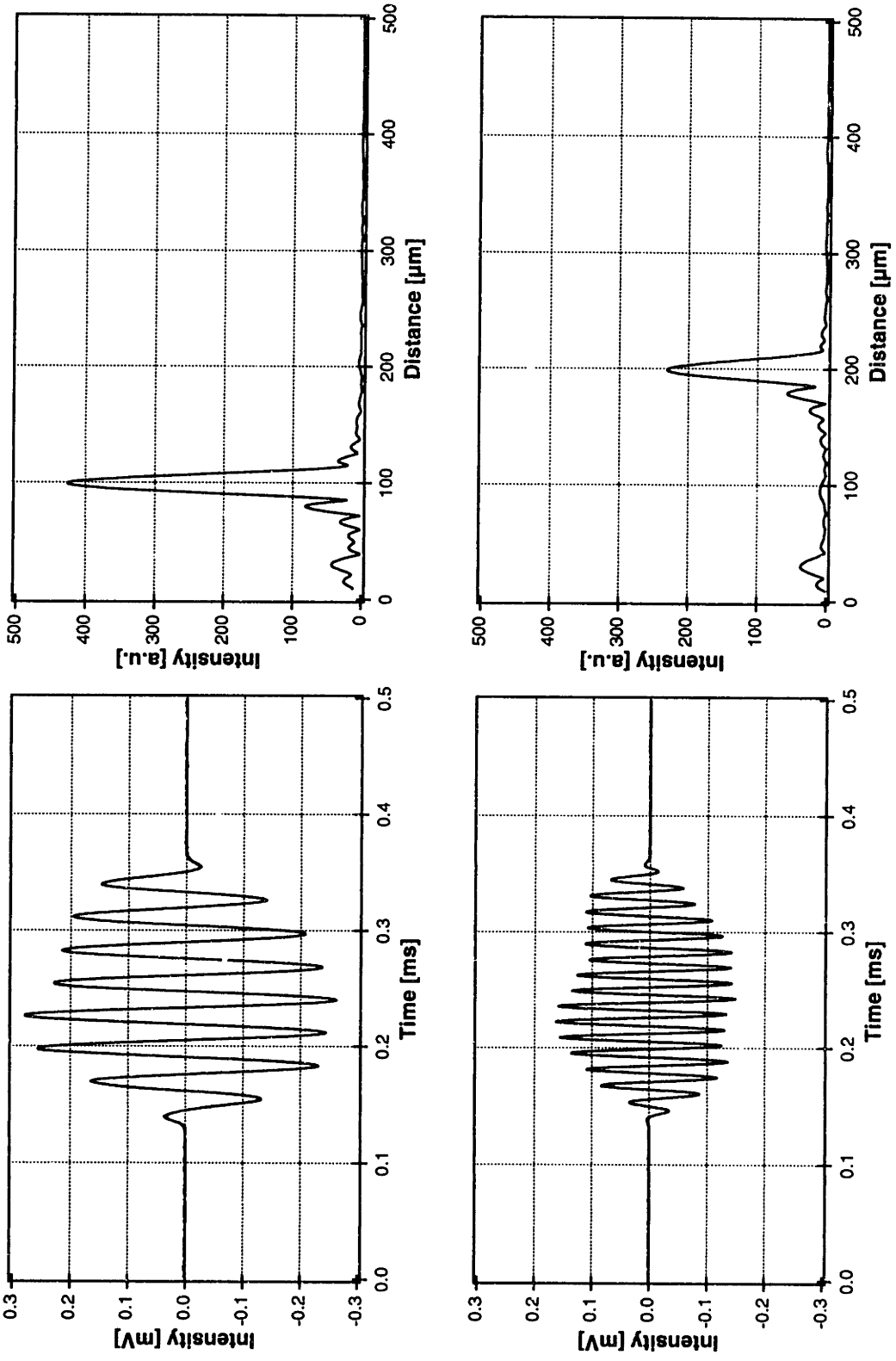

FIGURE 5-10: Interferograms for 100 and 200 μm arm length difference of the Michelson Interferometer and the corresponding Fourier transforms. The tuning frequency was 1 kHz and resolution of the system was measured to be 15 μm.

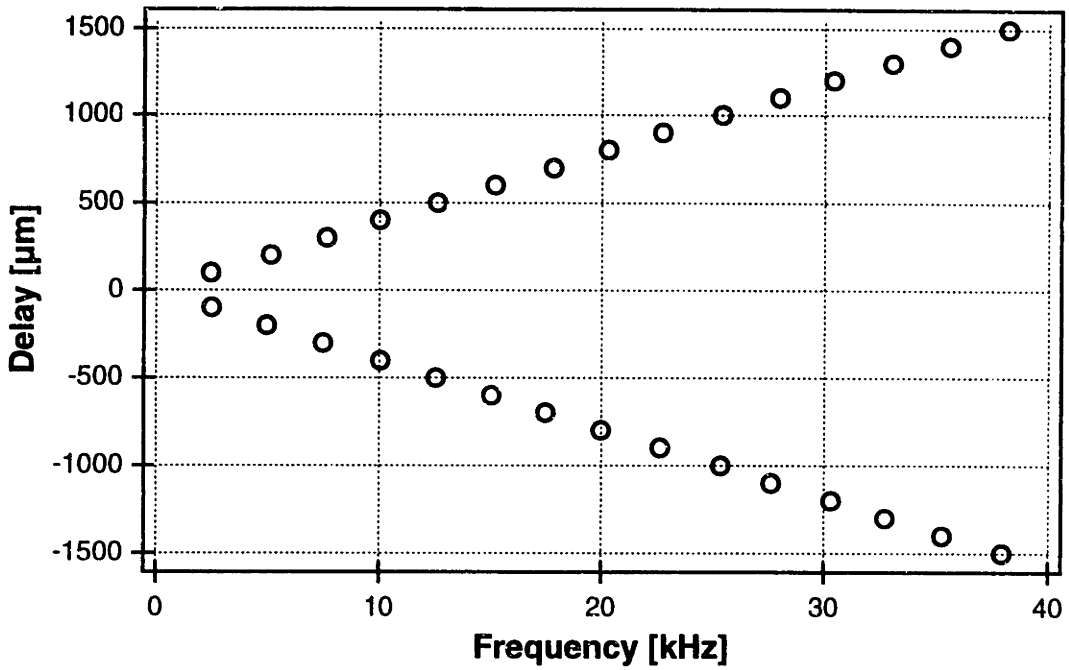

(a)

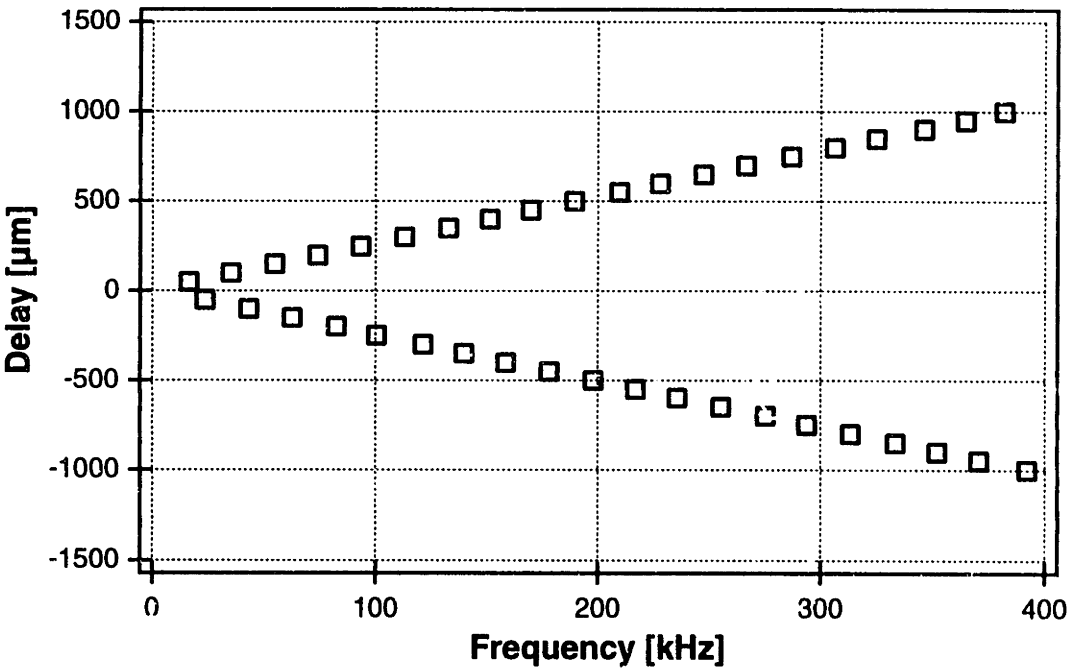

(b)

FIGURE 5-11: Linear dependency between the interferometer arm mismatch as a function of interferogram beat frequency: (a) 100 Hz and (b) 1 kHz wavelength tuning frequency.

in Figure 5-8. There was no appreciable difference in the longitudinal resolution of the system for different scan frequencies and is as predicted by equation (5-17) solely a function of the wavelength tuning bandwidth and shape.

5.3.3 Tuning rate limitations

A comparison of the data in Figures 5-9 and 5-10 indicated that the reflection peak magnitudes were diminished at increased scan frequencies. To quantify this tendency the magnitude of the reflection peaks were recorded as a function of the interferometer arm mismatch. This measurement was repeated for various Cr^{4+}:forsterite laser tuning rates. Representative data obtained for two select wavelengths, 100 Hz and 1kHz, are shown in Figure 5-12. The decrease in reflec-

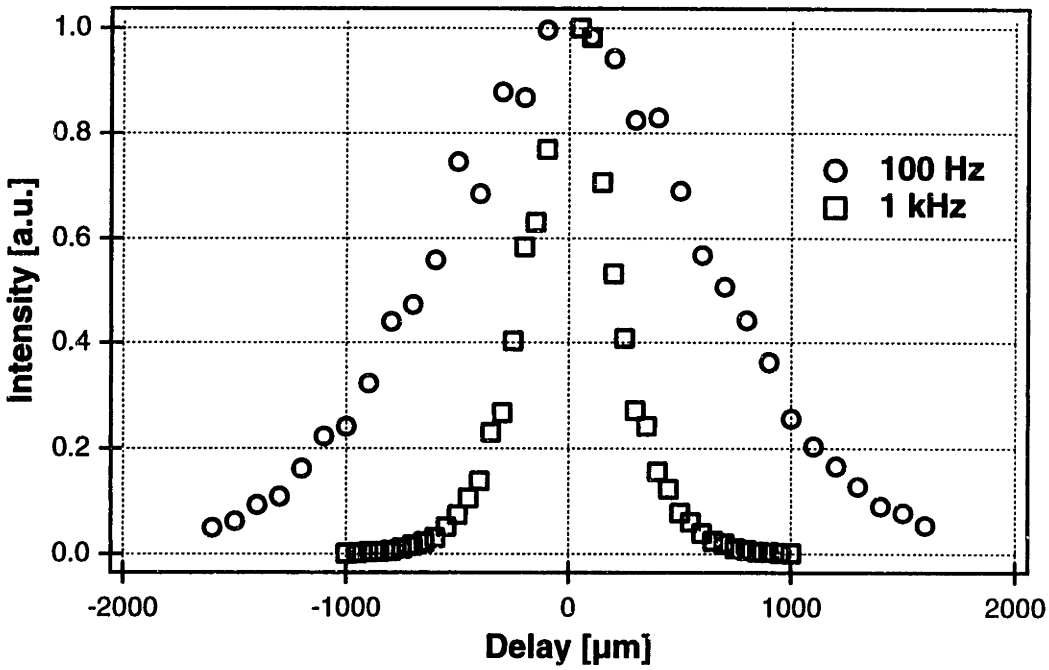

FIGURE 5-12: Reflection peak intensity as a function of interferometer arm mismatch for laser tuning frequencies of 100 Hz and 1 kHz.

tion signal magnitude for increasing interferometer delays is consistent with the theoretical analysis discussed in section 5.2.1 and can be attributed to the limited coherence length (coherence time) of the optical source. However, the change in OFDR system performance with laser tuning rate implies that the coherence properties of the Cr^{4+}:forsterite laser are affected by the tuning rate. Increasing the wavelength scanning rate resulted in an apparent decrease in the coherence

length of the laser emission. To quantify this change in coherence length a best fit of the second term in equation (5-12) was performed to the data in Figure 5-12, as well as additional frequencies in the range form 50 Hz to 1 kHz. The dependence of the laser coherence length on the laser tuning rate is shown in Figure 5-13.

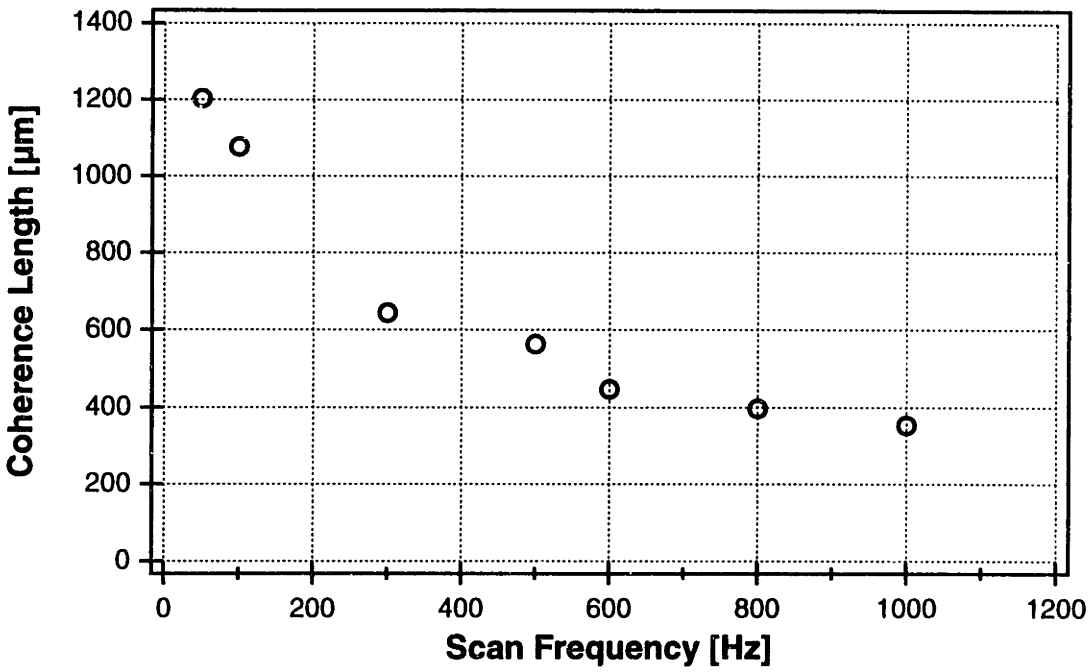

FIGURE 5-13: Dependence of the effective laser coherence length on the laser tuning frequency.

In this cavity configuration the laser operated at all times in a wide span of longitudinal cavity modes. However, the increase in coherence length indicated that the number of cavity modes involved in the gain competition increases with the tuning rate. This increase in laser linewidth can be attributed to a small differential loss between the lasing frequency and the newly selected frequency, such that the new frequencies build up before the old ones fully diminish. Unlike in a single-mode (single longitudinal cavity mode) laser, in this standing-wave cavity configuration many spatial modes compete for the gain and several can actually be lasing at any time. The standing wave geometry results in spatial hole burning which allows for the simultaneous lasing of multiple longitudinal cavity modes in a homogeneously broadened gain medium. Spatial hole burning may actually be beneficial to the rapid frequency switching dynamics by in effect seeding new lasing wavelengths [94]. For OFDR applications in which tunable solid-state lasers are used,

singe-mode operation should in general be avoided. In practice it is very difficult to perform a measurement which would provide information about the instantaneous laser behavior when subject to rapid wavelength tuning. The systematic characterization of the OFDR system performance is in fact a very precise tool for an indirect measurement of laser coherence dynamics.

The fundamental limit for the rate at which a solid-state laser can be tuned is determined by the resonator relaxation dynamics [94]. Relaxation oscillations result from the interdependence between energy stored in the electric field and energy stored in the excited state of the gain crystal and are initiated by rapid changes of the cavity loss or gain [95]. When the resonator loss is rapidly increased the field is diminished. this reduces the rate at which energy is extracted from the excited state and leads to a buildup of excess excited state population. This in turn, increases the gain and leads to a buildup of the field energy. This induced oscillations in resonator output energy can be characterized by the equation:

$$\omega = \sqrt{\frac{r-1}{\tau_c} \cdot \frac{1}{\tau_2}} \tag{5-22}$$

where the quantity r is a measure of how many times the laser is above threshold, τ_c is the cavity decay time, and τ_2 is the excited state lifetime. From this equation one can infer that the detrimental effects of relaxation oscillations on the tuning rate of the laser will, in general, be diminished by 1) increasing the wavelength selectivity of the filtering prism sequence, 2) reducing the resonator length, or 3) increasing the output coupling.

The signal-to-noise ratio (SNR) was empirically measured by operating the OFDR system with a high-reflector in the sample arm. Under these conditions neutral density filters were inserted into the sample arm until no beat signal could be measured. The SNR of this system was measured to be 70 dB.

5.4 Applications of rapidly tuned cw Cr^{4+}:forsterite laser

An attractive feature of OFDR is that ranging can be performed without the need to mechanically scan the path length of the interferometer reference arm as is required in OCDR ranging systems. This allows for the scanning of large samples without the limitation brought about by the

scanning of the reference arm over the dimensions of the sample. Moreover, the different optical source requirements of OFDR relative to OCDR may also be advantageous. High-resolution OCDR systems typically require the use of modelocked solid-state lasers, whereas OFDR systems of comparable resolution are based on tunable cw solid-state lasers which may be significantly less complex. This section illustrates a few high-resolution imaging applications of an OFDR system using a rapidly tuned cw Cr^{4+}:forsterite laser.

5.4.1 OFDR application to surface profiling

Non-contact measurements of surface profiles is an important function in numerous engineering and manufacturing applications. To demonstrate the surface profiling capability of this system a surface reconstruction image of the lettering on the U.S. One Cent coin was performed. The coin was placed in the sample arm of the interferometer such that the zero-path-difference for the two interferometer arms was placed above the surface of the coin. The schematic of the system used is shown in Figure 5-7 and the light was focused onto the sample such that the focal spot size was 20 μm in diameter corresponding to a confocal parameter of 1 mm. For obtaining the 3-D surface profile the coin was moved on translation stages in a 20 μm × 20 μm grid such that at each point an axial scan was acquired. The galvanometric actuator was driven with an 100 Hz triangle - wave drive. For cases where the galvanometer is driven with a triangular voltage waveform the positive and negative angular deflection scans can be used for data acquisition. Thus, when a 100 Hz triangle drive was used, the actual data acquisition rate corresponded to 200 axial scans per second. Figure 5-14 shows the reconstructed lettering on the font side of a U.S. One Cent coin, the letters "BE" in "LIBERTY" were scanned with 15 μm axial resolution. The surface profile shown in Figure 5-14 was obtained by taking a 16-bit FFT of the acquired interferogram at each of the points in the image. The image is displayed such that lighter shades represent higher features than darker shades.

5.4.2 OFDR imaging of partially reflecting samples

In many applications it is necessary to perform ranging measurements through turbid media. If the medium under investigation has layers of different index of refraction, each interface will result in some reflection of the incident light. If the back-reflected light is coupled back into the interferometer, the positions of these interfaces can be measured with an OFDR ranging system.

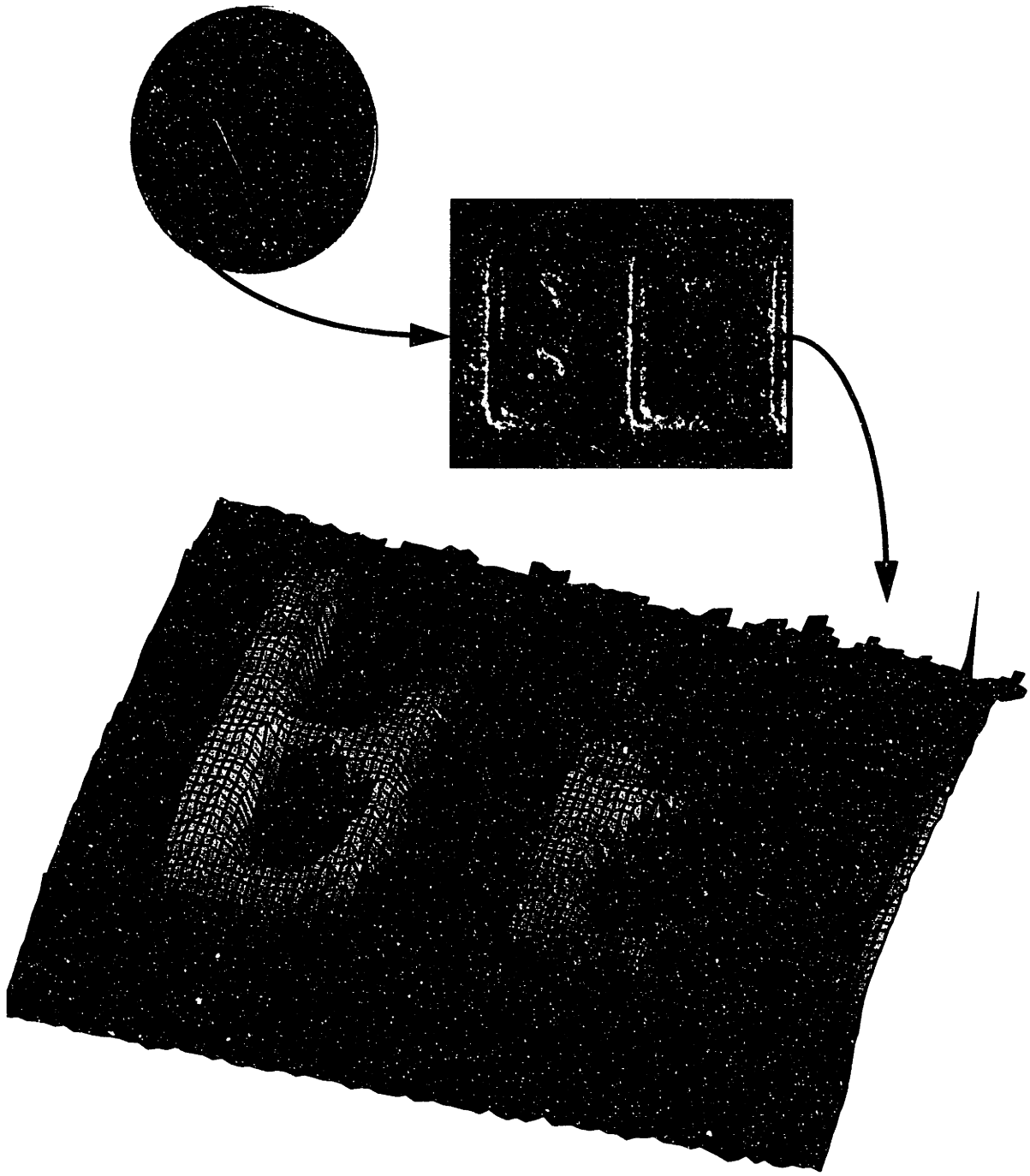

FIGURE 5-14: Reconstructed surface image of a part of an U.S. One Cent coin. The axial (depth) resolution set was 15 μm, and transverse points were acquired in a 20 μm × 20 μm grid by moving the sample.

Strictly speaking, the OFDR ranging system measures the optical path length between different reflectors. Thus, to actually determine the free-space sample size, the index of refraction needs to be known.

To demonstrate the ranging capability of the OFDR system based on a rapidly tuned cw Cr^{4+}:forsterite laser a test sample was constructed. This test sample consisted of two glass microscope slide cover slips separated by an air gap. The schematic of the system used is shown in Figure 5-4 and the light was focused onto the sample such that the focal spot size was 20 μm in diameter corresponding to a confocal parameter of 1 mm. The sample was positioned at a distance away from the zero-path-difference point of the two interferometer arms to prevent any ambiguity in the measured results. If any part of the sample were to cross the zero-path-difference point it would not be possible to distinguish reflections from either side of this point. The top image in Figure 5-15 shows the reflectivity map of the test sample as a function of the axial as well as transverse position. To obtain this 2-D image the sample was translated in 100 μm increments in the transverse direction, and axial scans were recorded at each position. The bottom image in Figure 5-15 shows the intensity profile of one axial scan. Reflections from each interface can clearly be distinguished and the separation between each reflection is a measure of the optical path difference. The scanning high-reflector was driven with a 100 Hz triangle wave (200 axial scans per second) and 16-bit FFT's were performed on each of the interferograms to obtain the reflectivity profiles.

The results of this measurement can be used to determine the index of refraction of the glass microscope slide cover slips. A stack consisting of ten cover slips was measured using a standard caliper to be (1.448±0.015) mm and the thickness of one cover slip was extracted as (145±2) μm. From the OFDR reflectivity trace shown in Figure 5-15 one can obtain the optical path length in the glass as (218±4) μm. The index of refraction of the glass cover slip can then be calculated as the ratio of these two thicknesses such that n(1.235 μm)=1.50±0.03. Conversely, if the index of refraction of the material is known the actual sample size can be extracted by measuring the optical path length.

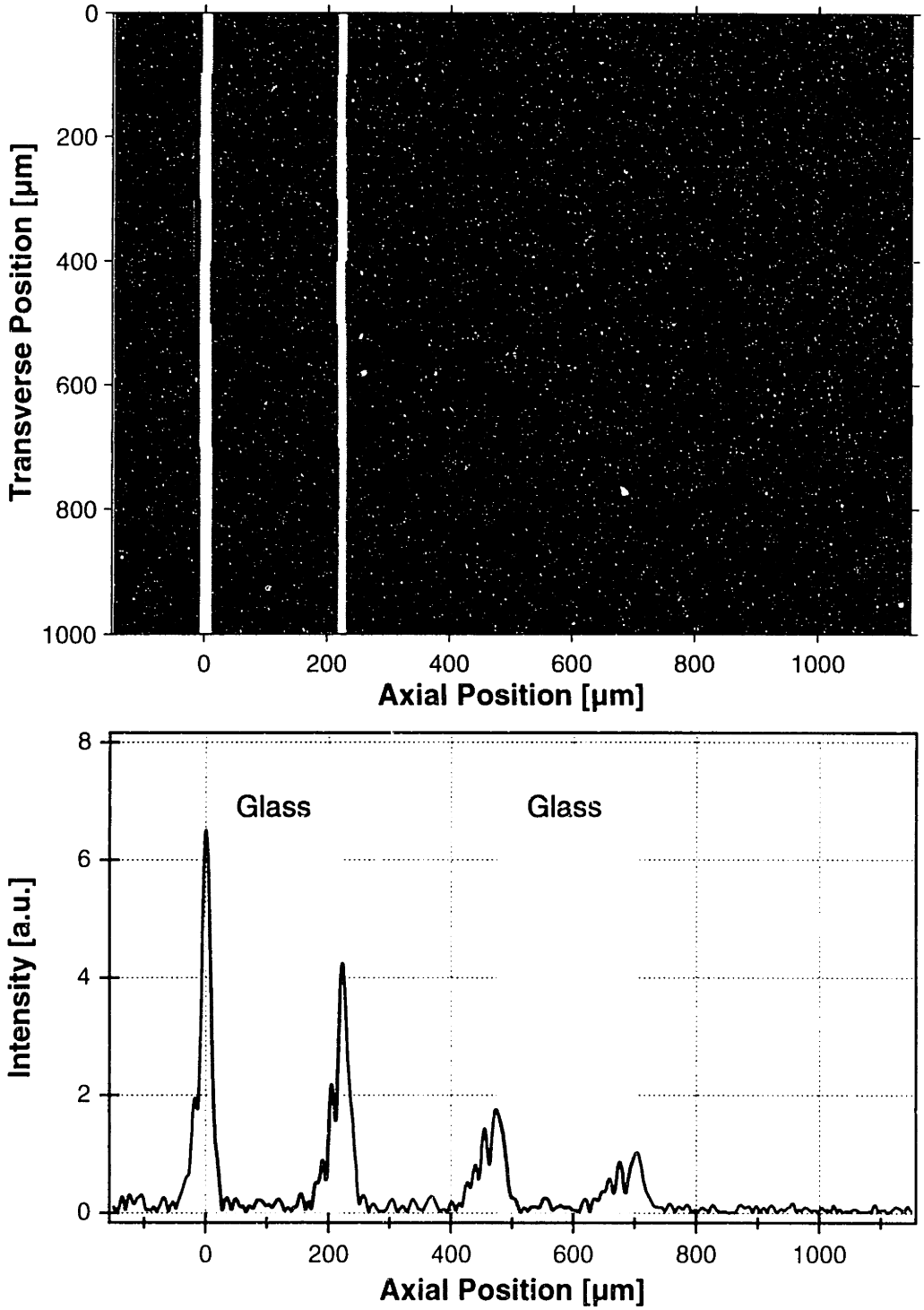

FIGURE 5-15: Top: 2-D intensity plot of the back reflected signal from two microscope slide cover slips, each 150 µm thick, with an air gap in-between. Transverse scans were obtained in 100 µm increments. Bottom: one axial scan of the above image. The axial position is a measure of the optical path.

Another set of measurements was performed by measuring the surface profile of a sample submerged in a scattering solution. Since one of the possible applications of OFDR imaging systems is to the imaging of biological samples it is of interest to evaluate the performance of this system for imaging through a multiply scattering medium. The test sample was once again a U.S. One Cent coin, and the structure which was imaged were the columns of the Lincoln Memorial engraved on the backside of the coin. The coin was submerged in a solution of Nanosphere™ size standard polystyrene spheres (502±4) nm in diameter fabricated by *Duke Scientific Corporation.* Polystyrene sphere solutions are commonly used to simulate various biological specimens. In this specific experiment the solution had a calculated loss coefficient of α=50 cm^{-1} and the mean free path between scattering events was 200 μm. The light was delivered such that the focal spot size was 20 μm in diameter corresponding to a confocal parameter of 1 mm. The scanning high-reflector was driven with a 100 Hz triangle wave and 16-bit FFT's were performed on each of the interferograms. The sample was placed on a translation stage and moved in 10 μm steps to allow for imaging in the transverse direction.

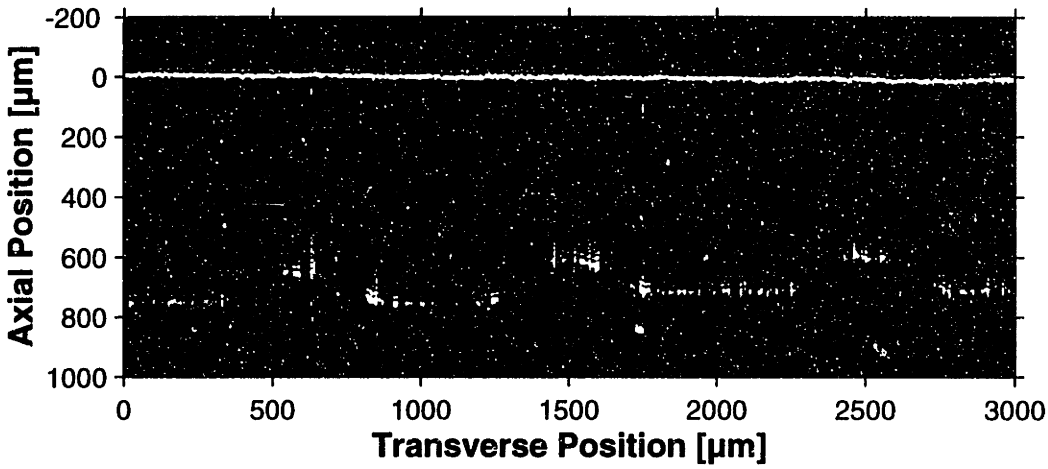

FIGURE 5-16: An OFDR image of the Lincoln Memorial columns on the backside of an U.S. One Cent coin. The coin was submerged in a multiply scattering solution.

Figure 5-16 shows a 2-D intensity map of the reflections from the coin surface. The strong reflection on top of the image (at 0 μm axial position) is due to the air-solution interface at which point the axial scale is set to zero for reference purposes. The actual zero-path-difference for the two interferometer arms was at about –350 μm. The three elevated features in the image represent

the "columns" of interest. At the sides of each of the "columns" the back-reflected signal appears to drop out. This loss of signal can be attributed to the curvature of the metallic surfaces and in these areas the light is reflected at angles such that it can not be collected for detection. This highlights a concern when optical imaging techniques are used in imaging of highly reflective surfaces for which the scanning beam can be reflected at angles away from the incident direction. Thus if OFDR (OCDR or spectral radar) is used for surface profiling it may be necessary to collect data at various angles of incidence to assure complete surface profiling. In some cases however, assumptions about the surfaces may be made and interpolation techniques could be applied. This concern does not apply in cases where the back-reflected signal is due to scattering events as opposed to specular reflections.

5.4.3 Data acquisition issues

In the system shown in Figure 5-7 the interferogram data were acquired by downloading the digitized oscilloscope traces to a personal computer. In actual system implementations the oscilloscope would be replaced by analog-to-digital converting circuitry for capturing the time-dependent interferogram traces. In this prototype OFDR system, each oscilloscope trace was digitized into 10000 data points. The interferogram data set for the image displayed in Figure 5-16 was in excess of 24 Mbytes in size. All waveforms were zero-padded to perform 16-bit FFT's and calculation of the reflectivity profiles. After data processing, typical data sets could be reduced to 6 Mbytes. This illustrates an important aspect to OFDR measurements where the data acquisition and display process depends heavily on fast computing.

In comparison to OCDR systems, OFDR systems shift the complexity from the optical source to the data processing equipment. In high-resolution OCDR systems modelocked solid-state lasers are used which are intrinsically more complex than tunable cw lasers in OFDR systems. Moreover, OFDR systems do not require scanning-arm interferometers but are based on simpler fixed-arm-length Michelson interferometers. However, to perform real-time OFDR measurements for which images could be displayed at video rates (24 images per second) it would be necessary to perform real-time FFT's for every image before it can be displayed. Thus, for a typi-

cal image as shown in Figure 5-16 one would need to perform 300 16-bit FFT's before the image can be displayed in full. Recent advancements in personal computers and specialized digital-signal-processing equipment are such that these computing requirements are within reach of present technology.

Chapter 6

Contributions and future work

6.1 Contributions

The work presented in this thesis contains a new, comprehensive study of the performance of cw Cr^{4+}:forsterite lasers based on crystals grown and operated along different crystallographic axes. It was concluded that lasers using a 1064 nm excitation source and for which the pump polarization is aligned parallel to the *b*-axis and propagating along either the *a*- or *c*-axis result in comparable performances. Thus, if one of these orientations can yield better results in crystal growth there appears to be no fundamental reason against its implementation in lasers. Extensive studies of cw efficiency and tuning ranges of lasers based on *a*- and *c*-axis crystals support this finding.

This thesis also presents the first studies of a novel room-temperature operated Cr^{4+}:forsterite laser pumped in the near-IR. The cw performance of this laser was studied as a function of various output couplers as well as for a range of pump wavelengths in the near-IR. This study resulted in the demonstration of the largest to-date reported tuning range, 200 nm, from a cw Cr^{4+}:forsterite laser. In addition, Kerr-lens modelocked operation of a Cr^{4+}:forsterite with a near-IR pump laser resulted in the generation of 50 fs optical pulses. This study was partially motivated by the large absorption coefficient at wavelengths near 740 nm where semiconductor diode lasers are available. Issues concerning direct diode-pumping were studied in systems which use simultaneous pumping with a diffraction limited Ti:Al_2O_3 laser and 670 nm broad-area laser diodes.

The OFDR system based on a Cr^{4+}:forsterite laser is the first to take advantage of the broad bandwidth provided by solid-state lasers to achieve high-resolution axial imaging capabilities. This system provides comparable spatial resolution as a high-resolution OCDR systems using solid-state lasers without the complexities involved in operating a modelocked laser. This work demonstrated and discussed issues associated with the system implementation using a Cr^{4+}:forsterite lasers. However, the findings are likely to be applicable to other solid-state lasers as well.

6.2 Future Work

Shortly before the completion of this manuscript a group of researchers at Cornell University reported successful direct diode-pumping of a cw Cr^{4+}:forsterite laser [96]. This publication is the first study directly motivated by the near-IR pumped Cr^{4+}:forsterite work presented in this manuscript. The results obtained by the Cornell University group are in close agreement with the preliminary work presented in this thesis. Even though the demonstrated output powers were rather low, this development is of great interest since it supports the findings about near-IR pumping of Cr^{4+}:forsterite lasers discussed in this thesis. Future work should be focused on further increasing the crystal doping and the fabrication of commercially available laser diodes at 700^{+}nm. Advances in both areas will facilitate the implementation of compact, tunable cw, as well as modelocked Cr^{4+}:forsterite lasers.

The use of a rapidly tunable Cr^{4+}:forsterite laser is of particular interest for OFDR because it is a solid-state laser with a broad emission bandwidth in the 1.3 μm wavelength range well suitable for medical applications. However, not all imaging applications require the use of this particular wavelength range. Future work using this OFDR technique should be considered in conjunction with other solid state systems with phonon broadened emission bands including, Cr^{4+}:YAG, Ti:Al_2O_3, Cr^{3+}:LiSrAlF, and Cr^{3+}:LiSrGaF. Efforts should also be directed to further studies of the laser tuning dynamics with the goal of extending the axial ranging capabilities of high-resolution OFDR systems. Two laser media, Cr^{3+}:LiSrAlF and Cr^{3+}:LiSrGaF, should be closely scrutinized for use in OFDR systems. Their performance is of interest since their material properties are somewhat different than for the other three gain media outlined in Table 1-1. The excited state lifetimes of Cr^{3+}:LiSrAlF and Cr^{3+}:LiSrGaF are significantly longer than for the

other materials and their stimulated emission cross-sections are smaller. Also, these gain media can be pumped by readily available 670 nm broad-area laser diodes and would allow for the implementation of compact and mobile optical ranging systems.

For OFDR systems based on the Cr^{4+}:forsterite laser, one of the weaknesses is the limited ranging capability due to a decrease in laser coherence length with increasing laser tuning rates. Future work should include the use of additional wavelength filtering prisms, or prisms with higher angular dispersion. In addition, shorter cavity configurations should be implemented to reduce cavity buildup time. The cavity length can be reduced by a factor of two if end-pumped laser cavities are used such that the total resonator length can realistically be reduced to ~30 cm. This, in conjunction with other optimizations may improve the ranging distance to several millimeters. If ranging distances are extended to about 5 mm, at scan rates of 2000 scans per second, such OFDR system could be applied to high-resolution, real-time, non-destructive imaging in engineering or medicine.

References

[1] T. H. Maiman, "Optical Maser action in ruby," *British Communication of Electronics*, vol. 7, pp. 674, 1960.

[2] P. F. Moulton, "Spectroscopy and laser characteristics of Ti:Al_2O_3," *J. Opt. Soc. Am. B*, vol. 9, pp. 560, 1986.

[3] L. Spinelly, B. Couillaud, N. Goldblat, and D. K. Negus, "Starting an Generation of Sub-100fs Pulses in Ti:Al_2O_3 by Self-Focusing," presented at Conference on Lasers and Elecro-optics, Baltimore, MD, 1991.

[4] I. D. Jung, F. X. Kärtner, N. Matuschek, D. H. Sutter, F. Morier-Genoud, G. Zhang, U. Keller, V. Scheuer, M. Tilsch, and T.Tschudi, "Self-starting 6.5-fs pulses from a Ti:sapphire laser," *Opt. Lett.*, vol. 22, pp. 1009-1011, 1997.

[5] S. A. Payne, L. L. Chase, H. W. Newkirk, L. K. Smith, and W. F. Krupke, "$LiCaAlF_6:Cr^{3+}$: a promising new solid-state laser material," *IEEE J. Qunatum Electron.*, vol. 24, pp. 2243-2252, 1988.

[6] S. A. Payne, L. L. Chase, L. K. Smith, W. L. Kway, and H. W. Newkirk, "Laser performance of $LiSrAlF_6:Cr^{3+}$," *J. Appl. Phys.*, vol. 66, pp. 1051-1056, 1989.

[7] L. K. Smith, S. A. Payne, W. L. Kway, L. L. Chase, and B. H. T. Chai, "Investigation of the Laser Properties of Cr^{3+}:$LiSrGaF_6$," *IEEE J. Quant. Elect.*, vol. 28, pp. 2612-2618, 1992.

[8] R. Scheps, "Cr:$LiCaAlF_6$ laser pumped by visible laser diodes," *IEEE J. Quantum Electron.*, vol. 27, pp. 1968-1970, 1991.

[9] R. Scheps, J. F. Meyers, H. B. Serreze, A. Rosenberg, R. C. Morris, and M. Long, "Diode-pumped Cr:$LiSrAlF_6$ laser," *Opt. Lett*, vol. 16, pp. 820-822, 1991.

[10] V. P. Yanovsky, A. Korytin, F. W. Wise, A. Cassanho, and H. P. Jenssen, "Femtosecond Diode-Pumped Cr:LiSGAF Laser," *IEEE J. Selected Topics in Quantum Electron.*, vol. 2, pp. 465-472, 1996.

[11] N. A. Noginov, H. P. Jenssen, and A. Cassanho, "Characterization of tunable Cr:LiSGAF laser material," presented at CLEO, Washington, DC, 1993.

[12] M. J. P. Dymott and A. I. Ferguson, "Pulse duration limitations in a diode-pumped femtosecond Kerr-lens mode-locked Cr:LiSAF laser," *Applied Physics B*, vol. 65, pp. 227-234, 1997.

[13] I. T. Sorokina, E. Sorokin, E. Winter, A. Cassanho, H. P. Jenssen, and R. Szipocs, "Sub-20 fs pulse generation from the mirror dispersion contrelled Cr:LiSaF and Cr:LiSAF laser," *Appl. Phys. B*, vol. 65, pp. 245-253, 1997.

[14] I. T. Sorokina, E. Sorokin, E. Winter, A. Cassanho, H. P. Jenssen, and R. Szipocs, "14-fs pulse generation in KLM prismless Cr:LiSGaF and Cr:LiSAF lasers: observation of pulse frequnecy shift," *Opt. Lett.*, pp. 1716-1718, 1997.

[15] D. Kopf, K. J. Weingarten, L. R. Brovelli, M. Kamp, and U. Keller, "Diode-pumped 100-fs passively mode-locked Cr:LiSAF laser with an antiresonant Fabry-Perot saturable absorber," *Opt. Lett.*, vol. 19, pp. 2143-2145, 1994.

[16] D. Kopf, A. Prasad, G. Zheng, M. Moser, and U. Keller, "Broadly tunable femtosecond Cr:LiSAF laser," *Opt. Lett.*, vol. 22, pp. 621-623, 1997.

[17] D. Kopf, U. Keller, M. A. Emanuel, R. J. Beach, and J. A. Skidmore, "1.1-W cw Cr:LiSAF laser pumped by a 1-cm diode array," *Opt. Lett.*, vol. 22, pp. 99-101, 1997.

[18] D. Kopf, K. J. Weingarten, G. Zhang, M. Moser, M. A. Emanuel, R. J. Beach, J. A. Skidmore, and U. Keller, "High-average-power diode-pumped femtosecond Cr:LiSAF lasers," *Applied Physics B*, pp. 235-243, 1997.

[19] N. B. Angert, N. I. Borodin, V. M. Garmash, V. A. Zhitnyuk, A. G. Okhrimchuk, O. G. Siyuchenko, and A. V. Shestakov, "Lasing due to impurity color centers in yttrium aluminum garnet crystals at wavelengths in the range 135-1.45 μm," *Sov. J. Quantum Electron.*, vol. 18, pp. 73-74, 1988.

[20] A. V. Shestakov, N. I. Borodin, V. A. Zhitnyuk, A. G. Okrimtchyuk, and V. P. Gapontsev, "Tunable Cr^{4+}:YAG lasers," presented at Conference on Lasers and Elctro-Optics, Washington, DC, 1991.

[21] A. Sennargolu, C. R. Pollock, and H. Nathel, "Efficient continious-wave chromium-doped YAG laser," *J. Opt. Soc. Am. B*, vol. 12, pp. 930-937, 1995.

[22] P. M. W. French, N. H. Rizvi, J. R. Taylor, and A. V. Shestakov, "Continuous-wave mode-locked Cr^{+4}YAG laser," *Opt. Lett.*, vol. 18, pp. 39-41, 1993.

[23] A. Sennaroglu, C. R. Pollock, and H. Nathel, "Continuous-wave self-mode-locked operation of a femtosecond Cr4+:YAG laser," *Opt. Lett.*, vol. 19, pp. 390-392, 1994.

[24] Y. P. Tong, P. M. W. French, J. R. Taylor, and J. O. Fujimoto, "All-solid-state femtosecond sources in the near infrared," *Opt. Comm.*, vol. 136, pp. 235-238, 1996.

[25] B. Hu, H. Zhu, P. Deng, and P. Pan, "Growth and perfection of chromium-doped forsterite," *Journal of Crystal Growth*, vol. 128, pp. 991-995, 1993.

[26] V. Petricevic, S. K. Gayen, and R. R. Alfano, "Laser action in chromium activated forsterite for near-infrared excitation: Is Cr^{4+} the lasing ion?," *Appl. Phys. Lett*, vol. 53, pp. 2590-2592, 1988.

[27] H. R. Verdún, L. M. Thomas, D. M. Andrauskas, and A. Pinto, "Laser performance of chromium-aluminum-doped forsterite," presented at Tunable Solid State Lasers, Washington, DC, 1989.

[28] R. Moncorgé, D. J. Simkin, G. Cormier, and J. A. Capobianco, "Spectroscopic properties and fluorescence dynamics in chromium-doped forsterite," presented at Tunable Solid State Lasers, Washington, DC, 1989.

[29] B. E. Scheetz and W. B. White, "Synthesiss and optical absorption spectra of C^{2+}-containing orthosilicates," *Contr. Mineral. Petrol.*, vol. 37, pp. 221-227, 1972.

[30] R. Rager and G. Weiser, "Polarized absorption spectra of trivalent chromium in forsterite, Mg_2SiO_4," *Bull. Mineral.*, vol. 104, pp. 603-609, 1981.

[31] Y. Yamaguchi, K. Yamagishi, A. Sugimoto, and Y. Nobe, "Optical properties and crysstal growth atmosphere of forsterite," presented at Advanced Solid-State Lasers, Washington, DC, 1991.

[32] W. Jia, L. Lu, B. M. Tissue, and W. M. Yen, "Valence and site occupation of chromium ions in single-crystal forsterite fibers," *J. Crystal Growth*, vol. 109, pp. 329-333, 1986.

[33] J. A. Caird, M. D. Shinn, T. A. Kirchoff, L. K. Smith, and R. E. Wilder, "Measurements of losses and lasing efficiency in GSGG: Cr, Nd and YAG:Nh laser rods," *Appl. Opt.*, vol. 25, pp. 4294-4305, 1986.

[34] W. Jia, B. M. Tissue, L. Lu, K. R. Hoffman, and W. M. Yen, "Near-infrared luminescence in Cr, Ca-doped yttrium aluminum garnet," presented at Advanced Solid-State Lasers, Washington, DC, 1991.

[35] S. Kück, K. Petermann, and G. Huber, "Spectroscopic investigation of the Cr^{4+}-center in YAG," presented at Advanced Solid-State Lasers, Washington, DC, 1991.

[36] M. H. Garrett, V. H. Chan, H. P. Jenssen, M. H. Whitmore, A. Scara, D. J. Singel, and D. J. Simkin, "Comparison of chromium forsterite and akermanite laser host crystals," presented at Advanced Solid-State Lasers, Washington, DC, 1991.

[37] T. H. Allik, B. H. T. Chai, and L. D. Merkle, "Crystal growth and spectroscopic analysis of Cr4+-doped melilite compounds," presented at Advanced Solid-State Lasers, Washington, DC, 1991.

[38] R. Moncorgé, G. Cormier, D. J. Simkin, and J. A. Capobianco, "Fluorescence Analysis of Chromium-Doped Forsterite (Mg_2SiO_4)," *IEEE J. Quantum Electron.*, vol. 27, pp. 114120, 1991.

[39] V. G. Baryshevski, M. V. Korzhik, M. G. Livshitz, A. A. Tarasov, A. E. Kimaev, I. I. Mishkel, M. L. Meilman, B. I. Minkov, and A. P. Shkadarevich, "Properties of forsterite and the performance of dorsterite lasers with lasers and flashlamp pumping," presented at Advanced Solid-State Lasers, Washington, D.C., 1991.

[40] T. J. Carrig and C. R. Pollock, "Performance of a continuous-wave forsterite laser with krypton ion, Ti:sapphire, and Nd:YAG pump lasers," *IEEE J. Quant. Electr.*, vol. QE-29, pp. 2835-2844, 1993.

[41] J. M. Evans, V. Petricevic, A. B. Bykov, A. Delgado, and R. R. Alfano, "Direct diode-pumped continuous-wave near-infrared tunable operation of Cr^{4+}:forsterite and Cr^{4+}:Ca_2GeO_4," *Opt. Lett.*, vol. 22, pp. 1171-1173, 1997.

[42] V. Petricevic, S. K. Gayen, R. R. Alfano, K. Yamagishi, H. Anzai, and Y. Yamaguchi, "Laser action in chromium-doped forsterite," *Appl. Phys. Lett*, vol. 52, pp. 1040-1042, 1988.

[43] V. Petricevic, A. Seas, and R. R. Alfano, "Slope efficiency measurement of a chromium-doped forsterite laser," *Opt. Lett.*, vol. 16, pp. 811-813, 1991.

[44] T. J. Carrig and C. R. Pollock, "Tunable, cw operation of a multiwatt forsterite laser," *Opt. Lett.*, vol. 16, pp. 1662-1664, 1991.

[45] B. Minkov, "personal communication on Cr^{4+}:forsterite crystal growth," . Institute for Single Crystals, Kharkov, Ukraine, 1995.

[46] H. G. Danielmeyer, "Lasers," , vol. 4, A. K. Levine and A. DeMaria, Eds. New York: Marcel Kekker, 1975, pp. 1-71.

[47] G. Onishchukov, W. Hodel, H. P. Weber, V. Mikhailov, and B. Minkov, "CW lasing characteristics of high Cr^{4+}-concentration forsterite," *Opt. Comm.*, vol. 100, pp. 137-140, 1993.

[48] R. L. Fork, B. I. Greene, and C. V. Shank, "Generation of optical pulases shorter than .1 psec by colliding pulse modelocking," *Appl. Phys. Lett.*, vol. 38, pp. 671-673, 1981.

[49] J. Mark, L. Y. Liu, K. L. Hall, H. A. Haus, and E. P. Ippen, "Femtosecond pulse generation in a laser with a nonlinear external resonator," *Opt. Lett.*, vol. 14, pp. 48-50, 1989.

[50] E. P. Ippen, H. A. Haus, and L. Y. Liu, "Additive pulse mode locking," *J. Opt. Soc. Am. B*, vol. 6, pp. 1736, 1989.

[51] U. Keller, G. W. tHooft, W. H. Knox, and J. E. Cunningham, "Femtosecond pulses from a continuously self-starting mode-locked Ti:sapphire laser," *Opt. Lett.*, vol. 16, pp. 1022-1024, 1991.

[52] M. T. Asaki, C. P. Huang, D. Garvey, J. Zhou, H. C. Kapteyn, and M. M. Murnane, "Generation of 11-fs pulses from a self-mode-locked Ti: sapphire laser," *Opt. Lett.*, vol. 18, pp. 977-979, 1993.

[53] A. Seas, V. Petricevic, and R. R. Alfano, "Continuous-wave mode-locked operation of a chromium-doped forsterite laser," *Opt. Lett.*, vol. 16, pp. 1668-1670, 1991.

[54] A. Seas, V. Petricevic, and R. R. Alfano, "Generation of sub-100-fs pulses from a cw mode-locked chromium-doped forsterite laser," *Opt. Lett.*, vol. 17, pp. 937-939, 1992.

[55] A. Sennaroglu, T. J. Carrig, and C. R. Pollock, "Femtosecond pulse generation by using an additive-pulse mode-locked chromium-doped forsterite laser operated at 77 K," *Opt. Lett.*, vol. 17, pp. 1216-1218, 1992.

[56] A. Sennaroglu, C. R. Pollock, and H. Nathel, "Generation of 48-fs pulses and measurement of crystal dispersion by using a regeneratively initiated self-mode-locked chromium-doped forsterite laser," *Opt. Lett.*, vol. 17, pp. 826-828, 1993.

[57] A. Seas, V. Petricevic, and R. R. Alfano, "Self-mode-locked chromium-doped forstertie laser generates 50-fs pulses," *Opt. Lett.*, vol. 18, pp. 891-893, 1993.

[58] Y. Pang, V. Yanovsky, F. Wise, and B. I. Minkov, "Self-mode-locked Cr:forsterite laser," *Opt. Lett.*, vol. 18, pp. 1168-1170, 1993.

[59] V. Yanovsky, Y. Pang, F. Wise, and B. I. Minkov, "Generation of 25 fs pulses from a self-mode-locked Cr:forsterite laser with optimized group-delay dispersion," *Opt. Lett.*, vol. 18, pp. 1541-1543, 1993.

[60] Z. Zhang, K. Torizuka, T. Itatani, K. Kobayashi, T. Sugaya, and T. Nakagawa, "Self-starting mode-locked femtosecond forsterite laser with a semiconductor saturable-absorber mirror," *Opt. Lett.*, vol. 22, pp. 1006-1008, 1997.

[61] P. T. Guerreiro, S. Ten, E. Slobodchikov, Y. M. Kim, J. C. Woo, and N. Peyghambarian, "Self-starting mode-locked Cr:forsterite laser with semiconductor saturable Bragg reflector," *Optics Communications*, vol. 136, pp. 27-30, 1997.

[62] P. T. Guerreiro, S. Tan, N. F. Borrelli, J. Butty, G. E. Jabbour, and N. Peyghambarian, "PbS quantum-dot doped glasses as saturable absorbers for mode locking of a Cr:forsterite laser," *Appl. Phys. Lett*, vol. 71, pp. 1595-1597, 1997.

[63] J. D. Kafka, W. L. Watts, and J.-W. Pieterse, "Picosecond and femtosecond pulse generation in a regeneratively modelocked Ti:sapphire laser," *IEEE. J. Quantum Electron.*, vol. QE-28, pp. 2151-2162, 1992.

[64] B. E. Bouma, G. J. Tearney, S. A. Boppart, M. R. Hee, M. E. Brezinski, and J. G. Fujimoto, "High-resolution optical coherence tomographic imaging using a mocel-locked ti:Al_2O_3 laser source," *Opt. Lett.*, vol. 20, pp. 1486-1488, 1995.

[65] B. E. Bouma, G. J. Tearney, I. B. Bilinsky, B. Golubovic, and J. G. Fujimoto, "Self-phase-modulated Kerr-lens mode-locked Cr:forsterite laser source for optical coherence tomography," *Opt. Lett.*, vol. 21, pp. 1839-1841, 1996.

[66] G. J. Tearney, B. E. Bouma, S. A. Boppart, B. Golubovic, E. A. Swanson, and J. G. Fujimoto, "Rapid acquisition of in *vivo* biological images by use of optical coherence tomography," *Opt. Lett.*, vol. 21, pp. 1408-1410, 1996.

[67] R. C. Youngquist, S. Carr, and D. E. N. Davies, "Optical coherence domain reflectometry: A new optical evaluation technique," *Opt. Lett.*, vol. 12, pp. 158-160, 1987.

[68] K. Takada, I. Yokohama, K. Chida, and J. Noda, "New measurement system for fault location in optical waveguide devices based on interferometric technique," *Appl. Optics*, vol. 26, 1987.

[69] D. Huang, E. A. Swanson, C. P. Lin, J. S. Schuman, W. G. Stinson, W. Chang, M. R. Hee, T. Flotte, K. Gregory, C. A. Puliafito, and J. G. Fujimoto, "Optical Coherence Tomography," *Science*, vol. 254, pp. 1178-1181, 1991.

[70] E. A. Swanson, D. Huang, M. R. Hee, J. G. Fujimoto, C. P. Lin, and C. A. Puliafito, "High-speed optical coherence domain reflectometry," *Opt. Lett.*, vol. 17, pp. 151-153, 1992.

[71] V. P. Yanovsky and F. W. Wise, "Nonlinear propagation of high-power, sub-100-fs pulses near the zero-depersion wavelength of an optical fiber," *Opt. Lett.*, vol. 19, pp. 1547-1549, 1994.

[72] W. Koechner, *Solid-State Laser Engineering*, Fourth Edition ed. Berlin, Germany: Springer-Verlag, 1996.

[73] K. V. Yumashev, N. V. Kuleshov, P. V. Prokoshin, A. M. Malyarevich, and V. P. Mikhailov, "Excited state absorption of Cr^{4+} ion in forsterite," *Appl. Phys. Lett.*, vol. 70, pp. 2523-2525, 1997.

[74] M. I. Demchuk, N. I. Zhavoronkov, V. P. Mikhailov, and B. I. Minkov, "Efficient lasing in chromium-activated forsterite pumped in the near infrared," *Quantum Electron.*, vol. 24, pp. 19-20, 1994.

[75] K. Horai, "Thermal conductivity of rock-forming minerals," *J. Geophys. Res.*, vol. 76, pp. 1278-1308, 1971.

[76] J. B. Holt, "Thermal diffusivity of olivine," *Earth Planet. Sci. Lett.*, vol. 27, pp. 404-408, 1975.

[77] S. S. Ballard and J. S. Browder, "Thermal properties," in *CRC handbook of Laser Science and Technology*, vol. 4, M. J. Weber, Ed. Boca Raton, FL: CRC Press, 1986, pp. 49-54.

[78] T. Y. Fan and A. Sanchez, "Pump Source Requirements for End-Pumped Lasers," *IEEE J. Quant. Electr.*, vol. 26, pp. 311-316, 1990.

[79] N. V. Kuleshov, V. G. Shcherbitsky, V. P. Mikhailov, S. Hartung, T. Danger, S. Kuck, K. Petermann, and G. Huber, "Excited-State Absorption in Cr^{4+}-Doper Mg_2SiO_4 and Y_2SiO_5 Laser Materials," presented at OSA Trends in Optics and Photonics on Advanced Solid State Lasers, San Francisco, 1996.

[80] S. D. Personick, "Photon probe-An optical fiber time domain reflectometer," *Bell Syst. Tech. J.*, vol. 56, pp. 355-366, 1977.

[81] H. H. Gilgen, R. P. Novak, R. P. Salathe, W. Hodel, and P. Beaud, "Submillimeter Optical reflectometry," *J. Lightwave Technol.*, vol. LT-7, pp. 1225-1233, 1989.

[82] W. V. Sorin, D. K. Donald, S. A. Newton, and M. Nazarathy, "Coherent FMCW Reflectometry Using a Temperature Tuned Nd:YAG Ring Laser," *IEEE Photon. Technol. Lett.*, vol. 4, pp. 1069-1072, 1990.

[83] M. Bail, G. Häusler, J. M. Herrmann, M. W. Lindner, and R. Ringler, "Optical coherence tomography with the "Spectral Radar"-Fast optical analysis in volume scatterers by short coherence interferometry," presented at European Biomedical Optics Week, BiOS '96, Vienna, Austria, 1996.

[84] S. R. Chin, E. A. Swanson, and J. G. Fujimoto, "Optical coherence tomography using a frequency-tunable optical source," *Opt. Lett.*, vol. 22, pp. 340-342, 1997.

[85] S. Shalini and W. V. Sorin, "Phase Noise Considerations in Coherent Optical FMCW Reflectometry," *J. Lightwave Technol.*, vol. LT-11, pp. 1694-1700, 1993.

[86] M. Born and E. Wolf, *Principles of Optics*, Sixth Edition ed. Oxford, England: Pergamon Press, 1980.

[87] K. Takada, "High resolution OFDR with incorporated fiber-optic frequency encoder," *IEEE Photon. Technol. Lett.*, vol. 4, pp. 1069-1072, 1992.

[88] K. Takada, "Fiber-Optic Frequency Encoder for High-Resolution OFDR," *IEEE Photon. Technol. Lett.*, vol. 4, pp. 1174-1177, 1992.

[89] R. Passy, N. Gisin, J. P. v. d. Weid, and H. H. Gilgen, "Experimental and Theoretical Investigations of Coherent OFDR with Semiconductor Laser Sources," *J. Lightwave Technol.*, vol. LT-12, pp. 1622-1630, 1994.

[90] J. P. v. d. Weid, R. Passy, and N. Gisin, "Mid-Range Coherent Optical Frequency Domain Reflectometry with a DFB Laser Diode Coupled to an External Cavity," *J. Lightwave Technol.*, vol. LT-13, pp. 954-960, 1995.

[91] U. Glombitza and E. Brinkmeyer, "Coherent Frequency-Domain Reflectometry for Characterization of Single-Mode Integrated-Optical Waveguides," *J. Lightwave Technol.*, vol. LT-11, pp. 1377-1384, 1993.

[92] U. Haberland, W. Rütten, V. Blazek, and H. J. Schmitt, "Investigation of highly scattering media using near-infrared continuous wave tunable semiconductor laser," presented at Optical Tomography, Photon Migration, and Spectroscopy of Tissue ands Model Media: Theory, Human Studies, and Instrumentation, San Jose, CA, 1995.

[93] H. Barfuss and E. Brinkmeyer, "Modified Optical Frequency Domain Reflectometry with High Spatial Resolution for Components of Integrated Optic Systems," *J. Lightwave Technol.*, vol. 7, pp. 3-10, 1989.

[94] P. A. Schulz, "Fast Electro-Optic Wavelength Selection and Frequency Modulation in Solid State Lasers," *The Lincoln Laboratory Journal*, vol. 3, pp. 463-477, 1990.

[95] A. Siegman, *Lasers*. Mill Valley, CA: University Science Books, 1986.

[96] L. Qian, X. Liu, and F. Wise, "Cr:forsterite laser pumped by borad-area laser diodes," *Opt. Lett.*, vol. 22, pp. 1707-1709, 1997.